Translational self-diffusion in small molecules investigated via NMR spectroscopy and molecular dynamics simulations

Thesis

For the award of the degree of

DOCTOR OF PHILOSOPHY

Supervised by:

Dr. Kavita Dorai

Submitted by:

Satnam Singh

Indian Institute of Science Education & Research Mohali

Mohali 140 306

India

September 2018

Declaration

The work presented in this thesis has been carried out by me under the guidance of Dr. Kavita Dorai at the Indian Institute of Science Education and Research Mohali.

This work has not been submitted in part or in full for a degree, diploma or a fellowship to any other University or Institute. Whenever contributions of others are involved, every effort has been made to indicate this clearly, with due acknowledgement of collaborative research and discussions. This thesis is a bonafide record of original work done by me and all sources listed within have been detailed in the bibliography.

Satnam Singh

Place :
Date :

In our capacity as supervisor of the candidate's PhD thesis work, we certify that the above statements by the candidate are true to the best of our knowledge.

Dr. Kavita Dorai
Associate Professor
Department of Physical Sciences
IISER Mohali

Place :
Date :

Acknowledgements

First of all, I thank my supervisor Dr. Kavita Dorai who turned out to be much more than a PhD supervisor and guided me through all my ventures. Their consistent encouragement has always been a motivation. Without their unwavering guidance, this thesis would not have been possible. At the same time, I would like to thank Prof. Debi Prasad Sarkar, Director, and Prof. N Sathyamurthy former director IISER Mohali. His plausible arguments and easy approach sorted many problems. I also thankful to Prof Arvind.

I would like to thank my doctoral committee member Prof. Sudeshna Sinha and Dipanjan Chakraborty for his useful comments and support throughout the PhD. I am obliged to the faculty of the Department of Physical Sciences of IISER Mohali whose direction and guidance has been very fruitful during the PhD course work and the lab rotations. My sincere thanks to all the faculty members of IISER Mohali for various direct and indirect interactions all through the PhD.

I am happy to be a part of a dynamic research group with numerous research directions. Many thanks to the group meetings and the healthy discussions with the group members. My sincere thanks to the group mates: Amandeep Singh, Rakesh Sharma, Jyotsana Ojha, Jaskaran Singh Nirankari, Dileep Singh, Akanksha Gautam Chandan Sharma, Akash Sherawat and Akshay Gayakwad. I am obliged to my lab mates and friends Harpreet Singh, Shruti Dogra and Debmalya Das for their critical comments, useful discussions and the team spirit. I would like to thank the graduate students Agrim Gupta, Aditya Mishra, Guru Gaurav, Ankit Singh who, during their short stay in the lab turned out to be very helping.

I thank Dr. Paramdip S. Chandi for his help at the numerous occasions, Dr. B. S. Joshi (Application Scientist, Bruker India) for his technical support and guidance. I would also like to thank my senior and collaborator Dr. Raju Nanda, for the useful discussions and pleasant time we had.

I would like to thank the whole of the IISER Mohali staff, who put numerous efforts for making an institute run. I am thankful to my fellow students for their various direct and indirect interactions. Special thanks to Mr. Balbir Singh for various direct and indirect help in the NMR Lab.

Many thanks to my teachers at the school, college and the university levels for their

efforts to shape my future.

My sincere gratitude towards my parents and family who, through all their thick and thin, put my needs at priority and always encouraged to proceed further. Their relentless efforts, sacrifices, patience and consistent faith always inspired me.

I am obliged to NMR research facility of IISER Mohali housing 400 MHz and 600 MHz Bruker NMR spectrometers. During this thesis, various experiments on 600 MHz are performed using QXI, TXI and BBI probeheads, and on 400 MHz spectrometer using BBFO probehead.

Many thanks to the Library facilities that provide access to various journals and books, IISER Mohali computing facilities for providing the access to various different softwares, basic requirements such as internet facilities and the technical support.

I would like to thank CSIR for the financial support during the PhD (Jan. 2012 - Jul. 2017), and IISER Mohali for funding towards participation in EUROMAR 2016, held in Aarhus, Denmark.

Satnam Singh

Abstract of the Thesis

This thesis deals with the study of the diffusion dynamics of small molecules using NMR spectroscopy and molecular dynamics simulations. The contents of the present thesis have been divided into six chapters whose brief account is sketched below:

Chapter 1

This chapter contains an introduction to the basics of NMR spectroscopy, molecular dynamics and molecular diffusion. The physical basis of the NMR signal, the FID and spin magnetization, T_1 and T_2 relaxation processes are discussed in the beginning. The pulsed field gradient NMR technique to measure translational self-diffusion coefficients is described in detail. The basic flowchart for a molecular dynamics simulation is explained and the force fields and other constraints used in the GROMACS molecular dynamics software package is discussed. The fundamentals of molecular diffusion have been explained on the basis of Fick's laws of diffusion.

Chapter 2

The dynamics of drug molecules inside liposomal drug carriers is important from the point of view of understanding their biological interactions. Molecular dynamics simulations are extensively used to study the self-assembly of lipid bilayers and drug penetration into these membrane mimetics. This chapter describes a study using molecular dynamics simulations on a fluorinated drug diffusing inside a lipid bicelle (simulating a drug carrier environment). The conformational and transport properties of the drug inside a bicelle made from a mixture of DMPC/DHPC molecules are studied. The effect of temperature and bicellar phase on these structural and dynamic properties have been investigated. The computations show that the drug molecule is able to penetrate

into the lipid bilayer and drug molecule diffuses anomalously inside the bicelle.

Chapter 3

This chapter describes an NMR spectroscopic study of the temperature dependent dynamic behavior of $LiClO_4$ mixtures of various polyethylene glycols (PEG)-based polymers in three different molecular solvents viz. water, dimethyl sulfoxide (DMSO), and acetonitrile (ACN). Temperature dependent NMR self-diffusion coefficients, spin-lattice (T_1), and spin-spin relaxation (T_2) studies has been performed in order to understand the dynamics of these mixtures. Protons from the ethylene oxide (EO) unit (-OCH_2CH_2-) of polymers have been probed through NMR spectroscopy for its study of chemical shift, diffusion and relaxation studies. It has been observed that the increased temperature of the medium shows a deshielded chemical environment for the protons of EO unit in its D_2O and DMSO mixtures, however a shielded chemical environment has been observed in its ACN mixtures. On the other hand, the hydroxyl proton shows opposite behavior in its mixtures with ACN and DMSO, which is explained on the basis of the H-bonding phenomenon. Increasing temperature of the medium decreases the hydrodynamic radius of polymers and has been explained on the basis of solvation/desolvation phenomenon. A substantial interaction between the lithium cation with the EO unit of the polymer has been observed as probed through ^{1}H-^{7}Li 2D HOESY spectroscopy. The Li-H distance has been calculated by applying the isolated spin pair approximation and the shortest Li-H distance has been observed in its DMSO mixtures as compared to its ACN mixtures suggesting a stronger interaction between the Li+ cation with the polymer cage in its DMSO mixtures.

Chapter 4

Studies of the dynamics and conformation of polymer chains in ionic liquids are of great interest as they have wide-ranging applications in fuel cells, batteries and gas separation. Different binary mixtures of polymers and ionic liquids could exhibit dramatic variations in their properties such as solubility. Since it is difficult to perform experiments on dilute polymer/ionic liquid mixtures, theoretical investigations are quickly gaining ground in this novel area. In this chapter, the conformational properties of poly(ethylene glycol) (PEG) in a prototypical ionic liquid 1-methylimidazolium chlo-

ride ([MIM][Cl]), are studied using molecular dynamics simulations. The effect of temperature and of chain length on these conformational properties are investigated. The dihedral angle distribution has also been computed which suggests that at lower temperatures the polymer chain has a finite probability of adopting a helical conformation in the ionic liquid.

Chapter 5

Curcumin is a hydrophobic polyphenolic compound derived from the roots of the herb $Curcumalonga$ and exists in both keto and enol forms. Curcumin is an interesting compound due to its pharmacological effects including anti-inflammatory, antioxidant, antiproliferative and anticancer properties. This chapter describes a molecular dynamics study of the conformational flexibility and dynamics of curcumin inside a lipid bilayer. The lipid bilayer is constructed from dipalmitoylphosphatidylcholine (DPPC) molecules which have a hydrophobic tail and a hydrophilic head. To analyze the diffusion of curcumin in the lipid bilayer, the mean square displacement is studied with time. To investigate the conformational flexibility of curcumin, the radius of gyration and the distance between the oxygen atoms of the hydroxyl group are computed. The free energy of the solvation of curcumin inside the DPPC bilayer is also calculated.

Chapter 6

This chapter contains a brief summary of the main results of the present thesis, their applications, as well as their possible future extensions.

List of Publications

1. Structural and dynamical aspects of PEG/$LiClO_4$ in solvent-mixtures via NMR spectroscopy, Satnam Singh, Raju Nanda and Kavita Dorai, (Under Review 2018).

2. Molecular dynamics study of the translational self-diffusion and liposomal interaction of a fluorinated drug molecule inserted in a phospholipid bilayer, Satnam Singh and Kavita Dorai, (Under Review 2018).

3. Molecular dynamics study of molecular interactions and transport properties of an ionic liquid-polymer mixture, Satnam Singh and Kavita Dorai, (Under Review 2018).

Contents

List of Figures

LIST OF FIGURES

List of Tables

LIST OF TABLES

Chapter 1

Introduction

1.1 Basics of NMR spectroscopy

Nuclear magnetic resonance (NMR) is a widely used analytical method in various fields of research such as physics, chemistry, biology, medicine and pharmaceutical science [1, 2, 3, 4, 5]. NMR is based on the spin of the nucleus. All atomic nuclei possess a spin quantum number, which may have values greater than or equal to zero[6, 7, 8, 9]. When these spins are placed in a homogeneous external magnetic field, they start to precess about the axis of the magnetic field with a specific frequency, known as the Larmor frequency [10, 11, 12, 13]. A net magnetization survives along the axis of the applied magnetic field, which can be manipulated by using radio frequency pulses. NMR has found a wide variety of applications such as the determination of biomolecular structure[14, 15, 16, 17], molecular structure determination of[18, 19, 20] and in magnetic resonance imaging (MRI) [21, 22, 23].

1.1.1 Magnetization and FID

The atomic nuclei having non-zero spin possess a finite dipole moment and behave like tiny bar magnets[24, 25, 26]. The magnetic moment of the nucleus is calculated by using:

$$\mu = \gamma \hbar I. \tag{1.1}$$

where μ is the magnetic moment, γ is the gyromagnetic ratio and I is the nuclear spin quantum number.

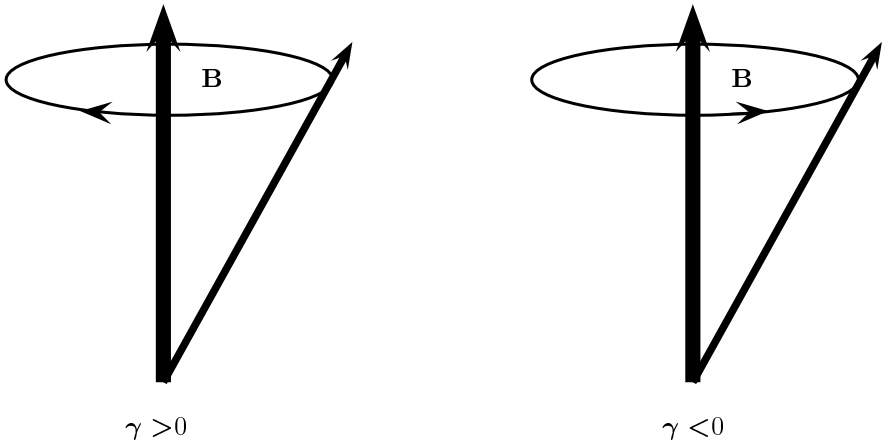

Figure 1.1: Pictorial representation of the relation of the direction of the precession of the spins to the gyromagnetic ratio(γ). For positive γ, the direction of the precession is clockwise, while for negative γ the direction is anticlockwise.

An NMR sample actually contains an ensemble of nuclear spins. Consider a homogeneous magnetic field applied in the z-direction; the nuclear spins will start precessing about z-axis. The z-component of all the spins is added up and gives a resultant magnetization in the z-direction. The pulse in the NMR is electromagnetic radiation having frequency in rf region. Such an rf pulse imposes a torque on the net z-magnetization vector and can rotate it in other directions. After making a transformation to the rotating frame, a 90° rf pulse rotates the magnetization into the $x - y$ plane. After the 90° pulse, the magnetization evolves under the system Hamiltonian and relaxes back to the equilibrium z-direction. During this period, the NMR signal is acquired. This time-domain signal is called free induction decay (FID). The Fourier transformation of this FID transforms it into the frequency domain, corresponding to the NMR resonance peak in frequency space.

1.1.2 Nuclear spin relaxation

The intensity of the NMR signal decay with time. This process is known as relaxation. By this process, the spin magnetization ultimately aligns along the equilibrium z direction. The relaxation process is described by two phenomenological processes[27, 28, 29].

1. Spin-lattice relaxation

2. Spin-spin relaxation

1.1.2.1 Spin-lattice relaxation time (T_1)

Spin-lattice relaxation is also known as longitudinal T_1 relaxation[30]. It is calculated by using inversion recovery method. The figure 1.2 is the pictorial representation of inversion recovery method.

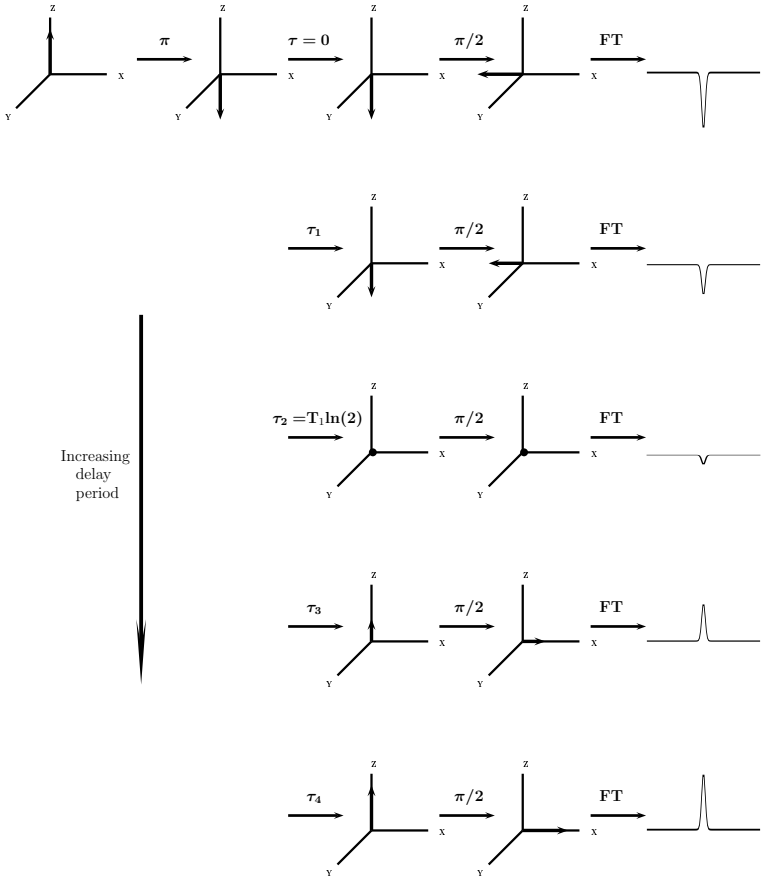

Figure 1.2: Pictorial representation of the T_1 spin-lattice relaxation process. For zero delay time($\tau = 0$), the intensity have negative minimum value. At $\tau = T_1 ln(2)$, the value of the intensity approaches to zero. As the time is increased, the value of the intensity approaches its maximum value.

In the beginning when the sample is placed in the homogeneous magnetic field in the z-direction, the spins start precessing with the Larmor frequency around the z-direction. The components of the magnetization in the $x-y$ plane ($M_x and M_y$) cancel out and a net magnetization survives only along the z-direction. After a 90° pulse, the magnetization is tipped into the $x-y$ plane, where it precesses freely and begins to relax back to the equilibrium z direction. Figure 1.2 shows the pictorial representation of T_1 relaxation. The spin-lattice relaxation time is calculated by using an inversion recovery experiment: an initial 180° pulse is applied along the z-magnetization, then a 90° pulse is applid after a τ delay: $180° - \tau - 90°$. This relaxation is governed by

$$M_z(t) = M_z(t)(1 - 2exp(-\frac{t}{T_1})) \tag{1.2}$$

where $M_z(t)$ is the magnetization in the z direction at time t and $M_z(0)$ is total magnetization in the z direction at equilibrium.

1.1.2.2 Spin-spin relaxation time(T_2)

Spin-spin relaxation is the process which is responsible for dephasing or decay the transverse component of the magnetization and is also called transverse relaxation or T_2 relaxation[30]. This relaxation process occurs due to local inhomogeneities of the magnetic field and is governed by:

$$M_{xy}(t) = M_{xy}(0)exp(-\frac{t}{T_2}) \tag{1.3}$$

where $M_{xy}(t)$ is the value of magnetization at time t and T_2 is the spin-spin relaxation time. Spin-spin relaxation is measured by a simple spin echo experiment $90° - (\Delta - 180° - \Delta) \times L4$ (where Δ is a delay and $L4$ is the loop on $180°$ pulse). Figure 1.3 shows the pictorial representation of the T_2 process.

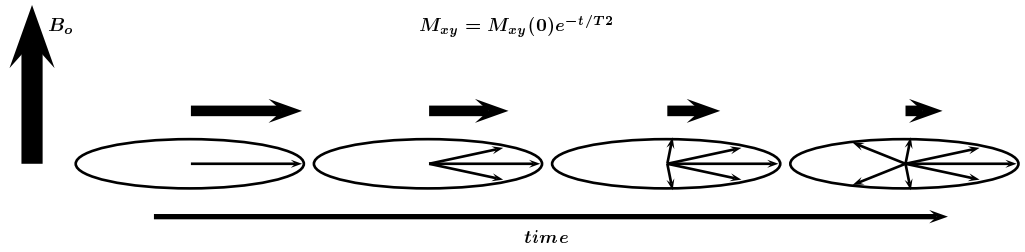

Figure 1.3: Pictorial representation of the T_2 relaxation process.

T_2 relaxation is calculated by using Carr-Purcell-Meiboom-Gill sequence (CPMG) experiment. The figure 1.4 is the pictorial representation of CPMG pulse sequence.

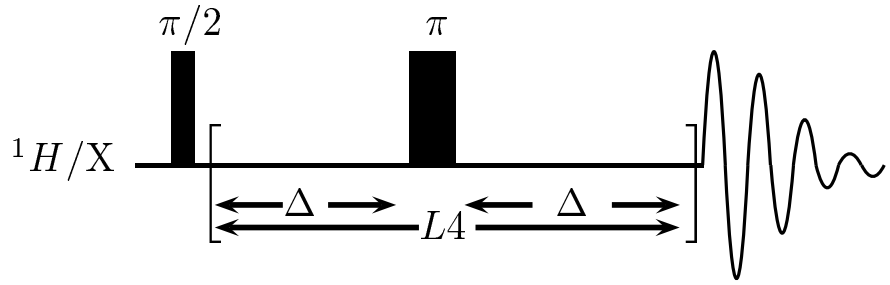

Figure 1.4: Pictorial representation of CPMG sequence.

1.1.3 Spin-echo experiment

A spin echo experiment leads to the refocusing of spin magnetization by an rf pulse. The equilibrium z magnetization is tipped into the $x - y$ plane by a 90° pulse. The spins begin dephasing due to transverse spin-spin relaxation and a 180° pulse is applied to achieve complete refocusing of the spin magnetization.

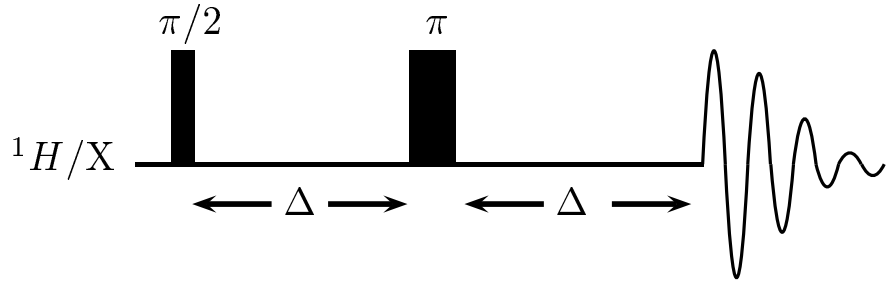

Figure 1.5: Pulse sequence of the spin echo experiment.

1.1.4 Pulsed field gradient diffusion NMR

NMR is a useful technique to study the diffusion on the millisecond time scale[31]. Pulsed field gradient is an NMR technique to study the diffusion, without disturbing the system under investigation. In this method the gradients are used along with the spin echo method for the spatial encoding. When the sample(spins) are placed in the

homogeneous magnetic field, the spins start precessing with the Larmor frequency, which is given by

$$\omega_0 = \gamma B_o \tag{1.4}$$

where γ is gyromagnetic ratio and ω_0 is Larmor frequency and B_o is homogeneous magnetic field. There are two basic pulse sequences used to study diffusion in NMR:

1. Pulse field gradient spin echo

2. Pulse field gradient stimulated echo

Both methods are described below.

1.1.4.1 Pulsed field gradient spin echo

In the pulse field gradient spin echo experiment, the first 90° pulse is applied to tip the magnetization vector into the transverse plane. Then the gradient of the magnetic field (g) is applied in the z-direction. The effective frequency of the precession of the spins becomes

$$\omega_{eff} = \omega_o + \gamma g z \tag{1.5}$$

With the external magnetic field gradient the frequency of the precession of the spins becomes a function of z. It provides spatial labeling to spins. This is called encoding. The phase (phi) of the spins is written as

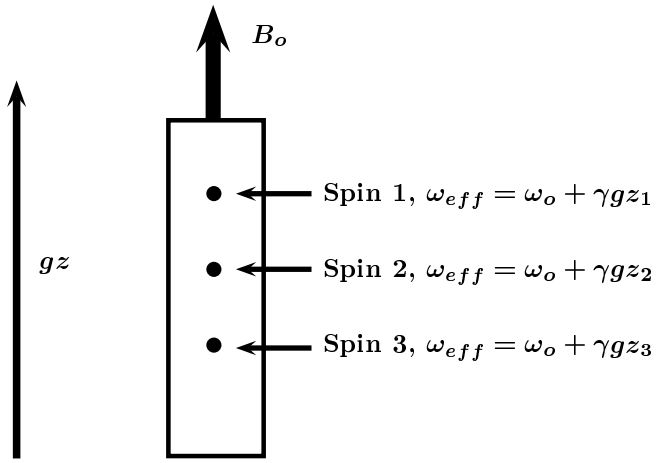

Figure 1.6: When a gradient is applied along the homogeneous magnetic field B_o, the total magnetic field experienced by the spins becomes a function of z. The angular velocity of the spin precession becomes spatially dependent. This figure shows the effective angular velocity of the precession as a function of time.

$$\phi(z) = \phi_o + \int \gamma g z dt \tag{1.6}$$

Due to the diffusion, the spins change their respective positions. After this the refocusing pulse($180°$) is applied and the same intensity of the magnetic field gradient is applied to decode the signal. The signal attenuation reflects the diffusion process.

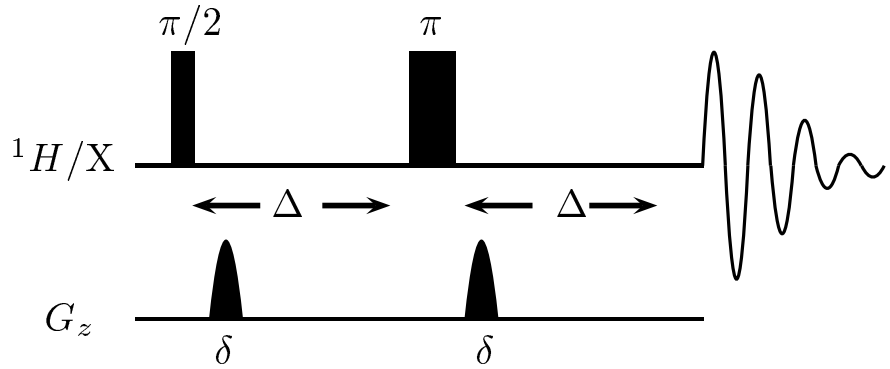

Figure 1.7: Pictorial representation of the pulse program of the pulsed field gradient spin echo NMR experiment. The gradient pulses are used to dephase the magnetization vector.

1.1.4.2 Pulsed field gradient stimulated echo

Pulsed field gradient stimulated echo pulse sequence is another method to study the diffusion by NMR[32]. In this method, three 90° pulses are used along with the gradients. The basic pulse sequence of stimulated echo is $90^\circ - \tau/2 - 90^\circ - \tau/2 - 90^\circ$. The first 90° pulse aligns the magnetization in the $x - y$ plane.

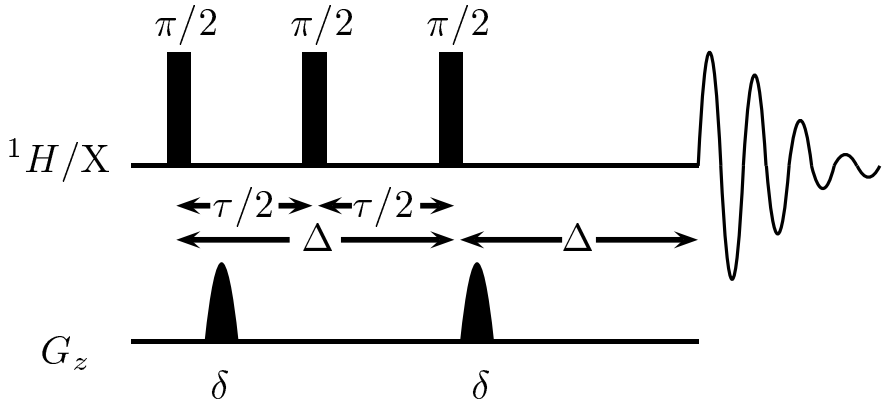

Figure 1.8: Pulse sequence of the pulsed field gradient stimulated echo NMR experiment. The gradient pulses are used to dephase the magnetization vector.

Then the gradient is applied to dephase the spins. The second 90° pulse is applied to tip the dephased spins into $x - z$ plane. The z-component of the magnetization does not precess but remains aligned along the direction of the magnetic field. The last 90° pulse is used to align the spins in the transverse plane and a gradient pulse is used to rephase the spins. The diffusion is calculated from the attenuation of the signal.

1.1.4.3 Stejskal-Tanner equation

Stejskal-Tanner equation is an important equation in NMR diffusion measurements[33, 34, 35]. It is used to calculate the diffusion coefficient. The equation combines Fick's second law with Bloch equation:

$$A = A_0 exp[-D\gamma^2\delta^2 g^2(\Delta - \frac{\delta}{3})] \tag{1.7}$$

where A is the intensity of the NMR peak, D is the diffusion coefficient, γ is the gyromagnetic ratio, δ is the duration of the magnetic gradient pulse, g is intensity of the gradient pulse and Δ is the diffusion time.

1.1.4.4 Applications of pulsed field gradient NMR

The pulsed field gradient NMR experiment is a key technique for various magnetic resonance applications[36, 37]. An important application is in the area of magnetic resonance imaging (MRI). The technique is also used to study the diffusion dynamics of the molecules[38]. In the Diffusion Ordered Spectroscopy (DOSY) experiment[39], the components of the mixture are resolved depending upon the diffusivity of the molecule. The DOSY method is also used to determine the size of the molecule and the process of aggregation occurring in the mixture of solutions[40]. Another application of the pulse field gradient is in solvent suppression in the NMR experiment[41]. Sometimes there are various unwanted solvent peaks in the NMR spectrum. The pulsed field gradient technique is an effective method to suppress such unwanted peaks. Gradient pulses are used in the phase cycling technique. It is routinely used in magnetic resonance to remove background signals and to suppress unwanted free induction decays (FID) and spin echoes. In this the desired coherence pathway is selected by using the gradient pulses [31].

1.2 Molecular dynamics simulations

Numerical simulations have long been used to understand the properties of ensembles of molecules in terms of their structure and the microscopic interactions between them. There are two types of computational techniques used [42, 43]: molecular dynamics (MD) simulations and Monte Carlo (MC) simulations.

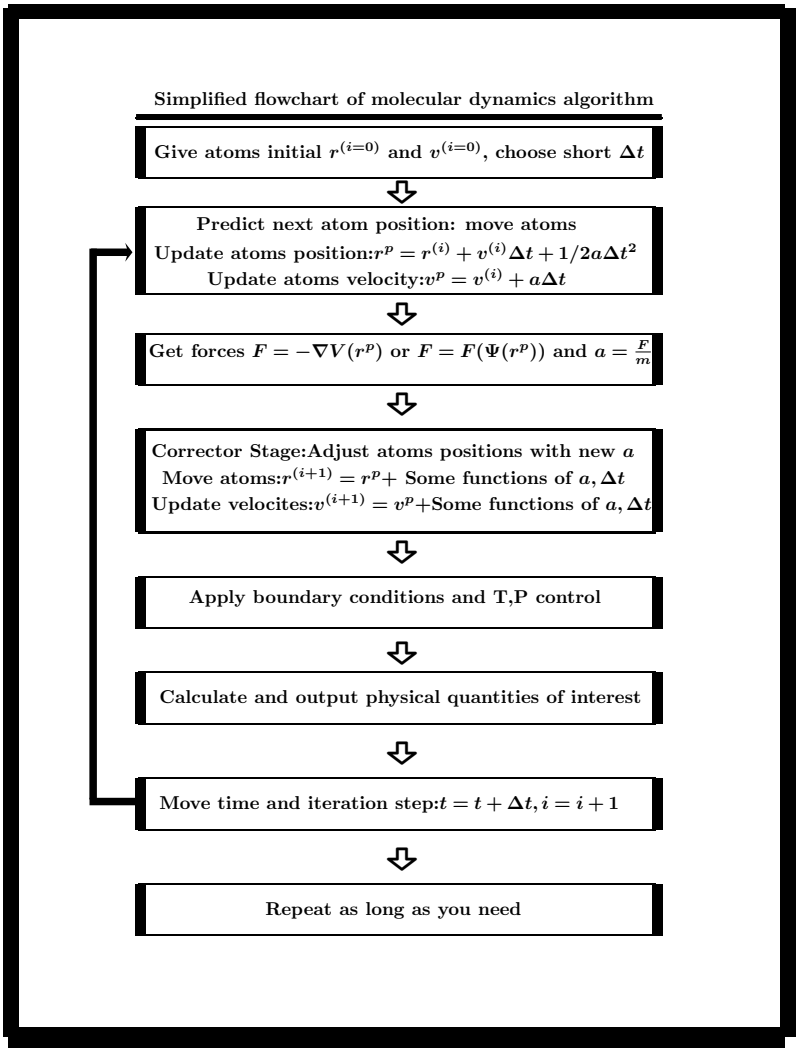

Figure 1.9: Flowchart of a typical molecular dynamics simulation.

MD simulations give insights into molecular properties such as transport coefficient, time dependent responses to perturbation and rheological properties and are hence often preferred over MC simulations. Molecular dynamics is the computational study of the physical motion of the atoms and the molecules. The molecules or atoms freely interact with each other for a fixed time and then the system is allowed to evolve, with interactions being governed by the forcefield.

The trajectories of the molecules or the atoms are calculated by solving the Newton equations of motion. The force between particles (molecules or atoms) is calculated

from the interatomic or intermolecular potential. The negative gradient of the potential gives the force. Examples of some of the most commonly used molecular dynamics simulation packages are AMBER, CHARMM, GROMOS, and OPLS[44, 45, 46, 47]. For the simulation, the initial conditions are provided externally in a file. The temperature distribution is computed according to the Maxwell Boltzmann distribution. Figure 1.9 depicts the flowchart of a typical molecular dynamics simulation. The results of the MD simulations are usually validated by comparing with experiments. MD simulations are extensively used in chemical physics, material science, biomolecular modeling and pharmaceutical science[48, 49]. MD simulations are used for quantitative estimation of quantities such as binding constants of ligands to receptors and for the prediction of spatial molecular structure of the big proteins. This is helpful in refining the structure when compared with X-ray and NMR experimental data. The MD simulations are also extremely helpful in the field of the drug discovery [50]. MD simulations are also useful for the calculation of the thermodynamical properties of the molecular systems such as free energy, entropy contribution etc. Despite several advantages, MD simulations have several limitations as well. The time and the size are the biggest limitations of MD studies. The smallest integration step for the simulation is of the order of femto seconds ($\approx$ 2fs). In nature the size of the systems is huge, which cannot be realistically simulated by the MD simulations. The order of the number of the atoms simulated in the simulations is up to 100000. Due to small integration time steps and large number of atoms, there are billions of calculations.

So it is extremely time consuming. In molecular dynamics simulations the forcefields are the main models. If the potentials in the forcefields mimic the force experienced by the real atoms, then the simulation become realistic. But the forcefield taken in the simulations are approximated. To decrease the time of the simulations, the long range interactions are truncated within some range.

1.2.1 Forcefields and interactions

The force field is a key part of any molecular dynamics simulation. It refers to the functional form and the parameters used to calculated the interatomic potential energy. The parameters of the force field are derived from experiments or from the quantum mechanical calculations. There are mainly three type of force fields which are used in

molecular dynamics simulations:

1. All atom: In this type, the parameters are provided to the individual atoms. All atoms are considered as the interacting units. This force field is highly time consuming.

2. United atom: In the united atom force field, the parameters are provided to all atoms of the molecule except the non polar hydrogen. This force field is less time consuming.

3. Coarse grained: In this force field, groups of atoms are considered as interacting beads. In this force field the number of interacting units are reduced, so it is less time consuming. Martini coarse grained is one example of this force field[51].

The total energy in the molecular dynamics simulation is written as

$$E_{total} = E_{bonded} + E_{nonbonded} \tag{1.8}$$

The bonded interactions of the atoms are the interactions which are occurs through the bond. The non-bonded interactions of the atoms are the interactions which occur through space.

The bonded interactions can be categorized as:

1. Bond: This interaction occurs due to the atomic bonds. The bond between two atoms is considered analogous to a spring. So the contribution of this factor due to the stretching of the bond is written as

$$V_{bond}(r_{ij}) = \frac{1}{2}k^b_{ij}(r_{ij} - b_{ij})^2 \tag{1.9}$$

   where k_{ij} is the spring constant between two atoms, r_{ij} is the distance between two atoms and b_{ij} is the mean distance between two atoms.

2. Angle: The vibration of the angle between triplet atoms contributes to the potential energy. It is also taken as a harmonic potential:

$$V_{angle}(\theta_{ijk}) = \frac{1}{2}k^\theta_{ijk}(\theta_{ijk} - \theta^0_{ijk})^2 \tag{1.10}$$

   where k^θ_{ijk} is a constant analogous to the spring constant, θ_{ijl} is the angle and the θ^0_{ijk} is mean angle in triplet atoms.

3. Dihedrals: Dihedral is the angle between two planes. It involves a group of four atoms. It is further divided into two parts

   (a) Proper Dihedral: For the proper Dihedral, the potential energy is

   $$V_{prodihed}(\phi_{ijk}) = k_\phi(1 + cos(n\phi - \phi_s)) \tag{1.11}$$

   where ϕ is the angle between planes.

   (b) Improper Dihedral: The potential energy due to the Improper Dihedral is

   $$V_{impdihed}(\xi_{ijkl}) = \frac{1}{2}k^{\xi}_{ijk}(\xi_{ijkl} - \xi^0_{ijkl})^2 \tag{1.12}$$

The non bonded interaction of the force field have following terms

1. Coulomb interaction: Coulomb interaction is the main term in the non-bonded interaction. It is due to the charge on the interacting atoms. It is written as:

   $$V_{Cou}(r_{ij}) = f\frac{q_i q_j}{\epsilon_r r_{ij}} \tag{1.13}$$

   Where r_{ij} is the distance between the interacting ith and jth atoms with the charge q_i and q_j.

2. Lennard-Jones interaction: The Lennard-Jones interaction potential is written as:

   $$V_{LJ}(r_{ij}) = \frac{C^{(12)}_{ij}}{r^{12}_{ij}} - \frac{C^{(6)}_{ij}}{r^6_{ij}} \tag{1.14}$$

   It is made up of two terms one is attractive and other is repulsive. $C^{(12)}_{ij}$ and $C^{(6)}_{ij}$ are the constants and depends on atom pairs.

1.2.2 Constraints

In molecular dynamics, the constraints are helpful to simulate a rigid body by using Newton's equation of motion. These are used to maintain the distance between two atoms. There are various constraint algorithms like LINCS and SHAKE are used in the molecular dynamics simulations [52, 53]. The LINCS is the default constraint algorithm used in the GROMACS software package.

1.2.3 GROMACS software package

GROningen MAchine for Chemical Simulations(GROMACS) is a widely used open source package used in dynamical simulations of molecules[54, 55]. It includes a rich set of calculation tools, preparation and analysis tools. Advanced techniques like free energy calculation are also supported in this package[56]. It also supports the multithreading, CPU-GPU acceleration, state of the art 3D domain decomposition, and also parallelization. The GROMACS package is written in C and C++ language. Following force filed are the default present in GROMACS

1. AMBER(Assisted Model Building with Energy Refinement): It is family of the force fields originally developed by Peter Kollman's group[44]. The potential energy function of the AMBER force field is

$$\begin{aligned} V(r^N) &= \sum_{\text{bonds}} k_b(l-l_0)^2 + \sum_{\text{angles}} k_a(\theta-\theta_0)^2 + \sum_{\text{torsions}} \sum_{n} \frac{1}{2} V_n[1+\cos(n\omega-\gamma)] \\ &+ \sum_{j=1}^{N-1} \sum_{i=j+1}^{N} f_{ij}\{\epsilon_{ij}\left[\left(\frac{r_{0ij}}{r_{ij}}\right)^{12} - 2\left(\frac{r_{0ij}}{r_{ij}}\right)^{6}\right] + \frac{q_i q_j}{4\pi\epsilon_0 r_{ij}}\} \end{aligned} \tag{1.15}$$

   Where all terms have their usual meanings.

2. CHARMM(Chemistry at Harvard Macromolecular Mechanics): CHARMM force field is developed by Martin Karplus and his group. Several versions of the CHARMM are available in the GROMACS package. The potential energy function of the CHARMM force field is following[45].

$$\begin{aligned} V &= \sum_{bonds} k_b(l-l_0)^2 + \sum_{angle} k_a(\theta-\theta_0)^2 + \sum_{dihedrals} k_\phi\left[1+\cos\left(n\phi-\delta\right)\right] \\ &+ \sum_{\text{impropers}} k_\omega\left(\omega-\omega_0\right)^2 + \sum_{\text{Urey}-\text{Bradley}} k_u\left(u-u_0\right)^2 \\ &+ \sum_{j=1}^{N-1} \sum_{i=j+1}^{N} f_{ij}\{\epsilon_{ij}\left[\left(\frac{r_{0ij}}{r_{ij}}\right)^{12} - 2\left(\frac{r_{0ij}}{r_{ij}}\right)^{6}\right] + \frac{q_i q_j}{4\pi\epsilon_0 r_{ij}}\} \end{aligned} \tag{1.16}$$

3. GROMOS(Groningen Molecular Simulation): It is general purpose molecular dynamics force field. The potential energy function of the GROMOS force field

is following[46]

$$\begin{aligned} V &= \sum_{bonds} k_b(l^2 - l_0^2)^2 + \sum_{angle} k_a(cos\theta - cos\theta_0)^2 + \sum_{dihedrals} k_\phi \left[1 + \cos\left(n\phi - \delta\right)\right] \\ &+ \sum_{Improper} k_a(\xi - \xi_0)^2 + \sum_{\text{impropers}} k_\omega \left(\omega - \omega_0\right)^2 \\ &+ \sum_{j=1}^{N-1} \sum_{i=j+1}^{N} f_{ij}\{\epsilon_{ij}\left[\left(\frac{r_{0ij}}{r_{ij}}\right)^{12} - 2\left(\frac{r_{0ij}}{r_{ij}}\right)^{6}\right] + \frac{q_i q_j}{4\pi\epsilon_0 r_{ij}}\right\} \end{aligned} \tag{1.17}$$

4. OPLS(Optimized Potentials for Liquid Simulations): The OPLS force field is developed by Prof. William L. Jorgensen[47]. The potential energy function of this field is following.

$$\begin{aligned} V(r^N) &= \sum_{\text{bonds}} k_b(l - l_0)^2 + \sum_{\text{angles}} k_a(\theta - \theta_0)^2 + \sum_{\text{dihedrals}} (\frac{V_1}{2}[1 + \cos(\phi - \phi_1)] \\ &+ \frac{V_2}{2}[1 - \cos(2\phi - \phi_2)] + \frac{V_3}{2}[1 + \cos(3\phi - \phi_3)] + \frac{V_4}{2}[1 - \cos(4\phi - \phi_4)]) \\ &+ \sum_{j=1}^{N-1} \sum_{i=j+1}^{N} f_{ij}\{\epsilon_{ij}\left[\left(\frac{r_{0ij}}{r_{ij}}\right)^{12} - 2\left(\frac{r_{0ij}}{r_{ij}}\right)^{6}\right] + \frac{q_i q_j}{4\pi\epsilon_0 r_{ij}}\right\} \end{aligned} \tag{1.18}$$

GROMACS is a useful tool to calculate various molecular properties[57]. Few properties and their respective commands are given below

1. Diffusion: It can calculate the diffusion coefficient from the trajectories obtained from the molecular dynamics simulation. It originally extracts the mean square displacement from the trajectories with the time. The slope of that trajectory gives the diffusion coefficient. "gmx msd" is the command used to calculate it.

2. Radial distribution function: The radial distribution function are the pair correlation functions gives the probability of one particle w.r.t second particle as the function of the distance. To calculate radial distribution function in the GROMACS "gmx rdf" command is used.

3. Radius of gyration: Radius of gyration is the quantity with which the size of the molecule can be estimated. It can be calculated by using GROMACS command ”gmx gyrate”.

4. Dihedral angles: Dihedrals angle are very useful to study the geometric isomerism. The command to calculate Dihedral angle is "gmx angle".

5. Root mean square deviations in structure: Root mean square deviations is very useful to calculate the variation of structure during the dynamics. This tool is useful to study the dynamics of large proteins and long chain polymers. The command to use this tool is "gmx rmsd"

1.3 Fundamentals of molecular diffusion

Diffusion is the process in which the molecules intermingle as a result of their kinetic energies. It is the random movement of particles. During diffusion, the particles make numerous collisions with each other. Diffusion word is derived from latin word diffundere. The meaning of this word is spread out. There are lots of examples of diffusion in nature such as: diffusion of chemical fumes in air or a food color dye dropped in water.

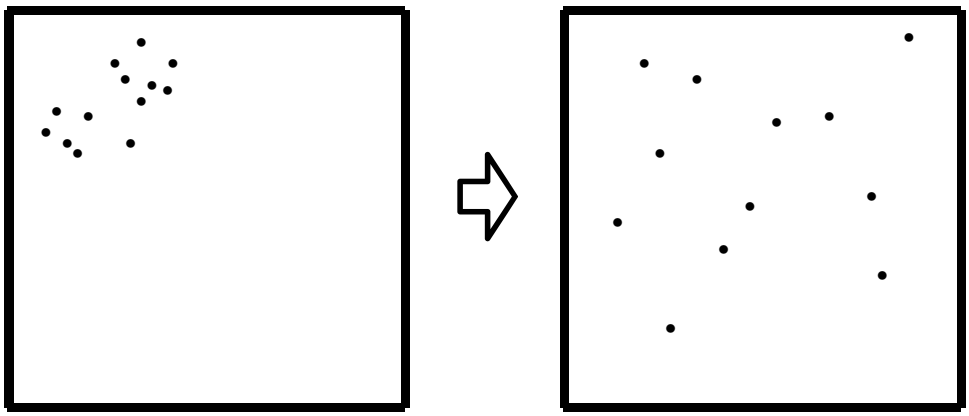

Figure 1.10: Depiction of particles in a box diffusing with time.

Diffusion is the process by which matter is transported by the random motion of the molecules and was understood by Adolf Fick in 1855 using the mathematics of heat transfer equations. The transfer of the heat is proportional to the temperature gradient. In the diffusion phenomenon, the temperature is analogous to the concentration.

1.3.1 Fick's First law

In an isotropic medium, the rate of transfer of a diffusing material through a unit area for unit time is proportional to the concentration gradient[58]. Fick's first law can hence be written as:

$$F = -D\frac{\partial C}{\partial x}. \tag{1.19}$$

where F is the rate of transfer per unit area, C is concentration of the diffusing substance, x is the spatial coordinate and D is the diffusion coefficient.

In an anisotropic medium, the diffusion coefficient becomes a tensor, and the above equation is written as:

$$\begin{pmatrix} F_x \\ F_y \\ F_z \end{pmatrix} = - \begin{pmatrix} D_{xx} & D_{xy} & D_{xz} \\ D_{yx} & D_{yy} & D_{yz} \\ D_{zx} & D_{zy} & D_{zz} \end{pmatrix} \begin{pmatrix} \frac{\partial C}{\partial x} \\ \frac{\partial C}{\partial y} \\ \frac{\partial C}{\partial x} \end{pmatrix}. \tag{1.20}$$

where F_x, F_y and F_z are the rates in the directions x, y and z, respectively.

1.3.2 Fick's second law

Fick's second law gives insights into change in the concentration with time. In an isotropic medium, in one dimension, this is written as:

$$\frac{\partial C}{\partial t} = D\frac{\partial^2 C}{\partial x^2} \tag{1.21}$$

where C is concentration of the diffusing material, D is diffusion coefficient, x is spatial coordinate and t is time. In a more general form, the above equation is written as:

$$\frac{\partial C}{\partial t} = div(D.gradC) \tag{1.22}$$

where div is the divergence and $grad$ is the gradient. For an anisotropic medium the above equation is written as:

$$\frac{\partial C}{\partial t} = - \begin{pmatrix} \frac{\partial}{\partial x} \\ \frac{\partial}{\partial y} \\ \frac{\partial}{\partial x} \end{pmatrix} \begin{pmatrix} D_{xx} & D_{xy} & D_{xz} \\ D_{yx} & D_{yy} & D_{yz} \\ D_{zx} & D_{zy} & D_{zz} \end{pmatrix} . \begin{pmatrix} \frac{\partial C}{\partial x} \\ \frac{\partial C}{\partial y} \\ \frac{\partial C}{\partial x} \end{pmatrix} \tag{1.23}$$

where C is concentration and Ds are diffusion coefficients, which are taken as constant.

1.4 Organization of the thesis

The organization of the thesis is described below: Chapter 2 describes a molecular dynamics study of the dynamics of a drug molecule pazufloxacin drug inside a bicellar lipid membrane. The lipid membrane is created from two different lipids 1,2-dihexanoyl-sn-glycero-3-phosphocholine (DHPC) and 1,2-Dimyristoyl-sn-glycero-3-phosphocholine (DMPC). The nature of the diffusion, radial distribution function and the time correlation function of the drug in the lipid bilayer is presented in this chapter. Chapter 3 deals with the an experimental study of the dynamics of six different polyethylene glycol polymers and lithium perchlorate in three different molecular solvents, using pulsed field gradient NMR and relaxation NMR. The activation energy and the rotational correlation time are calculated from the experimental data. Chapter 4 presents a molecular dynamics study of the dynamics of PEG polymer in an imidazolium-based ionic liquid. The radial distribution function, radius of gyration and various other aspects are probed. Chapter 5 presents a molecular dynamics study of the diffusion of a curcumin molecule inside a DPPC lipid membrane, at two different temperatures. To study the dynamics, both keto and enol forms of the curcumin are investigated. The nature of the diffusion, the radius of gyration and the free energy of the solvation are presented. Chapter 6 contains a brief summary of the work done in this thesis.

Chapter 2

Molecular dynamics simulation study of the translational self-diffusion and liposomal interaction of a fluorinated drug molecule inserted in a phospholipid bilayer

2.1 Background and Motivation

Understanding the molecular mechanism of drug insertion into membrane bilayers is significant for drug design and delivery studies. For drug action to occur, the drug must be able to penetrate the lipid bilayer membrane barrier present on the biological cell surface. Lipid bilayers are semipermeable barriers in biological cells which control the movement of several molecules into the cells [59]. Bicelles are model membrane mimetics composed of long-chain dimyristoylphosphatidylcholine (DMPC) molecules which get organized in a bilayered disc or vesicle with high curvature, stabilized by short-chain dihexanoylphosphatidylcholines (DHPC) molecules [60]. Bicelles have been extensively used as model membranes to study structure and dynamics of membrane-associated peptides and proteins and to study the interactions of drug molecules with cell membranes. Isotropic bicelles are usually disc-shaped entities with the DHPC molecules on the rim and the DMPC molecules clustered together on the planar sec-

tion. Phospholipid bicelles are often used as membrane mimetics and theoretical and experimental studies of drug and bicelle interactions provide interesting and useful insights. Biomembrane fluidity has been shown to be strongly affected by the presence of drug molecules, which modifies their biological and physiological properties [61]. When the drugs are encapsulated in the bicelles, the toxicity of the drug is reduced, and efficacy is increased.

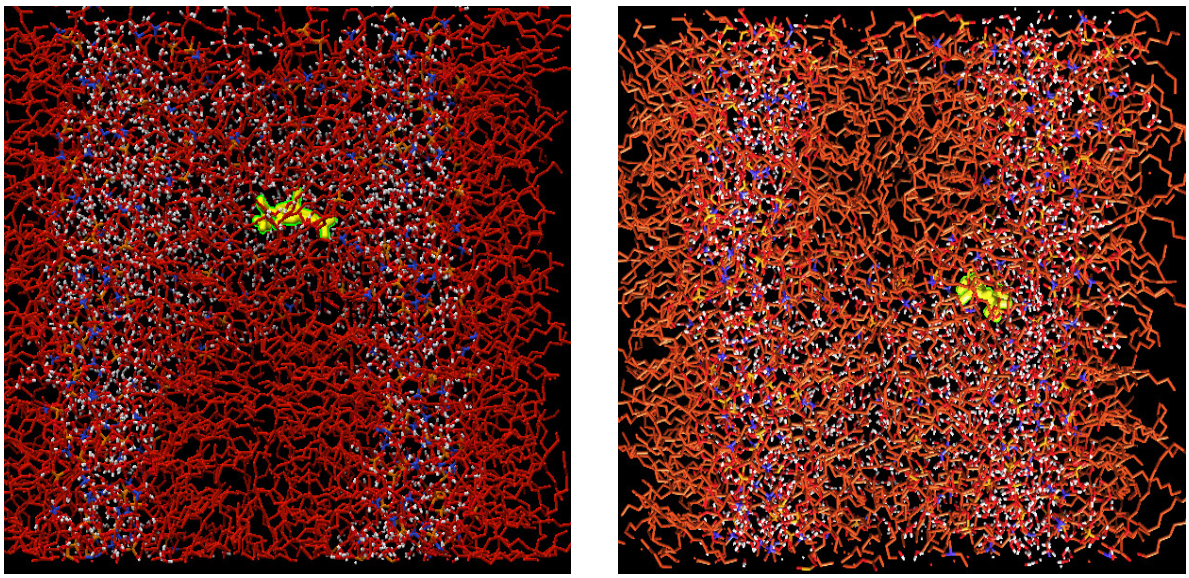

Figure 2.1: Snapshots of drug-lipid bilayer system, showing results of MD simulation at 0 ns (left panel) and at 200 ns (right panel). The drug molecule is displaced along the x-direction (normal to the membrane).

Several studies of the interaction between drugs and lipid bilayers have been reported using experiments and theory [62]. MD simulations are able to provide structural and dynamic information of drug-bilayer interactions, often over a range of time scales and length scales which are not amenable to experimental studies [63]. The insertion, preferred positioning and dynamics of the drug molecule in the lipid bilayer has been extensively studied using molecular dynamics simulations [64, 65, 66]. The interaction of drugs and membranes and their investigation using different experimental methods and molecular dynamics simulations has been extensively discussed in a recent review article [67]. The partitioning of anti-inflammatory drugs in lipid membranes has been studied via molecular dynamics simulations [68]. NMR

spectroscopy provides atomic-level information under nearly physiological conditions and is hence widely used for drug-substrate studies including conformation, dynamics, affinity and binding-site identification. Other techniques such as confocal Raman microscopy have also been used to study drug-lipid interactions [69]. The interaction of drugs and different membrane mimicking environments such as SDS micelles have been extensively studied using NMR spectroscopy and MD simulations [70, 71]. The action of an antihypertensive drug AT1 antagonist losartan via its interaction with SDS micelles was studied using MD simulations and NMR spectroscopy [72]. The effect of drug insertion on the mesoscopic properties of a phospholipid bilayer has been investigated [73] and the permeability of drugs through a lipid bilayer has been studied via dual-resolution molecular dynamics [74].

Drug binding to the liposomal surface is often dependent on the head group and the nature of the drug and has been extensively studied [75, 76]. The action of a drug not only depends on the structure of the drug, but also depends on its ability to bind with the lipid cell membrane [77]. Lipid-drug interactions are important to predict the pharmacokinetic properties of drug molecules, such as their transport, accumulation and efficacy. Such biophysical interactions may be altered by a change in the lipid composition of the cells and tissues to which the drug binds, due to which, target-specific drug design and drug delivery can be explored [78].

The head group region of a lipid is polar and forms the hydrophilic part of the membrane while the tails are hydrocarbon chains which are non-polar and lipophilic. It is thus to be expected that molecules with high polarity will be incorporated into polar head group region, while non-polar molecules will aggregate in the middle of the lipid bilayer [79]. However this raises an interesting question about the degree of penetration into the lipid bilayer of fluorinated molecules which are neither hydrophilic nor lipophilic in character [80]. In this chapter, this interesting question has been explored via MD simulations of the interaction of a fluorinated drug molecule, pazufloxacin, with a phospholipid bicelle. Pazufloxacin is a fluoroquinolone which are molecules that have long been used as extremely potent and broad-spectrum antibacterial drugs [81, 82]. Molecular dynamics simulations were performed on this drug molecule oriented in a phospholipid bicelle, which acts like a membrane-mimetic environment, and obtain useful information about its structural and dynamic behavior. There are so many limitation of experimental studies. The experimental studies

are more expensive than simulation studies. Sometimes the used chemicals are very costly. In the experimental studies, The conditions are not real.

The drug-bicelle interactions were investigated as a function of temperature (at two different temperatures 293 K and 303 K when the bicelle is in a gel phase and a liquid-crystalline phase, respectively). The radial distribution functions were computed between different head and tail groups of the DMPC and DHPC molecules with water, between the DMPC tail group and the drug molecule, and between the drug molecule and the water. The results contained in this chapter corroborate the hydrophobic or hydrophilic character of the different lipid tail and head groups. It is interesting to note that although the drug molecule is for the main part hydrophobic, it still gets trapped inside the lipid bilayer along with the water molecules. The transport behavior of the drug molecule inside the bicellar environment was also studied as a function of temperature, and it was inferred that the drug exhibits anomalous diffusion (in the sub-diffusive regime) when the bicelle is in the gel phase as well as in the liquid-crystalline phase.

2.2 Computational parameters

All MD simulations were performed using the GROMACS 4.5.6 software package [83], using the GROMOS 53a6 force field [84]. The structure and topology of the lipid molecules were downloaded from the Automated Topology Builder website [85], while the structure and standard GROMOS parameters for the drug molecule were obtained from the PRODRG server [86]. The composite drug-lipid bilayer system was first subjected to a 1 ns MD simulation for energy minimization. These minimized coordinates were fed into the final MD simulation which ran for 200 ns. The MD rectangular unit cell contained 128 DMPC molecules, 85 DHPC molecules, 2000 water molecules and a single drug molecule. The system was constrained in a $11 \times 6 \times 6$ nm^3 box and periodic boundary conditions were imposed, with y- and z- directions corresponding to the bilayer lateral and the x- direction corresponding to the bilayer normal, respectively. The ensemble adopted was NVT (constant particle numbers, volume and temperature). The temperature was controlled at 293 K using a modified Berendsen thermostat [87]. At this temperature, the model membranes are in a gel state. The electrostatic interaction was controlled using the particle-mesh Ewald (PME) method

using a fourth order cutoff for the direct space sum [88]. For the van der Waals interaction, the Verlet cutoff scheme was used to restrict the potential to a short range of 1 nm. Velocities were assigned from the Maxwell distribution. The equation of motion was integrated with the leap-frog integrator with a 2 fs integration time step. All bonds were constrained using the LINCS algorithm of order four [52].

2.3 Results & Discussion

2.3.1 Drug penetration into lipid bilayer

In order to be able to penetrate lipid bilayers and retain the desirable property of aqueous solubility, drug molecules are amphipathic i.e different molecular moieties of the molecule are either attracted or repelled by water. Most non-steroidal drugs contain aromatic rings and occur in both uncharged as well as anionic forms. The aromatic rings are the hydrophobic component and various polar functional groups are the hydrophilic part. In general charged molecules are usually congregated closer to the water/membrane interface as compared to uncharged molecules and the results of both experiments and simulations show that such drugs cause only minor perturbations to the structure of the lipid bilayer when they penetrate into the lipid. The preferred binding sites for amphipathic membrane-binding molecules are the water/membrane interface and the lipid headgroup/tailgroup interface. It has been shown that increasing the membrane asymmetry can enhance the drug penetration into the membrane. MD simulations of the drug pazufloxacin inserted in a phospholipid bicellar system (consisting of DHPC and DMPC) were performed in order to study the conformational dynamics and the diffusion pathway of the drug molecule. The drug molecule was initially placed at the center of the lipid bilayer. It is evident from the simulations that the drug diffuses along the direction of the normal to the membrane bilayer (denoted as the x-direction for the simulation). The positioning of the drug in the lipid bilayer is shown in snapshots of the MD trajectory in Figure 2.1. To get a more accurate profile of the relative positioning of the drug molecule within the lipid bilayer, the number density of the atoms in the drug molecule as a function of displacement along the membrane normal was also calculated. The results are depicted in Figure 2.2 and corroborate the model of the drug being displaced along the membrane normal direction. Within a few

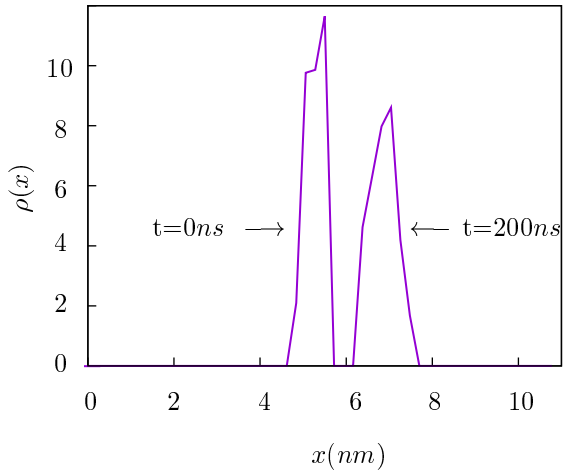

Figure 2.2: Plot of number density $\rho(x)$ of drug molecule atoms along the membrane normal (chosen as x-direction in the simulation).

seconds of the simulation, negative membrane curvature gets induced due to electrostatic attractions which help induce hydrophilic holes through which the drug molecule penetrates into the lipid bilayer.

2.3.2 Radial distribution function

A pair correlation function or a radial distribution function ($g(r)$) (RDF) is the probability of finding a pair of molecules a distance r apart, relative to the probability for a uniform distribution at the same density [89]:

$$g(r) = 4\pi r^3 \rho(r) dr \tag{2.1}$$

where ρ is the number density and r is the distance from the reference molecule. The radial distribution functions for the center of mass of each molecule considered in this work were computed from the trajectories of the simulation. These radial distribution or pair correlation functions give an intuitive structural insight into which part of the lipid bilayer is correlated with atoms on the drug molecule. The peak heights in these radial distribution function plots are dependent on the correlation or local density between the sites considered.

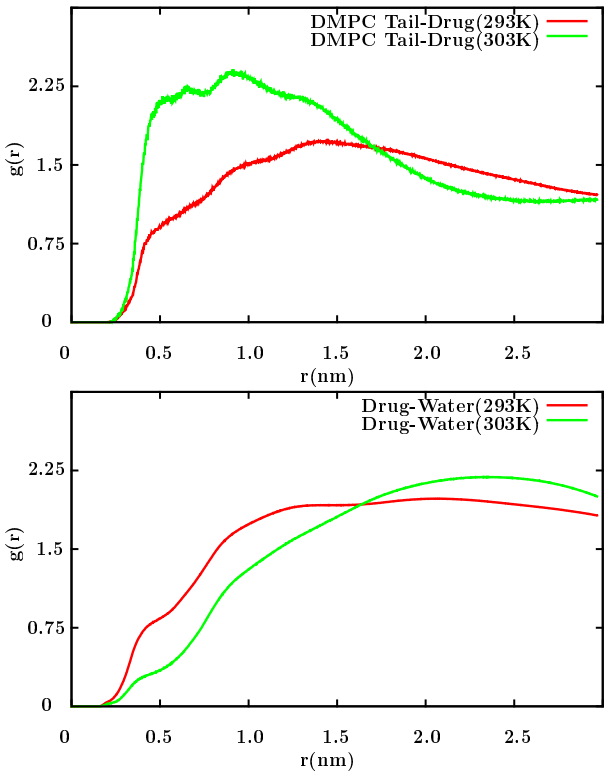

Figure 2.3: Radial distribution functions between the DMPC tailgroup and the drug molecule (top panel) and the drug molecule and water (bottom panel). The x-axis is distance in angstroms.

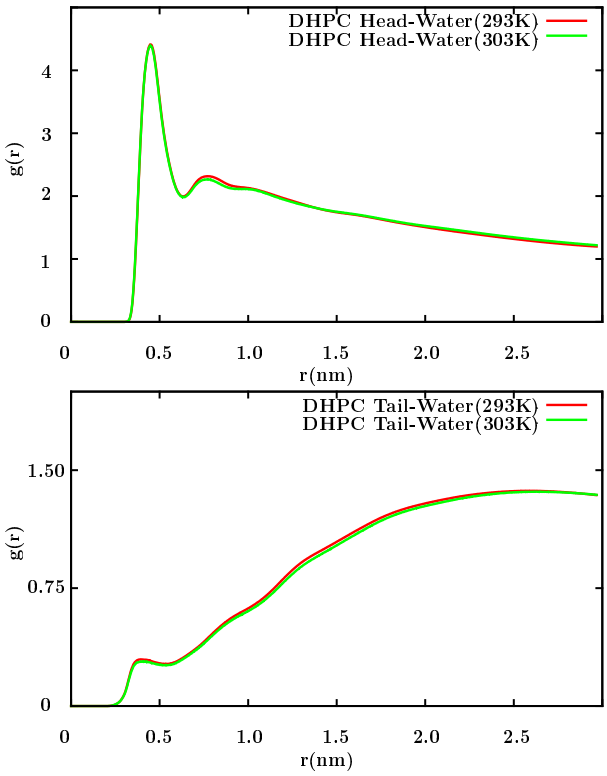

Figure 2.4: Radial distribution functions between the DHPC headgroup and water (top panel) and the DHPC tail and water (bottom panel). The x-axis is distance in angstroms.

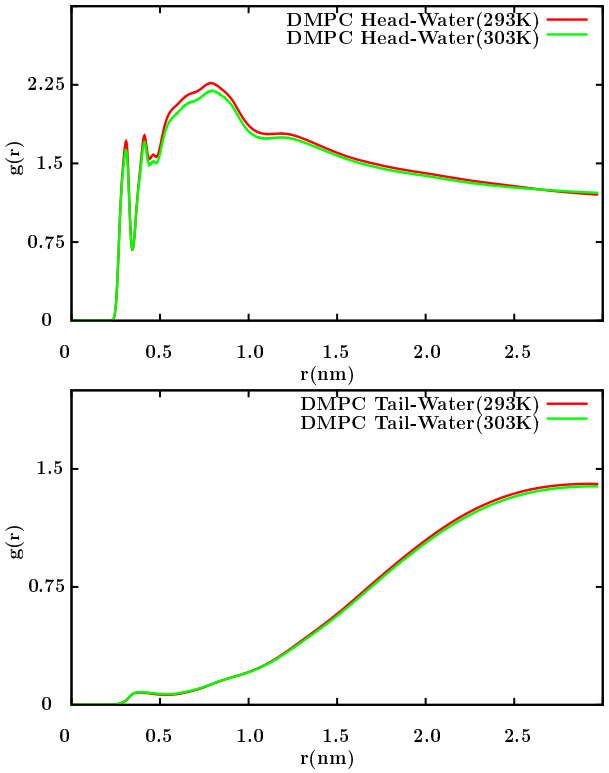

Figure 2.5: Radial distribution functions between the DMPC headgroup and water (top panel) and the DMPC tail and water (bottom panel). The x-axis is distance in angstroms.

Radial distribution functions of different lipid groups and water molecules were analyzed relative to the drug molecule, to characterize the position of the drug in the biomembrane mimetic. The following pairs were studied: (1) DMPC headgroups with water (2) DMPC tail groups with water (3) DHPC headgroups with water (4) DHPC tail groups with water (5) DMPC tail with drug and (6) Drug with water. All the RDFs were computed in both the gel phase and the liquid-crystalline phase of the bicelle.

Figure 2.5 depicts the radial distribution function of DMPC head groups and water. The DMPC headgroup is hydrophilic and gives a high correlation close to 0.30nm, as in the lipid membrane, the head groups are aligned toward the inside of the layer and water is sandwiched inside the bilayer. The height of this peak is the same at both the temperatures (293 K and 303 K). This suggests that although the bicellar phase has changed with temperature, the probability distribution remains the same. Since the DMPC tail groups are hydrophobic, there is no sharp peak observed in the

RDF of the DMPC tail with water (Figure 2.5 bottom panel). Figure 2.4 shows the radial distribution function of DHPC head groups and water. This RDF shows a very strong correlation with water close to 0.5 nm. The DHPC tail on the other hand is hydrophobic and shows an extremely weak correlation with water, close to 0.45 nm (Figure 2.4 bottom panel). The top panel in Figure 2.3 shows the radial distribution function of the DMPC tail with the drug molecule. Since both the DMPC tail and the drug are hydrophobic, the drug is trapped inside the bilayer, while the DMPC tail tends to align toward the outside. The RDF shows a correlation peak close to 0.45 nm. The correlation is stronger in the liquid-crystalline phase (303K) as compared to the gel phase (293K). The bottom panel of Figure 2.3 shows the radial distribution function of the pazufloxacin drug with water. Since the drug is hydrophobic it has a very weak correlation with water close to 0.40nm. The correlation is stronger in the gel phase as compared to the liquid-crystalline phase. The pazufloxacin drug and water are both sandwiched inside the lipid layer, and although the drug is hydrophobic, it is still forced to stay close to water.

2.3.3 Rotational correlation function

A time correlation function (TCF) $C(t)$ can be computed from MD simulations and is related to an average property of interest for instance $\langle A \rangle$ [90]

$$C(t) = \langle A(0)A(t) \rangle \tag{2.2}$$

If the TCF decays exponentially, correlation time τ can be obtained via a multiexponential fit, where τ gives information about how soon the property A becomes uncorrelated with its starting value. A special kind of TCF is the second order rotational correlation function (RCF) which gives information of time correlation of a molecular vector [90]

$$C_2(t) = \langle P_2(\cos\phi(0))P_2(\cos\phi(t)) \rangle \tag{2.3}$$

where P_2 is the second order Legendre polynomial. At long times this function converges to the order parameter squared S^2. In order to study the rotational dynamics of the drug molecule inside the lipid environment, RCFs were plotted versus time. Figure 2.6 shows the plot of the rotational autocorrelation function of the normal of the

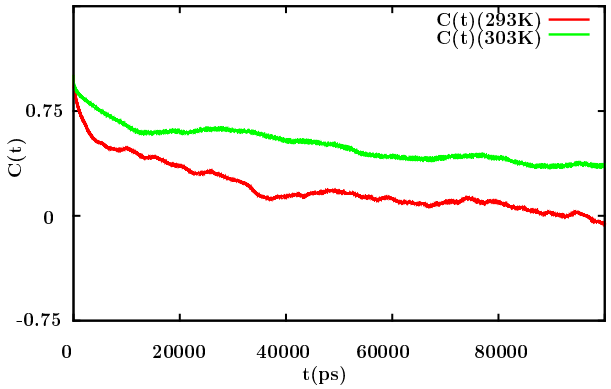

Figure 2.6: Rotational autocorrelation function of the normal of the plane spanned by three atoms on the aromatic ring (one fluorine and two carbons) of the pazufloxacin drug, calculated at temperatures 293 K and 303 K.

plane formed by three atoms (one fluorine atom and two carbon atoms) on the aromatic ring of the pazufloxacin drug molecule inserted in the lipid bilayer. The RCF is calculated at two different temperatures, 293 K and 303 K, when the bicelle is in the gel and the liquid-crystalline phase, respectively. It is calculated by fitting in the function $exp(\frac{-t}{\tau_c})$. The rotational correlation time is also decreased with increasing the temperature. Because the tumbling of the molecule increased with increasing the temperature. The correlation time (τ) in the gel phase was computed to be 71.92 ns, while in the liquid-crystalline phase, it turned out to be 19.26 ns. These values imply that the drug molecule is more restricted in the gel phase of the bicelle, as compared to the liquid-crystalline phase.

2.3.4 Translational self-diffusion

Apart from information about the insertion and final positioning of the drug molecule inside the model membrane, MD simulations can also provide dynamic information about diffusion of the drug molecule. The translational self-diffusion coefficient D of the drug molecule is determined as the ratio of the mean square displacement (msd) to time in the limit of infinite time from the Einstein equation [90]:

$$D = \lim_{t\to\infty} \left\langle \frac{|r(t_0+\tau) - r(t_0)|^2}{2n\tau} \right\rangle \tag{2.4}$$

where $r(t)$ indicates the displacement at time t and the brackets denote an ensemble average; the parameter n denotes the number of translational degrees of freedom (three for an isotropic liquid). In lipid bilayers molecules exhibit lateral two-dimensional molecular diffusion and hence $n = 2$ for such systems. The lateral diffusion coefficient of pazufloxacin diffusing in the lipid bilayer was calculated in the linear regime from 10-175 ns. The log-log plot of the mean square displacement with time is shown in Figure 2.7 and the diffusion coefficient was computed to be $2.9 \pm 0.5 \times 10^{-12}$ m^{2}s^{-1}. In general, molecular diffusion of a molecule inside a lipid bilayer can be anomalous, with the mean square displacement msd being related to the diffusion by the relation [91]:

$$msd = Ct^{\alpha}, \tag{2.5}$$

where C is a constant and α quantifies the diffusion; $\alpha = 1$ indicates normal Brownian diffusion while $\alpha \neq 1$ indicates the diffusion is anomalous [92]. For $\alpha > 1$ the regime is considered super-diffusive, while for $\alpha < 1$ it is considered sub-diffusive. From the negative slope of the plot in Figure 2.7, it can be inferred that the drug molecule exhibits some anomalous diffusive behavior when diffusing through the bicellar environment.

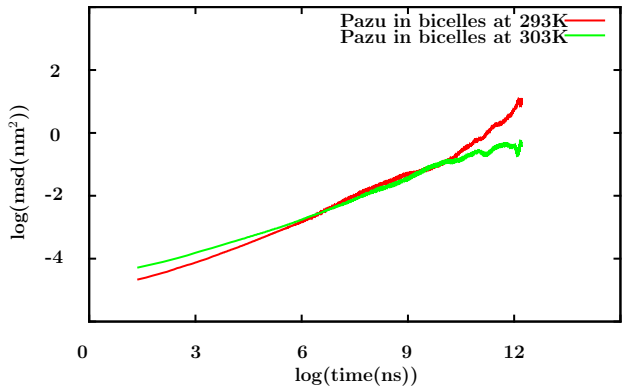

Figure 2.7: Log-log plot of the mean square displacement (nm) versus time (ms) of pazufloxacin molecule in DHPC-DMPC bicelles at two different temperatures: 293 K (bicellar gel phase) and 303 K (bicellar liquid-crystalline phase).

The DHPC/DMPC bicelle exists in a gel phase at 293 K and in a liquid crystalline phase at 303K. The diffusion coefficient of the drug diffusing in the bicelle was hence calculated in these two different bicellar phases and the value of the coefficient α was

computed from the slope of the curve. The value of α turns out to be 0.49 at 293 K (gel phase) and 0.4 at 303 K (liquid crystalline phase), indicating that the diffusion is anomalous and in the sub-diffusive regime.

2.4 Conclusions

Biophysical and biochemical studies of the interaction of drugs with lipid bilayers is of interest for pharmacology since the ability of a drug to reach its intracellular target depends crucially on how it interacts with the cell membrane barrier. MD simulations can provide a wealth of conformational and dynamic information about molecules as well as energetic information about drug and target interactions. Such studies are useful for the pharmaceutical industry in the context of novel drug design and discovery. For drug delivery studies, it is important to check if the simulation results are consistent with a diffusion model wherein the drug is well-inserted into the lipid bilayer, which is required for its diffusion toward the active ligand-binding site of the receptor. Insertion of the drug into the membrane could aid in its adopting a bioactive conformation and ultimately interact effectively with a target receptor.

The work described in this chapter focuses on investigating the molecular interactions and transport behavior of a fluorinated drug molecule pazufloxacin in a bicellar environment composed of a mixture of DHPC/DMPC lipid molecules. Molecular dynamics simulations were used to draw conclusions about the penetration of the drug into the lipid bilayer, conformational preferences inside the lipid bilayer and its diffusive properties inside the bilayer. These computational results are useful in the context of understanding drug delivery processes in biological cell membranes.

2. Molecular dynamics simulation study of the translational self-diffusion and liposomal interaction of a fluorinated drug molecule inserted in a phospholipid bilayer

Chapter 3

NMR study of PEG $LiClO_4$ mixtures in molecular solvents

3.1 Background and Motivation

In recent years, modern civilization has realized that the earth's fossil fuels are insufficient to fulfil the global energy requirement of human beings in the near future [93, 94]. On the other hand, there has been an increasing emission of greenhouse gases which are affecting the global climate change, driving the scientific community to develop clean and renewable energy and energy storage technologies [95]. Considerable research activity has been seen in recent years in the areas of energy storage devices such as lithium ion batteries (LIBs) and electrochemical double layer supercapacitors [95]. A lithium containing salt dissolved either in aqueous or nonaqueous solvents is required as an electrolytic medium for the operation of such devices [93, 96]. Various polymeric solid electrolytes are also used as electrolytic media in such devices. Among them PEO(poly(ethylene oxide)), PEG(poly(ethylene glycol)), and PPO (poly (propylene oxide)) are recognised as promising candidates for polymer electrolytes [96]. However, their use in neat form with Li^+ salt mixtures as an electrolyte has a major disadvantage as it has a very low ionic conductivity range of to 10^{-4} Scm^{-1} at room temperature, which limits their use for various practical application purposes. Polymer ionic conductivity can be increased by increasing the dynamic ability of ethylene oxide (EO) segments. In polyethylene oxide (PEO) based lithium ion batteries, it has been reported that the hydration of PEO molecules increases the conductivity by as much as

1000 times as compared to that of the typical binary mixture of PEO/lithium salts[97]. Such enhancement is attributed to water absorption that increases the mobility of PEO chains, producing more free mobile ions by reducing the coordination between PEO and Li^+ cation. The use of molecular solvents can act as liquid plasticizers which increases the ionic conductivity of these PEO / Li^+ salt mixtures. Therefore, it is of potential interest to study the dynamics of PEO / Li^+ salt mixtures in the presence of various molecular solvents. However, the dynamics of various salt mixtures of PEO-based polymers are very difficult to study because of their crystalline nature and therefore an attempt has been made recently to study the dynamics of low molecular weight EO-based polymer (PEG) in its $LiClO_4$ mixtures[96]. NMR spectroscopy is one of the most promising experimental techniques to study the dynamics of the PEO-based polymers and its mixtures with various salts and molecular solvents[98, 99, 100, 101, 102]. Beside the use of molecular solvents, ionic liquids (ILs) are also used as liquid plasticizers for the dynamic study of PEO / Li^+ salt mixtures. Other studies have also reported the dynamical aspects of EO-based polymers and their mixtures with various components[103, 104, 105, 106, 107], but little is known regarding the dynamics of these EO-based polymers in its lithium salt mixtures with molecular solvents. Understanding the dynamics of the EO-based polymer and Li^+ cation in molecular solvents can aid in the potential development of various energy storage devices.

This chapter reports on a study of the dynamics of low molecular weight PEG-based polymers in $LiClO_4$ mixtures of molecular solvents via NMR spectroscopic methods. $LiClO_4$ has been selected because of its maximum stability for the Li/O_2 battery as compared to other Li^+ salts as studied through X-ray photoelectron spectroscopy. Three deuterated molecular solvents were selected with different solvent properties viz. D_2O, DMSO-D_6, and CD_3CN. Six PEG-based polymers were selected with a varying molecular weight, starting from PEG-400 to PEG-10000. NMR chemical shifts, self-diffusion coefficients, NMR relaxation, and 2D HOESY NMR spectroscopic methods have been used to understand the structure and dynamics of these polymeric mixtures of $LiClO_4$ in its molecular solvents.

3.2 Experimental Section

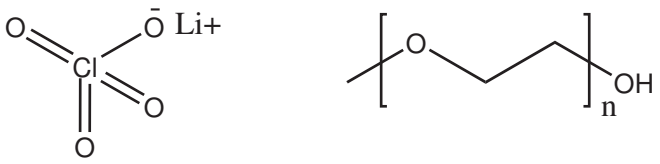

Figure 3.1: Lithium Perchlorate Polyethylene Glycol Molecule

3.2.1 Materials & Methods

The PEG-based polymers were purchased from Sigma Aldrich with 99.99 % purity and used without further purification. $LiClO_4$ was obtained from Fluka analytical (99.99 %) and kept overnight in an oven at a temperature of 65 ^{0}C to remove any absorbed moisture. The ternary mixtures are prepared by adding 53.2mg of $LiClO_4$ (1.0m) in 0.5 ml of D_2O. Then 15 mg of the PEG-based polymer is added to the solution mixture. For solvent mixture ,the mole fraction of solvent $x_{solvent}$(Solvent:DMSO-D_6, CD_3CN) in D_2O is kept constant. The concentration of $LiClO_4$ and polymers are kept constant in all mixtures for the purpose of comparison. All solutions were mixed by using the vortex method and ultra-sonication in order to obtain a clear transparent solution. The solutions were transferred to a 5mm NMR tube (external diameter) to record the NMR data. All NMR experiments were performed at four different temperatures starting at 298K, 310K, 317K, and 325 K. The samples were kept for 30 min inside the spectrometer prior to the NMR experiment in order to achieve thermal equilibrium. The mixture of LiCl in D_2O is used as reference in the Li NMR.

3.2.2 NMR Parameters

A Bruker 600MHz spectrometer equipped with QXI a probe having a 5mm bore was used for the diffusion experiments. Proton from the EO unit of the polymer was probed to measure the self-diffusion coefficients of polymer. The $ledgp2s1d$ pulse sequence was used to measure the signal intensity of the polymer to obtain the self- diffusion coefficient of the polymer via standard Stejskal-Tanner equation[108, 109, 110]. $ledgp2s1d$ pulse sequence minimize the effect of the eddy currents. The diffusion time

Δ in its DMSO-D_6 and D_2O mixture of polymer was kept as 0.2 s whereas in case of CD_3CN mixtures it was 0.05 s. On the other hand, the duration of the applied gradient pulse(δ) for all the diffusion experiments was kept constant at 1500 μs. The diffusion time Δ was optimize of each solvent before doing experiments. For each experiment we used 10 gradient points. The starting point was 1% and the last one was 95 %. The relaxation delay was kept 4 s in each experiment.

The pulse sequences used for the T_1 and T_2 relaxation experiments are $t1ir1d$ (inversion recovery) and $cpmg1d$ (CPMG), respectively[111, 112, 113]. Two dimensional (2D) HOESY experiments were recorded on a Bruker 400 MHz spectrometer equipped with a BBO probe. The pulse program used for the ^{7}Li-^{1}H HOESY experiments was $hoesyph$ and the mixing time for the experiments were 200 ms and 500 ms for DMSO-D_6 and CD_3CN mixtures, respectively[114]. Spectra were acquired in D_2O mixtures, however no cross peak were obtained.

3.3 Results & Discussion

3.3.1 NMR chemical shift

Generally PEG-based polymer shows three peaks in its solutions with molecular solvents; one for the internal ethylene group, second one is for the ethylene group at the end of the polymeric chain which is bonded with the hydroxyl group of the polymer and the third one is for the hydroxyl group[98, 115, 116]. Liu et al. reported the appearance of multiple peaks in the ^{1}H NMR spectra of PEG with a predominant polymeric peak for the internal EO unit of seven (heptamer) and above, however a single resonance appears below it [117]. The position and intensity of these peaks in the NMR ppm scale depends upon the nature of molecular solvent, nature of PEG, and its concentration in the solvent. The intensity of the alcoholic peak is very small and is dominated by the peaks from the EO units of PEG. Therefore, the only dominating resonance is from the EO units the PEG. ^{1}H NMR spectra of PEG-10000 / $LiClO_4$ / D_2O mixture by the addition of DMSO-D_6 and CD_3CN at four temperatures is shown in Figure 3.3. The ^{1}H NMR spectra of the PEG-10000 / $LiClO_4$ / D_2O without the addition of any co-solvent is given in Figure 3.3(a).

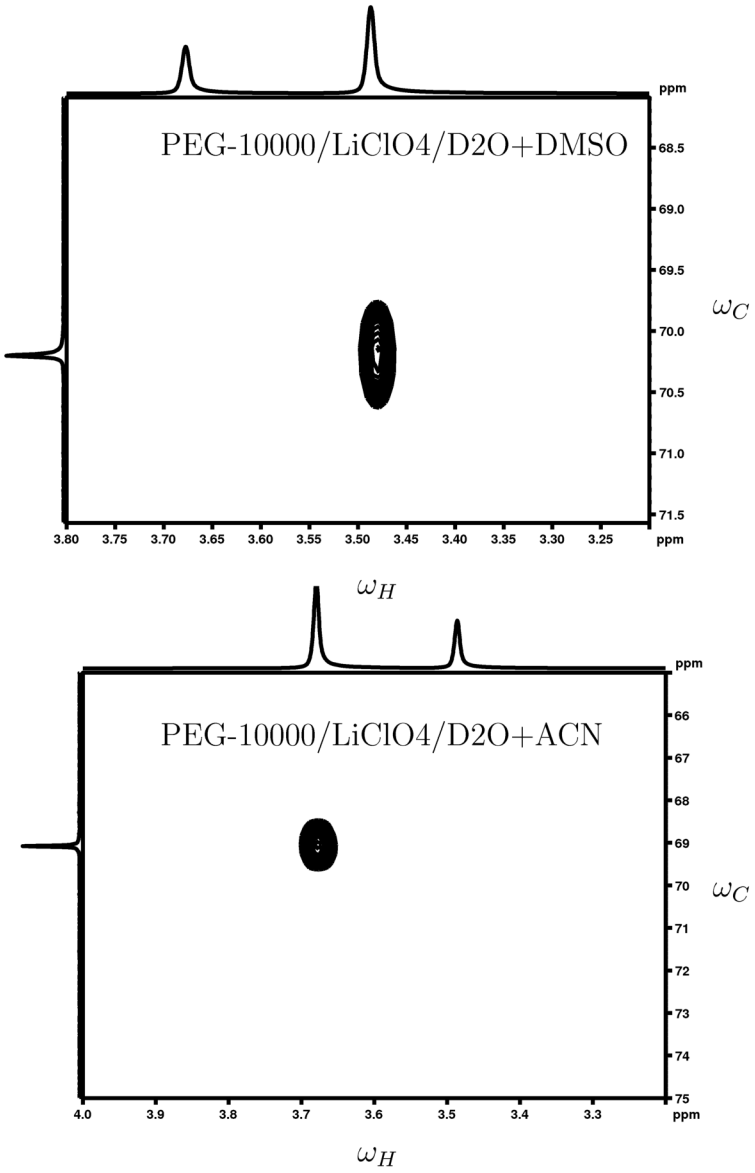

Figure 3.2: The 2D ^{1}H-^{13}C HMBC spectra of PEG-10000 / $LiClO_4$/D_2O+DMSO (top) and PEG-10000 / $LiClO_4$ / D_2O+ACN (bottom) recorded at 298K, Both specta are confirm the polymer resonances.

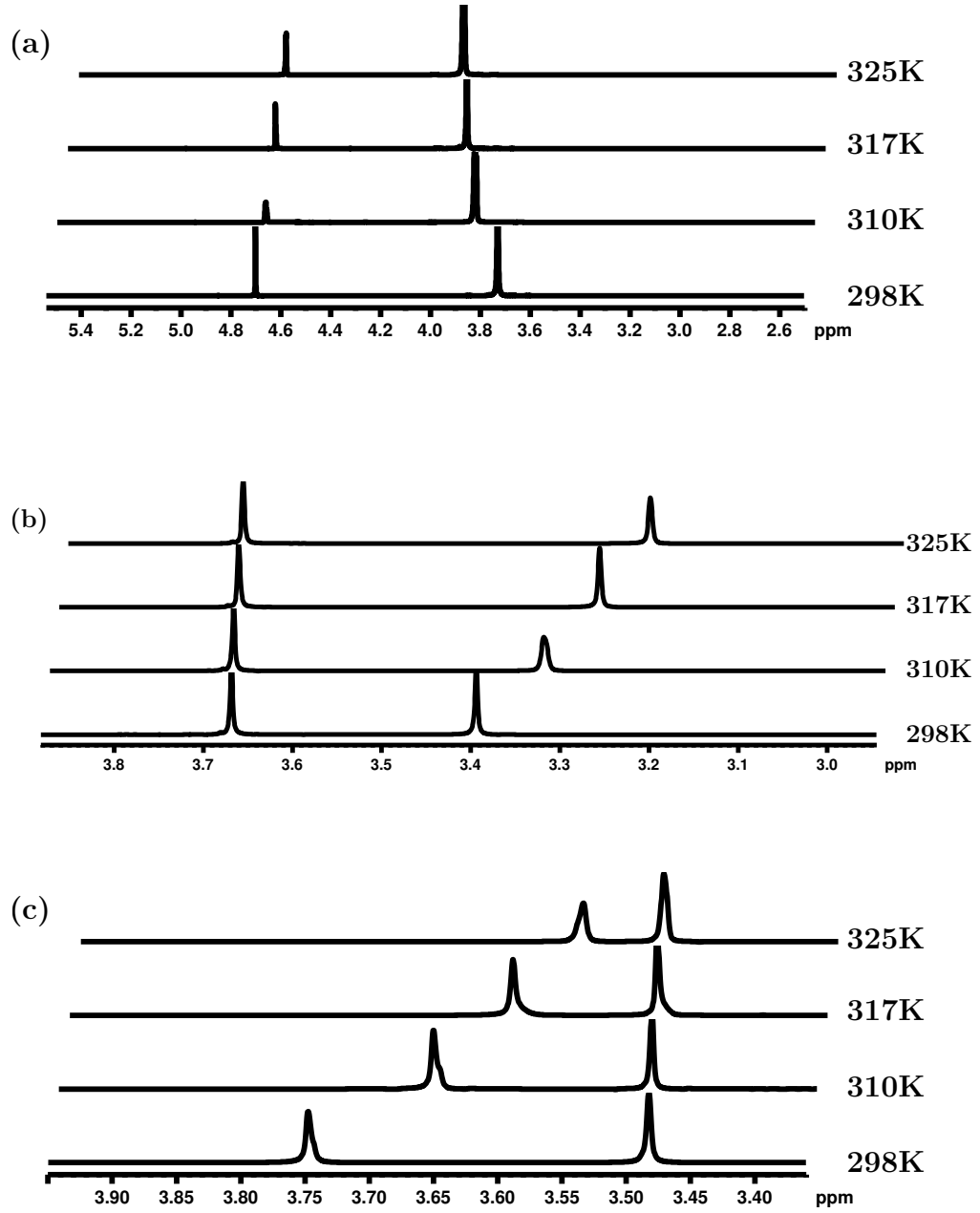

Figure 3.3: Temperature dependent variation of the ^1H NMR chemical shifts of the PEG-10000 in its $LiClO_4$ mixtures of D_2O (a), D_2O+ACN (b), and D_2O+DMSO (c), respectively

Table 3.1: Temperature dependent chemical shift values of the protons of EO unit of PEG in its PEG / $LiClO_4$ / solvent mixtures. Experimental uncertainties in chemical shifts are within ± 0.01 ppm

PEG / D_2O	**298K**	**310K**	**317K**	**325K**
10000	3.729	3.865	3.939	3.996
8000	3.732	3.866	3.939	3.998
3350	3.730	3.863	3.940	4.008
1450	3.728	3.867	3.937	3.998
1305	3.730	3.836	3.939	3.997
400	3.731	3.867	3.938	3.999
PEG / ACN+D_2O	**298K**	**310K**	**317K**	**325K**
10000	3.394	3.328	3.277	3.230
8000	3.404	3.337	3.286	3.238
3350	3.403	3.335	3.285	3.238
1450	3.387	3.318	3.268	3.221
1305	3.405	3.337	3.290	3.241
400	3.395	3.325	3.290	3.233
PEG / DMSO+D_2O	**298K**	**310K**	**317K**	**325K**
10000	3.482	3.489	3.493	3.496
8000	3.482	3.489	3.493	3.496
3350	3.478	3.482	3.485	3.486
1450	3.484	3.490	3.494	3.498
1305	3.479	3.489	3.494	3.497
400	3.480	3.486	3.490	3.493

Figure 3.2 represents the 2D ^{1}H-^{13}C HMBC spectra of the signal emerging from the EO unit of the PEG-10000 polymer. The HMBC spectra indicate that the ^{1}H resonance from PEG molecules is appearing at 3.47 ppm in PEG-10000 / $LiClO_4$ / D_2O/DMSO-D_6 mixture and 3.65 ppm in its PEG-10000 / $LiClO_4$ / D_2O / CD_3CN mixtures. The other peak appearing nearly at 3.7 ppm and 3.45 ppm in its PEG-10000 / $LiClO_4$ / D_2O / DMSO-D_6 and PEG-10000 / $LiClO_4$ / D_2O / CD_3CN mixtures are from the water molecules as observed from the HMBC and confirmed from the HSQC experiments. Temperature dependent chemical shift values of the resonances emerging out from the EO unit of all the studied PEG-based polymers. An increase in the temperature of the

medium increases the chemical shift values of the EO unit of PEG in its D_2O mixtures of $LiClO_4$. However, addition of molecular co- solvent such as DMSO-D_6 and CD_3CN shows a negligible temperature dependency and the changes are within the experimental error of ± 0.01 ppm as observed from Table 3.1. It is well known that the chemical shift of the proton is sensitive to its chemical environment and strongly influenced by the temperature of the medium due to the change in the magnetic susceptibility of the protons[118].

The observed downfield shift in the PEG / $LiClO_4$ / D_2O mixtures are because of the breaking of inter and intramolecular -HCH...OCH_2 hydrogen bonds. The conformational change existing in PEG is due to the reorganization of the red shifted O-H...O and blue shifted C-H...O H-bond is also in support of this statement. Increase in the temperature of the medium break these inter- and intra-molecular hydrogen bond network and consequently increase its interactions with the D_2O molecules through the D_2O...HCH- blue shifted and O-D...OCH_2 red shifted H-bonding interactions[98]. The increased dipole moment of the -CH bond with an increase in the temperature of the medium is also contributes to the downfield shift of the -CH bond because of the solvent disordering as observed from our earlier report of the $LiClO_4$ salt mixtures of ionic liquids in water[111]. An increased solvent disordering around the EO unit of polymers has also been observed which leads to an increase in the dipole moment of the -CH bond of EO units is also in support of this argument[119, 120, 121]. However, addition of molecular solvents (DMSO-D_6 / CD_3CN) to the PEG / $LiClO_4$ / D_2O mixtures shows an insignificant temperature dependency in the chemical shifts of EO protons. It suggests that the EO units of PEG are mostly surrounded by the DMSO-D_6 and CD_3CN molecules; and because of the poor H-bonding ability of these solvent molecules with the EO units of PEG it shows a negligible temperature dependency in its chemical shift values.

3.3.2 NMR Relaxation

Temperature dependent T_1 and T_2 relaxation time of PEG-400 and PEG-10000 in its $LiClO_4$ mixtures of molecular solvents is shown in Figure 3.4. The T_1 and T_2 relaxation times for other polymers are given in Table 3.2 & 3.3. It is observed from Figure 3.4 that the relaxation times of the PEG-based polymer in its $LiClO_4$ mixtures

of molecular solvents increase with an increase in the temperature of the medium. It indicates that the PEG-based polymers experience a less restricted dynamics with an increase thermal energy of the medium[122].

When the reorientational correlation time (τ_c) of the internuclear vector is small compared to the reciprocal of the proton resonance frequency in the extreme narrowing condition then the NMR T_1 relaxation time is given by equation as:

$$\frac{1}{T_1} = \frac{3}{2}(\frac{\mu_0}{4\pi})^2 \frac{\gamma^4 \hbar^2 \tau_c}{r^6} \tag{3.1}$$

where, μ is the permeability of free space, γ is the gyromagnetic ratio of the proton, and r is the interproton distance, respectively[123].

Table 3.2: ^{1}H NMR T_1-Relaxation times of the EO unit of PEG in PEG-plasticizer-$LiClO_4$ mixtures.

T_1 / PEG / D_2O	**298K**	**310K**	**317K**	**325K**
400	0.840 ± 0.007	1.188 ± 0.001	1.368 ± 0.003	1.548 ± 0.005
1305	0.689 ± 0.010	0.990 ± 0.004	1.138 ± 0.004	1.258 ± 0.006
1450	0.694 ± 0.009	0.984 ± 0.003	1.117 ± 0.004	1.237 ± 0.005
3350	0.651 ± 0.01	0.939 ± 0.004	1.036 ± 0.006	1.186 ± 0.005
8000	0.689 ± 0.007	0.908 ± 0.005	1.054 ± 0.005	1.181 ± 0.006
10000	0.668 ± 0.009	0.914 ± 0.005	1.063 ± 0.005	1.179 ± 0.007
T_1 / PEG / DMSO+D_2O	**298K**	**310K**	**317K**	**325K**
400	0.593 ± 0.01	0.762 ± 0.006	0.874 ± 0.005	0.998 ± 0.005
1305	0.685 ± 0.012	0.895 ± 0.004	0.973 ± 0.003	1.057 ± 0.007
1450	0.687 ± 0.009	0.906 ± 0.005	0.959 ± 0.005	1.077 ± 0.005
3350	0.569 ± 0.017	0.695 ± 0.007	0.771 ± 0.005	0.865 ± 0.007
8000	0.681 ± 0.008	0.868 ± 0.005	0.966 ± 0.006	1.077 ± 0.005
10000	0.661 ± 0.011	0.862 ± 0.006	0.938 ± 0.006	1.023 ± 0.006
T_1 / PEG / ACN+D_2O	**298K**	**310K**	**317K**	**325K**
400	1.967 ± 0.003	2.238 ± 0.025	2.366 ± 0.033	2.621 ± 0.050
1305	1.780 ± 0.011	2.160 ± 0.024	2.282 ± 0.028	2.650 ± 0.046
1450	1.828 ± 0.004	2.268 ± 0.014	2.543 ± 0.031	2.748 ± 0.040
3350	1.765 ± 0.005	2.197 ± 0.017	2.466 ± 0.035	2.610 ± 0.045
8000	1.777 ± 0.005	2.178 ± 0.018	2.529 ± 0.014	2.781 ± 0.047
10000	1.836 ± 0.004	2.132 ± 0.019	2.411 ± 0.031	2.645 ± 0.034

3. NMR study of PEG $LiClO_4$ mixtures in molecular solvents

The reorientational correlation time of the EO unit of the polymer has also been estimated by utilizing BPP type relaxation described in Equation 3.1 by ignoring all other relaxation mechanisms and is represented in Figure 3.4c for the $LiClO_4$ mixtures of PEG-400 and PEG-10000 in their respective solvent mixtures. Other values of τ_c are given in Table 3.4.

Table 3.3: ^{1}H NMR T_2-relaxation times of the EO unit of PEG in PEG-plasticizer-$LiClO_4$ mixtures.

T_2 / PEG / D_2O	**298K**	**310K**	**317K**	**325K**
400	0.790 ± 0.005	0.907 ± 0.052	1.214 ± 0.020	1.313 ± 0.030
1305	0.660 ± 0.006	0.899 ± 0.001	1.052 ± 0.010	1.194 ± 0.011
1450	0.649 ± 0.005	0.881 ± 0.003	1.050 ± 0.007	1.173 ± 0.006
3350	0.627 ± 0.007	0.849 ± 0.001	1.024 ± 0.001	1.148 ± 0.005
8000	0.610 ± 0.003	0.826 ± 0.001	1.008 ± 0.003	1.151 ± 0.001
10000	0.626 ± 0.006	0.838 ± 0.001	1.022 ± 0.004	1.165 ± 0.001
T_2 / PEG / DMSO+D_2O	**298K**	**310K**	**317K**	**325K**
400	0.558 ± 0.001	0.612 ± 0.003	0.702 ± 0.007	0.856 ± 0.014
1305	0.621 ± 0.002	0.701 ± 0.005	0.835 ± 0.004	1.007 ± 0.011
1450	0.662 ± 0.001	0.720 ± 0.002	0.892 ± 0.006	1.003 ± 0.005
3350	0.480 ± 0.001	0.547 ± 0.001	0.664 ± 0.004	0.776 ± 0.010
8000	0.600 ± 0.002	0.768 ± 0.007	0.904 ± 0.004	0.910 ± 0.006
10000	0.598 ± 0.002	0.680 ± 0.001	0.826 ± 0.013	0.701 ± 0.007
T_2 / PEG / ACN+D_2O	**298K**	**310K**	**317K**	**325K**
400	0.396 ± 0.002	0.351 ± 0.001	0.310 ± 0.001	0.295 ± 0.001
1305	1.373 ± 0.009	1.572 ± 0.007	1.664 ± 0.012	1.882 ± 0.015
1450	0.966 ± 0.002	1.061 ± 0.006	1.356 ± 0.005	1.382 ± 0.013
3350	1.200 ± 0.010	2.197 ± 0.018	2.467 ± 0.035	2.611 ± 0.046
8000	1.094 ± 0.004	1.268 ± 0.004	1.678 ± 0.015	1.843 ± 0.018
10000	0.315 ± 0.001	0.315 ± 0.001	0.323 ± 0.002	0.348 ± 0.001

It has been observed from Figure 3.4c that the correlation time of the EO unit of the PEG-based polymers decreases with the increase in the temperature of the medium, suggesting a free motion of the polymer.

Table 3.4: The estimated reorientational correlation time (τ_c) of the PEG-based polymer in its PEG / $LiClO_4$ /solvent mixtures

PEG / D_2O	$\tau_c(ps)/298K$	$\tau_c(ps)/310K$	$\tau_c(ps)/317K$	$\tau_c(ps)/325K$
400	47.9	33.9	29.5	26.0
1305	58.5	40.7	35.4	32.0
1450	58.1	40.9	36.1	32.6
3350	61.9	42.9	38.9	33.9
8000	58.5	44.4	38.2	34.1
10000	60.3	44.1	37.9	34.2
PEG / DMSO+D_2O	$\tau_c(ps)/298K$	$\tau_c(ps)/310K$	$\tau_c(ps)/317K$	$\tau_c(ps)/325K$
400	67.9	52.9	46.1	40.4
1305	58.8	45.0	41.4	38.1
1450	58.7	44.5	42.0	37.4
3350	70.8	57.9	52.3	46.6
8000	59.2	46.4	41.7	37.4
10000	60.9	46.8	42.9	39.4
PEG / ACN+D_2O	$\tau_c(ps)/298K$	$\tau_c(ps)/310K$	$\tau_c(ps)/317K$	$\tau_c(ps)/325K$
400	20.5	18.0	17.0	15.4
1305	22.6	18.7	17.7	15.2
1450	22.0	17.8	15.8	14.7
3350	22.8	18.3	16.3	15.4
8000	22.7	18.5	15.9	14.5
10000	22.0	18.9	16.7	15.2

The estimated correlation time given in Figure 3.4c and Table 3.4 indicates that the τ_c values of the EO unit of the PEG-based polymers follows the order as τ_c (PEG / $LiClO_4$ / D_2O/DMSO-D6) > τ_c (PEG / $LiClO_4$ / D_2O) > τ_c (PEG / $LiClO_4$ / D_2O / CD_3CN) which suggests that the decrease in the viscosity of the medium makes the environment of polymers less hindered for the rotation. The viscosity η of x_{DMSO-D_6} = 0.5 in D_2O(3.3cP)>D_2O (0.89 cP) >x_{CD_3CN} = 0.5 in D_2O (0.57cP) mixtures is in support of the above statement.

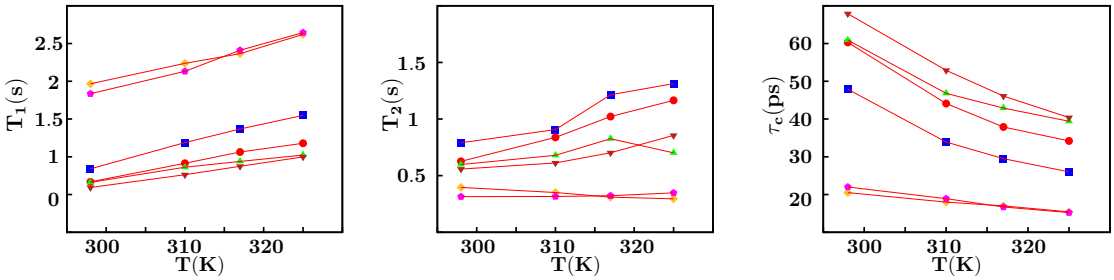

Figure 3.4: Temperature dependent variation of T_1 (a), T_2 (b), and τ_c (c) of EO unit of PEG- based polymers in its PEG/$LiClO_4$ /solvent mixtures. The symbol ■ 10000 / $LiClO_4$ / D_2O, The symbol ■ represents the D_2O-$LiClO_4$-PEG-400, ● represents the D_2O-$LiClO_4$-PEG-10000, ▼ represents the DMSO+D_2O-$LiClO_4$-PEG-400, ▲ DMSO+D_2O-$LiClO_4$-PEG-10000, ♦ ACN+D_2O-$LiClO_4$-PEG-400, *pentagonblack* represents ACN-$LiClO_4$-PEG-10000

3.3.3 NMR Diffusion

Temperature dependent self-diffusion coefficients of the PEG-based polymer were measured through the PFG-NMR methods and the values are given in the Table 3.5. It has been observed that the self-diffusion coefficients of PEG-based polymer in its $LiClO_4$ mixtures of molecular solvents follows the order as D_{PEG} (PEG/$LiClO_4$/D_2O /CD_3CN)> D_{PEG}(PEG / $LiClO_4$ / D_2O)> D_{PEG}(PE G/ $LiClO_4$ / D_2O / DMSO-D_6) and shows good correlation with the bulk viscosity of these molecular solvent mixtures indicating a strong diffusion-viscosity coupling. The hydrodynamic radii (R_H) of the diffusing polymer have been estimated by applying the Stokes-Einstein equation considering the sticky boundary condition as represented in Table 3.6. The R_H of the PEG-based polymers in its $LiClO_4$ mixtures of molecular solvents follows the order as of R_H (PEG / $LiClO_4$ / D_2O / DMSO-D_6)>R_H (PEG / $LiClO_4$ / D_2O) >R_H(PEG/$LiClO_4$ / D_2O / CD_3CN) and are inconsistent with the opposite trend of the experimentally measured self-diffusion coefficient values. However, the temperature dependent hydrodynamic results indicate that the R_H values of polymers decrease with the increase in the temperature of the medium. This can be explained on the basis of the solvation/desolvation phenomenon[119, 120, 124]. A change in the solvation behavior around the EO unit of the polymer with the increase temperature of the medium as reported by Magazu et al[121]. and Shikata et al[119]. independently for the aqueous solutions of PEO-based

polymer is the reason for the decrease in R_H values of polymers. Magazu et al[121]. observed a change in the solvation number of 2.4 per EO unit at 10 °C to 2.0 at 80 °C as studied from their ultrasonic velocity measurement. The temperature dependent R_H studies obtained from the NMR self-diffusion measurement shows a dramatic decrease of the hydrodynamic radii of PEO chains in its D_2O mixtures. Shikata et al[119]. observed a solvation number of 4.0 at a temperature lower than 30 °C obtained from their dielectric relaxation measurements are about twice as large as that obtained through the ultrasonic velocity measurement studies by Magazu et al[121].

Table 3.5: ^{1}H NMR Diffusion coefficients($10^{-10}\mathrm{m}^2\mathrm{s}^{-1}$)of the EO unit of PEG in PEG-plasticizer-$LiClO_4$ mixtures.

D / PEG / D_2O	**298K**	**310K**	**317K**	**325K**
400	3.82 ± 0.04	15.28 ± 0.50	18.91 ± 0.20	402.87 ± 57.5
1305	2.25 ± 0.02	6.20 ± 1.50	10.15 ± 0.14	390.09 ± 87.2
1450	1.86 ± 0.01	3.26 ± 0.06	12.44 ± 0.56	373.59 ± 55.82
3350	1.10 ± 0.01	2.46 ± 0.10	9.17 ± 0.24	237.39 ± 29.7
8000	0.69 ± 0.01	2.99 ± 0.09	7.94 ± 0.34	185.39 ± 18.41
10000	0.69 ± 0.01	2.37 ± 0.10	14.37 ± 1.15	190.28 ± 24.15
D / PEG / DMSO+D_2O	**298K**	**310K**	**317K**	**325K**
400	0.81 ± 0.01	1.96 ± 0.05	5.32 ± 0.14	23.59 ± 1.77
1305	0.27 ± 0.01	2.80 ± 0.02	3.69 ± 0.38	50.39 ± 7.57
1450	0.52 ± 0.01	5.54 ± 0.40	4.72 ± 0.14	41.22 ± 5.53
3350	0.27 ± 0.01	0.43 ± 0.01	5.49 ± 0.27	11.94 ± 2.87
8000	0.14 ± 0.01	0.82 ± 0.01	0.76 ± 0.02	29.62 ± 4.65
10000	0.15 ± 0.01	0.62 ± 0.01	0.67 ± 0.03	14.09 ± 1.63
D / PEG / ACN+D_2O	**298K**	**310K**	**317K**	**325K**
400	19.39 ± 0.08	28.46 ± 0.41	38.19 ± 0.55	85.37 ± 3.25
1305	20.08 ± 0.28	27.18 ± 0.19	35.39 ± 0.47	83.03 ± 1.14
1450	19.29 ± 0.14	31.54 ± 0.84	45.77 ± 0.38	126.04 ± 4.59
3350	18.97 ± 0.07	31.54 ± 0.84	34.33 ± 0.29	87.86 ± 2.92
8000	20.19 ± 0.08	31.59 ± 2.48	45.99 ± 4.02	66.13 ± 4.31
10000	18.96 ± 0.18	35.06 ± 0.46	48.47 ± 2.39	67.62 ± 1.15

However, this study also reported the desolvation behavior around the EO unit of PEO with increased temperature of the medium. Considering these reports, it can be

inferred that the decreased hydrodynamic radii of the PEG-based polymers with the increased temperature of the medium in its $LiClO_4$ mixtures of molecular solvents is due to the desolvation behavior around the EO unit. The hydrodynamic radius of the polymer was calculated by using stokes-einstine relation

$$D = \frac{k_b T}{6\pi\eta R_H} \tag{3.2}$$

where D is diffusion coefficient, η is viscosity. It is widely reported that the increase in the molecular weight of the polymer increases the magnitude of its R_H. This behavior has only been observed at lower temperatures of 298K and 310K in this study, however it disappear with increasing temperature of the medium.

Table 3.6: Hydrodynamic radii (R_H / nm) of the PEG-based polymer in its PEG / $LiClO_4$ / solvent mixtures.

PEG / D_2O	**R_H(Å)/298**	**R_H(Å)/310**	**R_H(Å)/317**	**R_H(Å)/325**
400	6.4	2.1	2.1	0.1
1305	11.0	5.3	3.9	0.1
1450	13.0	10.0	3.2	0.1
3350	22.0	13.0	4.3	0.2
8000	36.0	11.0	4.9	0.2
10000	36.0	14.0	2.7	0.2
PEG/DMSO+D_2O	**R_H(Å)/298**	**R_H(Å)/310**	**R_H(Å)/317**	**R_H(Å)/325**
400	14.0	7.2	3.1	0.8
1305	41.0	5.1	4.5	0.4
1450	21.0	2.6	3.5	0.5
3350	41.0	33.0	3.0	1.6
8000	78.0	17.0	22.0	0.6
10000	73.0	23.0	25.0	1.4
PEG/ACN+D_2O	**R_H(Å)/298**	**R_H(Å)/310**	**R_H(Å)/317**	**R_H(Å)/325**
400	3.2	2.6	2.1	1.0
1305	3.1	2.7	2.3	1.0
1450	3.3	2.4	1.7	0.7
3350	3.3	2.8	2.3	1.0
8000	3.1	2.4	1.7	1.0
10000	3.3	2.1	1.7	1.0

Interestingly this behavior is only observed in its $LiClO_4$ mixtures of D_2O and D_2O/DMSO-D6, however shows insignificant effect in its mixtures with CD_3CN possibly because of high self-diffusion coefficients of PEG in CD_3CN as compared to other mixtures.

3.3.4 Activation Energy

An attempt has been made to estimate the activation energy of the spin-lattice relaxation time and the diffusion processes from their experimentally measured values by applying the Arrhenius activation theory and are presented in Table 3.7 and 3.8.

Table 3.7: Activation energy of spin-lattice relaxation (E_{a,T_1}) of the EO unit of PEG-based polymer in its PEG/$LiClO_4$/solvent mixtures. All the units are in kJmol^{-1}.

Polymer/MW	$\mathbf{E_{a,T_1}}$ **kJ mol**$^{-1}$ (ACN+D_2O)	$\mathbf{E_{a,T_1}}$ **kJ mol**$^{-1}$ (D_2O)	$\mathbf{E_{a,T_1}}$ **kJ mol**$^{-1}$ (DMSO+D_2O)
400	8.4 ± 0.5	18.4 ± 1.6	15.6 ± 0.3
1305	11.5 ± 1.0	18.2 ± 2.1	12.9 ± 1.6
1450	12.4 ± 0.9	17.4 ± 2.0	13.2 ± 1.6
3350	12.0 ± 1.3	17.8 ± 2.0	12.5 ± 0.1
8000	13.7 ± 0.8	16.3 ± 0.9	13.6 ± 0.8
10000	11.1 ± 0.6	16.7 ± 1.8	13.1 ± 1.5

It has been observed that the activation energy of the T_1 relaxation process for the PEG-based polymer follows the order E_{a,T_1} (PEG / $LiClO_4$ / D_2O / DMSO-D_6) > E_{a,T_1} (PEG / $LiClO_4$ / D_2O)> E_{a,T_1} (PEG / $LiClO_4$ / D_2O / CD_3CN). However, insignificant variation in the E_{a,T_1} has been observed with the change in the molecular weight of polymer.

The activation energy for the T_1 relaxation process for the PEG-based polymers are in the range of 8-19 kJ/mol which are in support of other literature reports[115, 117]. At this stage the trend followed by the E_{a,T_1} in its different molecular solvents is not known and detailed theoretical studies are required for further confirmation. However, the activation energy of the diffusion process follows the order as $E_{a,D}$ (PEG / $LiClO_4$ / D_2O / DMSO-D_6) > $E_{a,D}$ (PEG/ $LiClO_4$ / D_2O) > $E_{a,D}$ (PEG / $LiClO_4$ / D_2O / CD_3CN)

Table 3.8: Activation energy of Diffusion ($E_{a,D}$) of the EO unit of PEG-based polymer in its PEG/$LiClO_4$/solvent mixtures. All the units are in kJmol^{-1}.

Polymer/MW	$E_{a,D}$ kJ mol^{-1} (ACN+D_2O)	$E_{a,D}$ kJ mol^{-1} (D_2O)	$E_{a,D}$ kJ mol^{-1} (DMSO+D_2O)
400	24.5 ± 4.1	25.5 ± 2.1	30.4 ± 1.3
1305	24.6 ± 4.1	26.9 ± 2.5	30.7 ± 2.2
1450	24.1 ± 6.3	27.3 ± 2.6	29.8 ± 1.8
3350	24.5 ± 4.4	28.3 ± 2.6	32.6 ± 1.9
8000	24.4 ± 2.2	28.7 ± 2.6	33.3 ± 2.4
10000	24.4 ± 2.5	28.5 ± 2.7	33.9 ± 1.9

and strongly correlates with the viscosity of these molecular solvents suggesting a strong diffusion-viscosity coupling.

3.3.5 2D HOESY Experiment

^{1}H-^{7}Li two dimensional HOESY experiments have been carried out in order to understand the Li^+ dynamics inside the Li^+ salt mixtures of the polymeric system. The mixture of LiCl in D_2O is used as reference in the Li NMR. Figure 3.5 represents the ^{1}H-^{7}Li HOESY spectra for the PEG-10000 / $LiClO_4$ / D_2O / DMSO-D_6 and PEG-10000 / $LiClO_4$ / D_2O / CD_3CN mixtures. These experiments were also carried out or these two mixtures in protonated solvent (DMSO and ACN) however, no ^{1}H-^{7}Li 2D cross peaks are observed, suggesting that the Li^+ cation is not interacting with either of these solvent molecules. It has been observed from the ^{1}H-^{7}Li HOESY spectra that the Li^+ cation is binding with the water molecules (signal is emerging from the amount of H_2O present in the sample and not from the D_2O) and not with the EO unit of PEG-based polymers (see Figure 3.5 for water and PEG resonances). A strong 2D HOESY correlation has been observed for the corresponding water resonance as given in Figure 3.5. The ^{1}H-^{7}Li distance has also been estimated from the assumption of isolated spin pair approximation given by Borgias et al.[125].

$$r_{H-Li} = r_{ref}\left(\sqrt[6]{\frac{I_{ref}}{I_{H-Li}}}\right) \tag{3.3}$$

where r_{H-Li} and r ref are the effective H-Li internuclear distance in the unknown and reference system; and I_{H-Li} and I_{ref} are their respective 2D HOESY intensities, respectively[125]. The reference ^{1}H-^{7}Li internuclear distance and its corresponding intensity values are taken as 2.0 Å and 8.3×10^{6} , respectively.

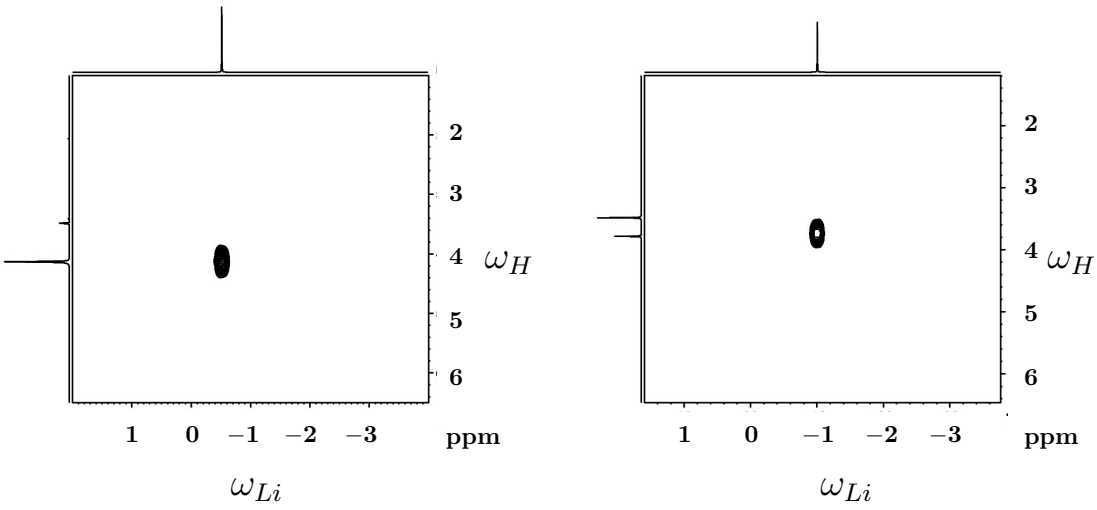

Figure 3.5: 2D HOESY spectra of PEG400 and PEG10000 in DMSO+D_2O solvent.

The estimated ^{1}H-^{7}Li internuclear distances are given in the Table 3.9. Experiments were also carried out in the PEG / $LiClO_4$ / D_2O mixtures; however ^{1}H-^{7}Li no cross peaks were observed for these systems suggesting that the ^{1}H-^{7}Li distance is far apart to be detected within the NMR timescale. The possible reason for the absence of ^{1}H-^{7}Li HOESY correlation is because of the faster proton transfer in its PEG / $LiClO_4$ / D_2O mixtures which could not be detected on the NMR time scales of the experiment.

Table 3.9: Calculated ^{7}Li-^{1}H distance from the HOESY spectra obtained through the two dimensional HOESY experiments in its PEG / $LiClO_4$ / solvent mixtures at 298 K.

Polymer/MW	$\mathbf{r}_{\mathrm{H-Li}}$(Å) (DMSO+$D_2O$)	$\mathbf{r}_{\mathrm{H-Li}}$(Å) (ACN+$D_2O$)
400	2.054	3.875
1305	3.040	2.851
1450	3.105	3.204
3350	2.178	3.885
8000	3.071	3.492
10000	2.843	3.528

Addition of molecular solvents hindered the proton transfer between water molecules in its PEG / $LiClO_4$ / D_2O / DMSO-D_6 and PEG / $LiClO_4$ / D_2O / CD_3CN mixtures and therefore the ^{1}H-^{7}Li HOESY correlations are observed in these mixtures. However, sophisticated computational studies are required to prove this hypothesis. The ^{1}H-^{7}Li distance in its PEG / $LiClO_4$ / D_2O / DMSO-D_6 mixtures are observed to be less (close to the van der Waals diameter of water, 2.8 Å) as compared to its mixtures with PEG / $LiClO_4$ / D_2O / CD_3CN mixtures as shown from their calculated values in Table 3.9. This indicates that the Li^+ cation binds strongly in its mixtures with DMSO-D_6 as compared to its mixtures with CD_3CN. In summary it can be said that the Li^+ cation is free to move in its PEG / $LiClO_4$ / D_2O mixtures however, addition of molecular solvents like DMSO-D_6 or CD_3CN hinders its mobility.

3.4 Conclusion

The study described in this chapter shows some of the important aspects of structural and dynamical features of PEG / $LiClO_4$ / solvent mixtures through different NMR spectroscopic methods. Temperature dependent variation of chemical shifts shows the poor coordinating ability of solvent mixtures with the PEG molecules as compared to the D_2O molecules. Increased temperature of the medium decreases the R_H value of the PEG-based polymer because of the desolvation behavior around the polymer. Both the self-diffusion coefficients and rotational correlation time of PEG-based polymers shows strong coupling with the viscosity of medium. Appearance of Li^+ -water bind-

ing in its PEG/$LiClO_4$/D_2O/DMSO-D_6 and PEG / $LiClO_4$ / D_2O / CD_3CN mixtures, and its disappearance in its PEG / $LiClO_4$ / D_2O mixture suggest that the mobility of Li^+ cation is more in the later mixture as compared to the former mixtures and therefore can act as a better electrolytic media for their wider applications.

3. NMR study of PEG $LiClO_4$ mixtures in molecular solvents

Chapter 4

Molecular dynamics simulation study of molecular interactions and transport properties of an ionic liquid-polymer mixture

4.1 Background and Motivation

Ionic liquids (IL) are a class of molten salts with melting points below 100°C that typically consist of a large organic cation and a smaller anion and have unique physical and chemical properties such as low volatility, high conductivity, low flammability and good thermal and chemical stability [126, 127, 128]. ILs are now widely accepted as "designer solvents" that can be tailored to suit a particular application [129]. ILs have been considered for a wide range of applications as catalytic,or as a co-catalyst, or as catalyst activator agents or just as the solvent for the reaction. They have been investigated as highly efficient catalysts for transition metals [130, 131, 132]. Due to the solubilities of gases such as CO_2, SO_2 or CO, ILs are used as the absorption media for gases [133, 134, 135]. ILs are highly conducting, and prevent the anode from hydrolysis - they are hence used as electrolytes in batteries [136, 137]. ILs have better ability to form tribofilms, higher thermal stability, environmental friendliness, and adaptability to various applications as compared to the conventional lubricants. They have remarkable ability to reduce friction and are hence widely used as lubri-

cants [138, 139]. Another recent application is based on their capability to dissolve lignocellulose biomass to a much higher extent than standard polluting organic solvents used in industry [140].

It is well established that polymeric materials can provide mechanical stability to binary mixtures of polymers with ionic liquids [141, 142, 143]. There is hence a widespread interest in characterizing the interactions of polymers with ionic liquids, for possible applications in a diverse areas ranging from green chemistry, fuel cells and as substitutes for biodegradable materials [144, 145]. However, it has also been recognized that the mechanism of formation of polymer/IL complexes is far more complex than that observed in salt/IL systems and depends crucially on the molecular interactions between the IL and the polymer [146]. The polymer poly(ethylene oxide) (PEO) and its interactions with prototypical ILs have been extensively studied and it has been shown that in dilute solutions and at room temperature PEO adopts extended conformations in the IL [147]. Ternary mixtures of lithium ions, PEO and IL have been studied using molecular dynamics [148]. Poly(ethylene glycol) (PEG) is another widely used polymer due to its low toxicity and PEG/IL binary mixtures using imidazolium-based ILs have been the subject of several experimental and theoretical investigations [149]. Several studies have revealed that IL/PEG complexes have formed due to the high hydrogen bonding of the terminal chains of the PEG and the IL [150]. In green chemistry the potential of IL/PEG-based aqueous biphasic systems for extraction of biomolecules has been explored [151].

In this chapter, molecular dynamics simulations have been performed to study the solvation structures, and the conformational and dynamic properties of PEG molecules in a prototypical ionic liquid 1-methylimidazolium chloride ([MIM][Cl]). The IL-polymer molecular interactions are investigated as a function of temperature as well as a function of the molecular weight (with the degree of polymerization N ranging from 9-25). The distribution of conformations obtained from the simulations seem to indicate that the PEG molecules adopt either an extended or a helical conformation in the ionic liquid. The atom-atom pair correlation and space distribution functions have been computed via the MD simulations between different cations and anions and PEG O atoms.

4.2 Computational Methods

All MD simulations were performed using the GROMACS 4.5.6 software package [83, 152], using the GROMOS 53a6 force field [84]. The structure and topology of the lipid molecules were downloaded from the Automated Topology Builder website [85]. All the simulations were performed at four different temperatures, namely, 290 K, 300 K, 310 K and 320 K using a canonical NVT (constant particle numbers, volume and temperature) ensemble. The MD rectangular unit cell contained 98 IL molecules and 2 PEG molecules. The composite IL-PEG system was constrained in a starting configuration of a $5 \times 5 \times 5$ nm^3 box and periodic boundary conditions were imposed in three dimensions. The system was prepared by randomly placing the molecules in the simulation box. The temperature was controlled using a modified Berendsen thermostat [87]. The long-range electrostatic Coulomb interactions were controlled using the particle-mesh Ewald (PME) summation method using a fourth order cutoff for the direct space sum [88, 153]. For the short-range van der Waals interaction, the Verlet cutoff scheme was used to restrict the potential to a range of 1 nm [154, 155]. Velocities were assigned from the Maxwell distribution. The equation of motion was integrated with the leap-frog integrator with a 2 fs integration time step. All bond lengths were constrained at their equilibrium distance using the LINCS constraint algorithm of order four [52]. The system was first subjected to a 1 ns MD simulation for energy minimization. These minimized coordinates were fed into the final MD simulation which ran for 100 ns. To investigate dynamics of the binary mixture with varying chain length of the polymer, four different chain lengths of the PEG molecules were used with $N = 2, 5, 6, 12$ and 512 IL cations and 512 Cl anions. These simulations were performed at a fixed temperature of 300 K with a single chain. Convergence of all the simulations have been checked before the final simulation.

4.3 Results & Discussion

To probe the conformational dynamics of PEG molecules in the ionic liquid, various properties of the binary polymer-ionic liquid mixture were investigated via molecular dynamics simulations and are described in detail below.

4.3.1 Distribution of dihedral angles

The distribution of dihedral angles was computed to study the conformational equilibration of the polymer molecules in the ionic liquid. Figure 4.1 shows the distribution of two different average dihedral angles namely the C-C-O-C and the O-C-C-O dihedral angles. The probability distribution of the O-C-C-O dihedral angle is periodic, with two symmetric prominent peaks at $-180°$ and $180°$ and two symmetric smaller peaks at $-75°$ and $75°$. This indicates that this dihedral angle can exist in both the *gauche* and *trans* conformations, with the *trans* conformation being more probable [156].

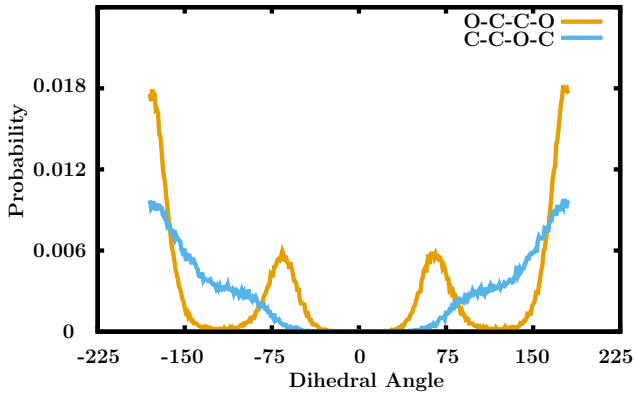

Figure 4.1: Probability distribution of two average dihedral angles (O-C-C-O and C-C-O-C) obtained from the simulation of of PEG molecules in the ionic liquid.

The probability distribution of the C-C-O-C dihedral angle is also periodic and gives a single peak at $180°$, indicating it exists only in the *trans* conformation. A closer look at the snapshots of the simulations (Figure 4.3) shows that the PEG chains in the IL can exist in both extended as well as hairpin conformations.

4.3.2 Radius of gyration

The scaling of size of an isolated polymer chain i.e. a chain in a dilute solution is usually computed with respect to the degree of polymerization N and depends on the scaling of chain size with the concentration in the semidilute region and if R_0 is the size of an isolated chain, the scaling in semidilute solutions follows the ideal chain scaling hypothesis $R_g \sim \sqrt{N}$ [157]. The radius of gyration R_g is related to the structure of the

polymer chain by

$$R_g = \sqrt{\left\langle \frac{1}{N} \sum_i (r_i - r_{CM})^2 \right\rangle} \tag{4.1}$$

where r_i is the position of the ith site on the PEG chain and r_{CM} is the position of the centre-of-mass of the chain. The variation of R_g with temperature is shown in Table 4.2 and it is observed that mean R_g increases with increasing temperature. The chain length of the PEG molecule was kept fixed at 3.7 nm for this simulation. The results of the simulations for the radius of gyration R_g as a function of the polymer chain length at 300 K are shown in Table 4.1.

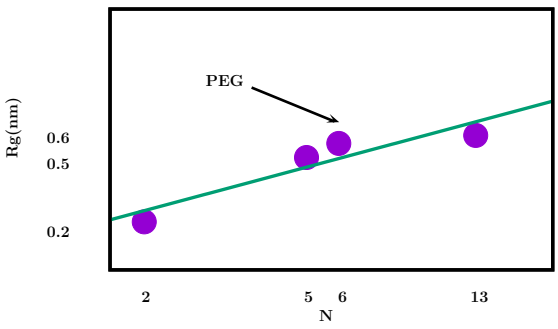

Figure 4.2: Plot of variation of the mean of the radius of gyration R_g with the degree of polymerization N on the logarithmic scale. Fitting gives a scaling exponent of 0.54 ± 0.08.

Figure 4.2 shows the logarithmic plot of the simulation results for variation of radius of gyration R_g with N. The fitting of the line gives a scaling exponent ν, where $R_g \sim N^{\nu}$ of $\nu = 0.54 \pm 0.08$.

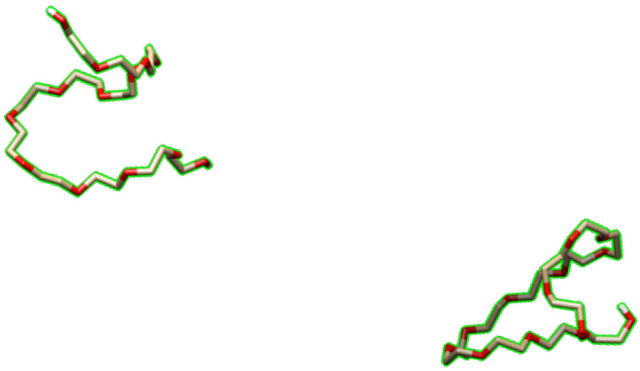

Figure 4.3: Representative snapshots of extended (left) and hairpin conformations (right) of the PEG molecules after a 100 ns MD run at 320 K.

In all the simulations, the value of R_g turns out to be less than that for the extended PEG chain, implying the existence of a non-extended structure conformation.

4.3.3 Radial distribution functions

The radial distribution function is a measure of how the density varies as a function of distance from a reference molecule [89]:

$$g(r) = 4\pi r^3 \rho(r) dr \tag{4.2}$$

where ρ is the number density and r is the distance from the reference molecule.

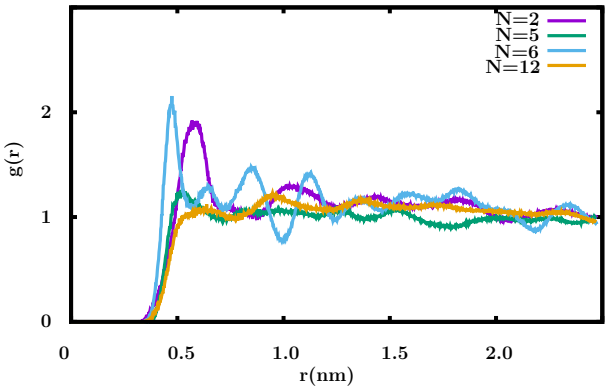

Figure 4.4: Comparison of radial distribution function of the Cl anion of the IL with O atom of the PEG molecule, with varying chain length (N=2,5,6,12). For all PEG chains, the selected O atom is close to the center of the chain.

The radial distribution functions for the centre of mass of each molecule considered in this work were computed from the trajectories of the simulation. These radial distribution or pair correlation functions give an intuitive structural insight into which part of the IL is correlated with atoms on the PEG polymer chain.

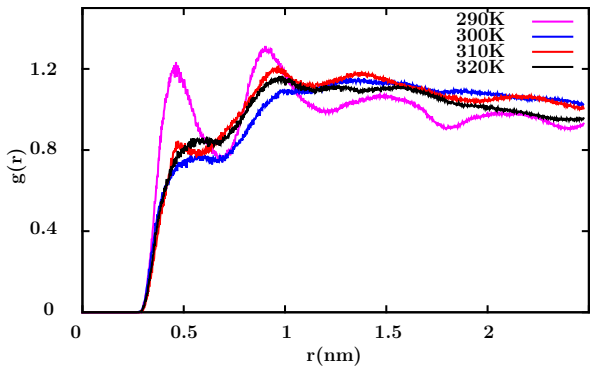

Figure 4.5: Comparison of radial distribution function of the N2 atom of the IL with O atom of the PEG molecule, with varying chain length (N=2,5,6,12). For all PEG chains, the selected O atom is close to the center of the chain.

The peak heights in these radial distribution function plots are dependent on the correlation or local density between the sites considered. The radial distribution functions between O atoms of the PEG molecule and different regions of the IL, namely the Cl- anion and the heavy atom N2 on the cation ring were calculated, in order to study the structural aspects of PEG in IL. Figure 4.4 shows the radial distribution functions between the oxygen atom of the PEG chain and the Cl- anion of the IL, as a function of varying chain length ($N = 2, 5, 6, 12$). The chain lengths $N = 2$ and $N = 6$ show the strongest correlations ($g(r) \approx 2$), while $N = 5$ and $N = 12$ show the weakest correlations. Figure 4.5 shows the radial distribution functions between the oxygen atom of the PEG chain and the N2 atom of the imidazolium ring on the IL, as a function of varying chain length ($N = 2, 5, 6, 12$). The largest peak is close to 0.5 nm. The chain lengths $N = 2$ and $N = 6$ show the strongest correlations, while $N = 12$ shows the weakest correlation. The correlations are not very strong, as evidenced from the value of $g(r)$ not being much greater than 1, with $g(r) \approx 1.5$ for the peak with the highest intensity. There do not appear to be long-range correlations between the polymer chain and the IL cation.

4.3.4 Translational self-diffusion

The transport behaviour of the PEG molecules in the IL was studied by via trajectories which were obtained from the simulation. The lateral diffusion coefficient of the PEG molecules in the linear regime was obtained from the mean square displacement by using Einstein's equation![90]:

$$D = \frac{\langle [R_i(t) - R_i(0)]^2 \rangle}{6t} \tag{4.3}$$

where $R_i(t)$ is the position vector of species i at time t, $R_i(0)$ is the position vector at time zero, D is diffusion coefficient and the brackets refers to the ensemble average.

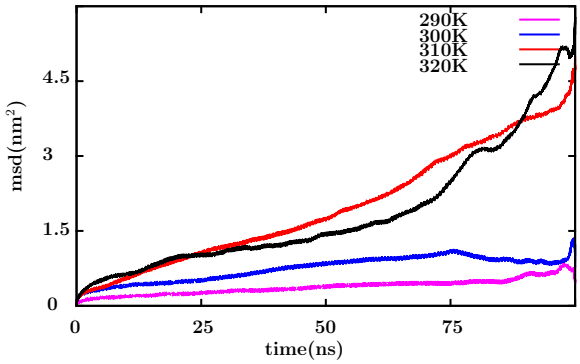

Figure 4.6: Plot of mean square displacement (nm^2) versus time (ns) of the PEG molecule in IL at four different temperatures. The diffusion coefficient D is extracted from the linear regime of the slope.

Anomalous diffusion can be characterized using the relationship between mean square displacement (MSD) versus time from [92]:

$$\text{MSD} = Ct^a \tag{4.4}$$

where a is the parameter which characterizes the degree of anomaly. When $a = 1$, the diffusion is normal (i.e Brownian) and when $a < 1$, the diffusion is anomalous.

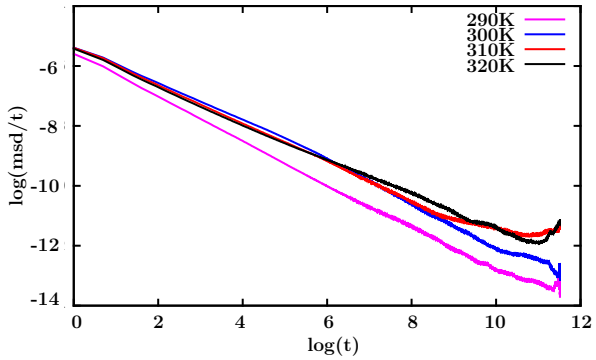

Figure 4.7: Plot between mean square displacement (nm^2) and time (ps) of the PEG molecule in IL on the logarithmic scale at different temperatures. The negative slope of the plots shows the anomalous diffusive behavior of the PEG molecule in the IL.

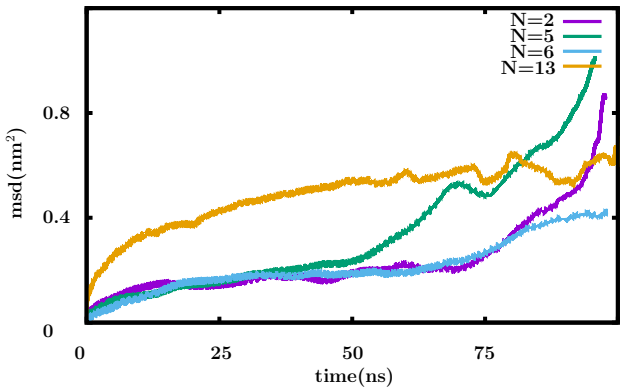

Figure 4.8: Plot of the mean square displacement (nm^2) and time (ns) of the PEG molecule as a function of different degrees of polymerization. The diffusion coefficient D is extracted from the linear regime of the plot.

Figure 4.6 shows the plot of mean square displacement (nm^2) versus time (ns). The diffusion coefficient D is extracted from the slope of the linear part of the plot. From Table 4.2, it can be seen that the diffusion coefficient increases with increasing temperature. Figure 4.7 shows the plot of mean square displacement and time on the logarithmic scale.

Table 4.1: Variation of the mean radius of gyration R_g and diffusion coefficient D of PEG molecules of different lengths in the ionic liquid at 300K.

N	M_w	R_g (nm)	Box Density (g/L)	Diffusion Coefficient (m^2 s^{-1})
2	106	0.234761	641.43	6.10×10^{-12}
5	238	0.491545	643.025	3.90×10^{-12}
6	282	0.57866	643.557	2.43×10^{-12}
12	590	0.629935	646.746	1.01×10^{-12}

Table 4.2: Variation of the mean radius of gyration R_g and the diffusion coefficient D of the PEG molecule in the the ionic liquid with temperature. The chain length of the PEG molecule is kept fixed at 3.7 nm.

Temperature	R_g (nm)	D (m^2 s^{-1})
290 K	1.07	1.10×10^{-12}
300 K	1.18	2.70×10^{-12}
310 K	1.23	1.02×10^{-11}
320 K	1.50	1.06×10^{-11}

The slope on the logarithmic scale is negative, from which it is clear that the PEG molecules diffuse anomalously in the IL. The diffusion coefficient of the PEG molecule, calculated by simulation at 310K (Table 4.1) is $1.02 \times 10^{-11} m^2 s^{-1}$, which corroborates well with the experimentally reported diffusion coefficient for low molecular weight PEG molecules in imidazolium based ILs determined via pulsed field gradient NMR [158]. Diffusion was also calculated as a function of the chain length of the PEG molecule and Figure 4.6 shows the variation of the mean square displacement (nm^2) versus time (ns). The diffusion coefficients are extracted from the linear regime and the value of the diffusion coefficient increases with decreasing degree of polymerization (Table 4.1).

4.4 Conclusions

In this chapter, molecular dynamics simulations were performed to study the molecular interactions, conformational dynamics and transport behaviour of binary mixtures of PEG polymer molecules with a standard ionic liquid. The simulation results imply that the mutual solubilities of the polymer and IL depend mainly on the hydrogen bonding networks between the IL anion and the -OH group of the polymer. At higher temperatures, the PEG molecules tend to exhibit nearly ideal-chain polymer dynamics. At lower temperatures, the PEG molecules in the IL have a finite probability to exist in helical conformations. Simulations of the transport behaviour and computations of the translational self-diffusion coefficient suggest that the PEG molecules show anomalous diffusion behaviour in the IL More detailed studies of long-chain PEG molecules at higher temperatures and in different ionic liquid solvents are required in order to understand the interesting conformational and transport behavior exhibited by polymer/IL binary mixtures. Furthermore, detailed insights into the underlying molecular interactions of such binary mixtures is essential to develop new applications of such mixtures in industry.

4. Molecular dynamics simulation study of molecular interactions and transport properties of an ionic liquid-polymer mixture

Chapter 5

Probing the dynamics and the conformational flexibility of the curcumin inside the DPPC lipid bilayer-a molecular dynamics study

5.1 Background and Motivation

Curcumin is a polyphenolic compound present in the dietary spice turmeric, acquired lot of attention of biologists and chemists due to its wide range of biological applications. It is a good antioxidant and protects the biological systems from oxidative deterioration[159, 160]. It is a potent anti-inflammatory agent because of its ability to scavenge reactive oxygen radicals which cause inflammation[161]. Many scientific studies show that curcumin binds to the amyloid peptide and inhibits the amyloid β aggregation[162, 163]. It can cross the blood-brain barrier and significantly decrease the amyloid β aggregation and is helpful ameliorate Alzheimer's disease[164, 165]. Various studies of curcumin are also shown that it can sensitize tumors to different chemotherapeutic agents including doxorubicin, 5-fluoruracil, pactilaxel, and vincristine[166]. Curcumin can sensitize wide band-gap semiconductors to visible radiation and hence it is also used as the dye in dye-sensitize solar cells[167, 168].

Various studies discuss the antioxidant, anti-inflammatory, antibacterial, antiapop-

tosis, and anticancer related activities of curcumin. Gonsalves et al[169] reported the study of curcumin in cosmetics. They studied curcumin and in vitro skin permeation and reported on the penetration of curcumin in the skin. Barclay et al[170] reported the antioxidation mechanism of curcumin. They suggested that the oxidative action of the curcumin is by donating the H atoms from the phenolic group. Duan et al[171] reported an in vitro/in vivo study of curcumin as an anti-cancer agent. In their experimental study, they synthesized cationic poly(butyl)acrylate nanoparticles coated with curcumin nanoparticles. The in vitro study showed good efficacy against the human hepatocellular cancer cell lines. The in vivo study of curcumin nanoparticles suppressed hepatocellular carcinoma growth. Aggarwal et al[172] reported a review of curcumin as an anti-inflammatory agent against various diseases such as neurodegenerative, cardiovascular, pulmonary, metabolic, autoimmune and neoplastic diseases. Curcumin regulates the various cause of inflammation like cytokines, protein kinases, adhesion molecules, redox status and enzymes. This property of curcumin makes it important for pharmacological applications. Hamaguchi et al[173] reported a review of curcumin in the context of Alzheimer's disease.

Curcumin is a polyphenolic compound which exhibits the keto-enol tautomerism[174, 175]. In acidic and in neutral solutions, the keto form predominantly exists, while in alkaline medium, the stable enol form exists[176]. Our cell walls are made up of lipid membranes and in the human body, curcumin interacts with the cell walls. Dipalmitoylphosphatidylcholine (DPPC) is a typical lipid molecule having hydrophilic head and hydrophobic tail. During the process of hydration, the hydrophilic head aligns toward the water molecules, while the hydrophobic tail aligns away from the water. Due to this, the molecules of the lipid (DPPC) form either a membrane or a bilayer.

In the molecular dynamics study described in this chapter, the dynamical aspects and the conformational flexibility of curcumin is probed inside the DPPC lipid membrane[177, 178]. The DPPC membrane exists in gel phase below the 306K, while it exists as fluid phase above 315K[179]. The molecular dynamics simulations were carried out at 300K and 320K and the diffusion dynamics of both keto and enol forms of curcumin was studied inside the DPPC lipid membrane in the gel and liquid phases. The diffusion model of the curcumin inside the DPPC is probed. To investigate the conformational flexibility of curcumin, radius of gyration and distance between oxygen atoms of the hydroxyl group was calculated and the order parameter and the area per

lipid of the DPPC were also compared.

5.2 Simulation Parameters

In molecular dynamics simulations, for the trajectories, the Newton equation of motion is iteratively solved for small time steps. The initial conditions are provided by the structure file. The molecular dynamics simulation were carried out with GROMACS 4.5.6.[83, 180] package. The Gromos 53a6force field[84, 181] which was developed by Berendsen et al[152] and MD integrator were used. The structure and topology files of the curcumin molecule were taken from Automated Topology Builder[85]. The force field parameters of the lipid bilayer used in the simulations, were developed by Berger et. al.[182]. In each simulation, one molecule of curcumin was placed at the center of the DPPC bilayer, which is made up of 128 molecules of DPPC and 3655 molecules of water.

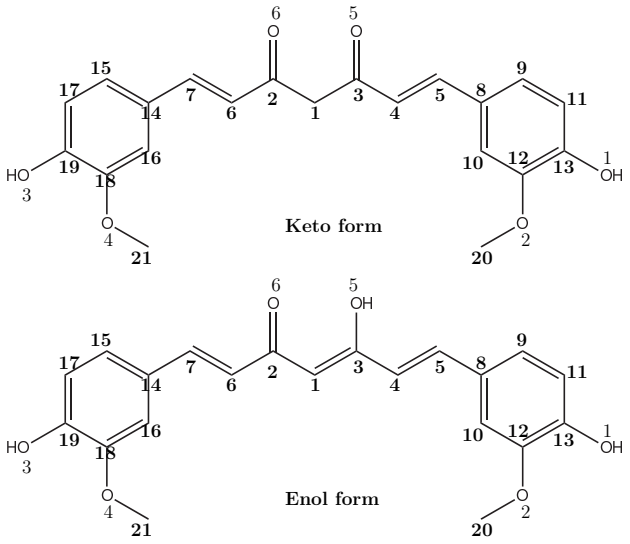

Figure 5.1: The molecular structure of the keto and enol tautomers of curcumin. The bold numbers are assigned to the carbons while non-bold numbers are assigned to oxygen atoms.

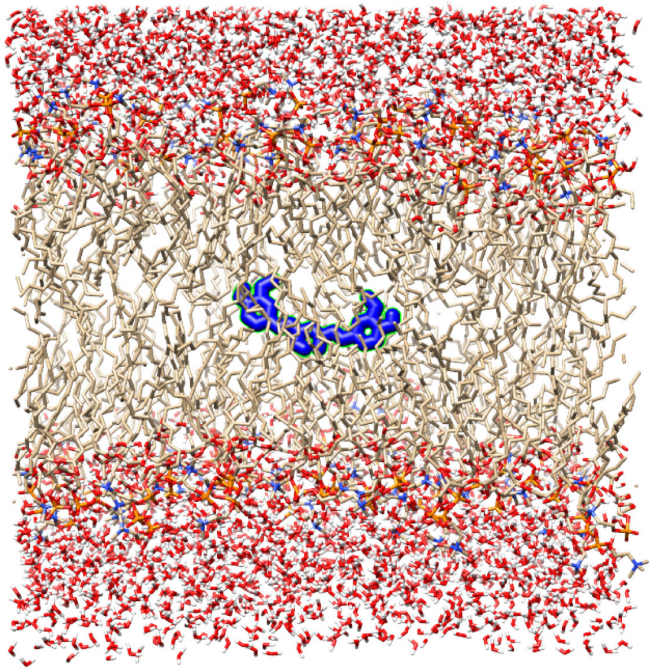

Figure 5.2: Screenshot of curcumin molecule inside the DPPC lipid bilayer.

All simulations were performed at two different temperatures 300K and at 320K, and at 1 bar pressure. Initially all the systems were minimized, then equilibrated for $10ns$ with NVT ensemble at their respective temperatures. The final simulations were performed with the NPT ensemble at 300K and 320K. The value of cut-off for short range electrostatic and Van der Waal's potential was $1.2nm$[183, 184] and the particle Mesh Ewald summation of order four was used[88, 153] for the long range Coulomb force. The periodic boundary condition in three dimensions were used. For temperature coupling Nose-Hoover thermostat[185] and for pressure coupling Parrinello-Rahman barostat[186] was used. For all simulations the constraint algorithm LINCS[52] of order four was used. This constraint algorithm was used for holonomic constraints. The velocities are assigned from the Maxwell distribution. Each simulation was first run for 1 ns to obtain the final coordinates, which were used in the final run of the simulation. All simulations were run for 50 ns with a step size of 2 fs[180]. Berger lipid parameters

5.2.1 Calculating the free energy of solvation

Molecular dynamics simulations were used to calculate the free energy of the solvation of curcumin molecule in the DPPC lipid membrane. The free energy is calculated by using the thermodynamic integration method.

$$\Delta G_{sol} = \int_0^1 d\lambda \langle \frac{dH(\lambda)}{d\lambda} \rangle \tag{5.1}$$

where H is the Hamiltonian and $\lambda = 1$ is a coupled state. First the system was minimized with 500000 steps then equilibrated with NVT ensemble with 20000 steps. Convergence of the simulation was checked before the final simulation. Then the simulation of the free energy of solvation was begun.

5.3 Results & Discussion

5.3.1 Diffusion analysis

The diffusion of a single molecule of curcumin inside the DPPC lipid bilayer was studied. The diffusion coefficients are presented in the table 5.1. The high value of the error in the diffusion coefficients of the curcumin is due to the local fluctuations. In case of large number of molecules, the local effects are averaged out, which reduces the error.

$$\langle \Delta r^2 \rangle = 6Dt \tag{5.2}$$

where $\langle \Delta r^2 \rangle$ is mean square displacement MSD and D is diffusion coefficient.

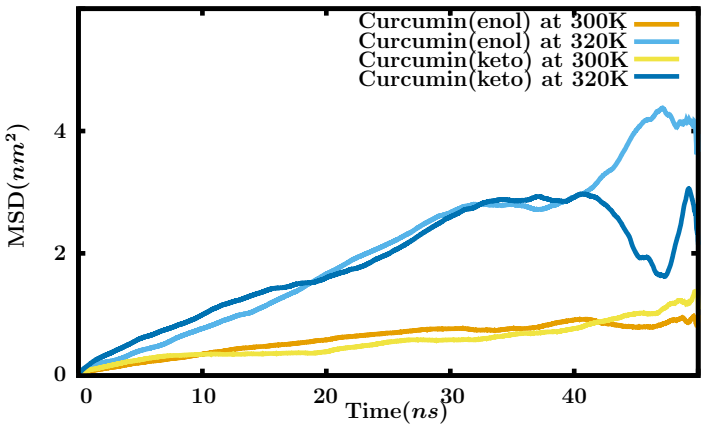

Figure 5.3: Plot of mean square displacement of curcumin with time.

Table 5.1: Diffusion of the curcumin molecule with temperature

Temperature	Curcumin Type	Diffusion coefficient(m^2s^{-1})
300K	Enol	$2.70 \pm 2.60 \times 10^{-12}$
320K	Enol	$1.32 \pm 0.53 \times 10^{-11}$
300K	Keto	$2.70 \pm 1.90 \times 10^{-12}$
320K	Keto	$1.03 \pm 0.68 \times 10^{-11}$

The plot of the mean square displacement(MSD) and time is given in the plot 5.3.

$$MSD = Ct^a \tag{5.3}$$

where MSD is mean square displacement and t is time. The diffusion model is inferred from the log-log plot of the mean square displacement and the time. Figure 5.4 shows the variation of the mean square displacement with time on a logarithmic scale.

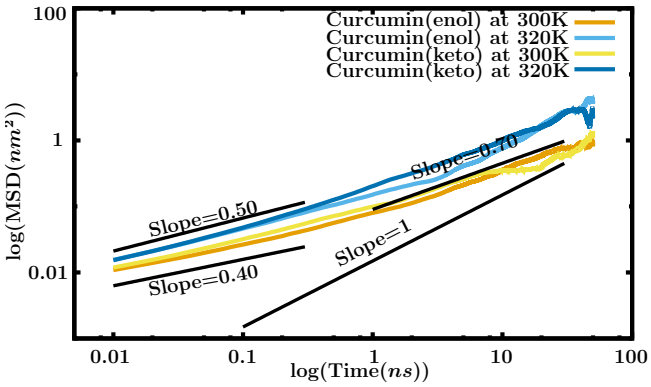

Figure 5.4: Log-log plot of mean square displacement with time. The slope gives information of the nature of the diffusion.

The slope of the plot gives the order of the anomaly and indicates that diffusion happens in the sub-diffusive region. Up to 1 ns, the slope of the plot lies between the 0.4-0.5. But after 1 ns, it lies close to 0.7.

5.3.2 Radius of gyration

Curcumin can exist in different conformations due to conformational flexibility. To probe the conformational flexibility of the curcumin, the radius of gyration was studied. The radius of gyration of a molecule is given as:

$$Rg = (\frac{\sum_i ||r_i||m_i}{\sum_i m_i})^{\frac{1}{2}}. \tag{5.4}$$

where Rg is radius of gyration, r_i is the position coordinates and m_i is the mass of the i_{th} atom. The radius of gyration of curcumin was studied as a function of time, and at both temperatures. The mean radius of gyration of the curcumin is presented in the Table 5.2. The radius of gyration as a function of time is presented in Figure 5.5.

Table 5.2: Variation of the mean radius of gyration of the curcumin molecule in the DPPC lipid bilayer with temperature.

Temperature	Type	Radius of Gyration(nm)
300K	Enol form	0.53
320K	Enol form	0.57
300K	Keto form	0.53
320K	Keto form	0.47

The value of the radius of gyration of both the conformation at 300K is same, while at 320K, the value of keto form is less than the enol form. This shows that the keto form of the curcumin is more flexible than the enol form. The enol form is less flexible due to the carbon-carbon double bond(C1=C3) in curcumin(See Figure5.1).

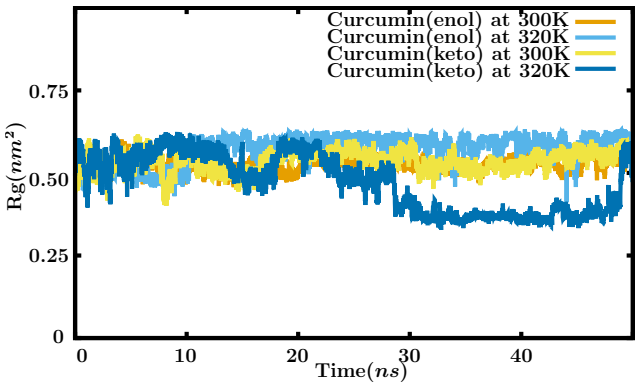

Figure 5.5: Variation of the radius of gyration of the curcumin molecule with time. Keto form has a lower radius of gyration at 320K.

In Figure 5.5 at 320K, the keto form has a radius of gyration less than 0.3 nm. This also shows the flexibility of the keto form.

5.3.3 Density profile

To investigate the location of the curcumin molecule inside the DPPC lipid membrane, the density of the curcumin molecule is calculated. The density profile of curcumin is given in the Figure 5.6. It is clear that, during the whole simulation, the curcumin shows maximum density at the center of the DPPC lipid bilayer. It is due to the hydrophobic nature of the curcumin.

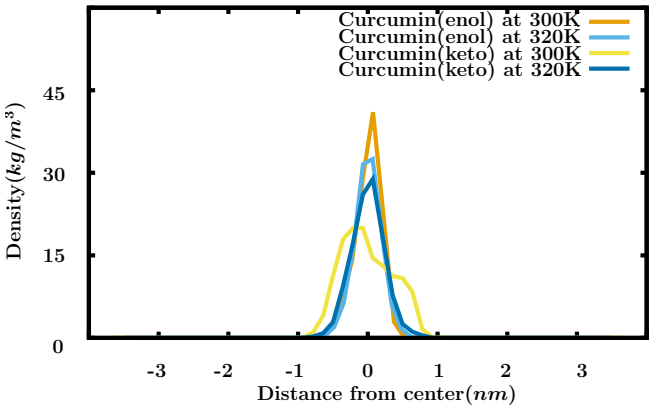

Figure 5.6: Plot of the density profile of curcumin. Since curcumin is hydrophobic it remains inside the lipid bilayer. The maximum density is found at the center.

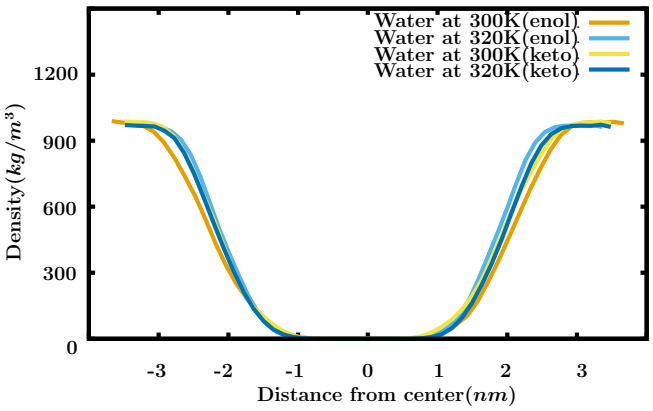

Figure 5.7: Plot of the density profile of the water molecules of the DPPC lipid bilayer. The water molecules remain outside the lipid bilayer during the entire run of the simulation, showing that the bilayer remains stable.

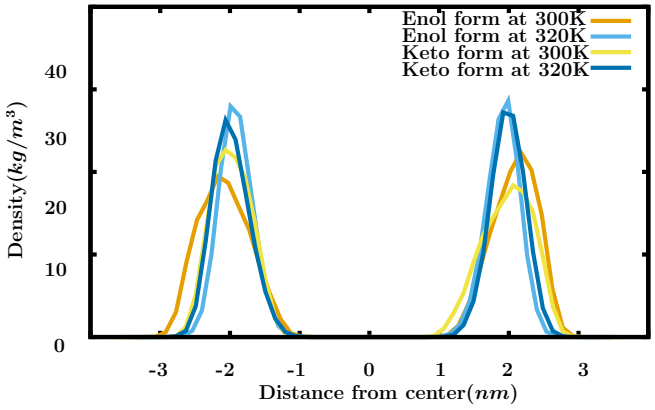

Figure 5.8: Plot of the density profile of the phosphorus atoms of the DPPC lipid bilayer, showing the stability of the bilayer during the entire run of the simulation.

Figure 5.7 shows that during the entire run of the simulation, the water molecules stay outside the bilayer. This suggests that the curcumin molecule does not cross the bilayer. Furthermore, curcumin stays inside the lipid bilayer. Figure 5.8 shows the density profile of phosphorus atoms of the lipid bilayer. The probability of the phosphorus atoms localized at same place in whole simulation. This shows the stability of the bilayer during the entire simulation.

5.3.4 Distance between the oxygens of the hydroxyl group

To probe the shape of the curcumin inside the DPPC lipid bilayer, the distance between oxygens of the hydroxyl group was calculated. The distance between the oxygens of the hydroxyl group of the curcumin while stretched is $1.8nm$. It is calculated by using Avogadro software[187]. The average distance between both oxygens of the keto form is 1.12 nm. This shows that at 320K, the keto form exists in the hairpin like configuration. Due to the single bond in C-C(C1-C3) atoms, the keto form becomes more flexible than the enol form of the curcumin.

Table 5.3: Average distance between oxygen atoms of hydroxyl group of curcumin.

Temperature	curcumin(Enol)(nm)	curcumin(Keto)(nm)
300K	1.48	1.49
320K	1.55	1.12

The average calculated distance between both the oxygens is presented in Table 5.3. The double C=C(C1=C3) bond in the enol form of curcumin makes it more rigid than the keto form of the curcumin. Figure 5.9 shows that the keto form of curcumin distance is approximately 0.5 nm. This suggests that it exists in a hairpin-like configuration.

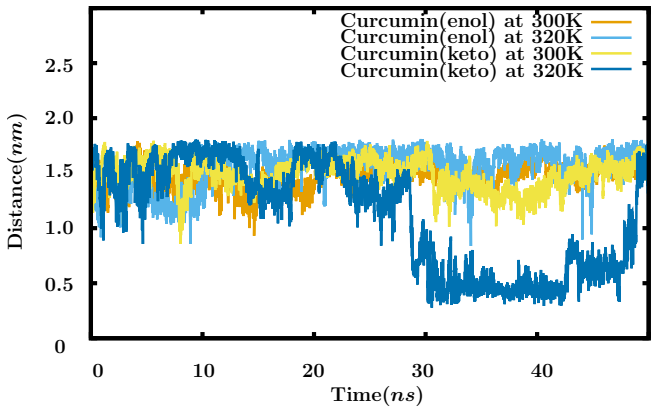

Figure 5.9: Variation of the distance between the oxygen atoms of the hydroxyl group of curcumin.

When the temperature increases, the distance in the enol form does not vary much, while in case of keto form it decreases at 320K and is sometimes less than 0.4 nm(See Figure 5.9). This is due to the flexibility of the keto form. It suggests that at 320K, the keto form exists in a hairpin-like configuration. This also supports the results obtained from the radius of gyration calculations.

5.3.5 Free energy of solvation

Curcumin is a hydrophobic molecule. To investigate its solubility in the lipid environment, the free energy of the solvation was calculated. The free energy of the solvation of the curcumin inside the lipid bilayer is presented in the Table 5.4. The negative value of the free energy of the solvation shows its high solubility in the lipid environment.

Table 5.4: Free energy(kJ/mol) of solvation of the curcumin in the lipid bilayer.

Temperature	curcumin(Enol)	curcumin(Keto)
300K	-246.25 ± 15.03	-134.64 ± 19.35
320K	-157.12 ± 22.49	-205.62 ± 35.78

5.3.6 Lipid parameters

5.3.6.1 Area per lipid

Area per lipid is an important property of the lipid membranes. The area per lipid of the DPPC bilayer was calculated and is presented in Table 5.5. With increasing temperature, the area per lipid also increases, which is in good agreement with already reported results in the literature[188]. However it was observed that a single molecule of the curcumin does not have any significant effect on the area of the lipid.

Table 5.5: Area per lipid(nm^2) of DPPC membrane alone and the DPPC membrane with curcumin is calculated.

Temperature	Pure membrane(nm^2)	With curcumin(Enol)(nm^2)	With curcumin(Keto)(nm^2)
300K	0.56	0.54	0.58
320K	0.61	0.61	0.58

5.3.6.2 Order parameter

The concept of the order parameter is widely used in the area of lipid bilayers. It is a sensitive measure of structural orientation or flexibility of lipids in a bilayer. The deuterium order parameter S_{CD} for the carbon tails was calculated. The angle θ_{CD} is the angle between the molecular axis given by the carbon atoms C_{i-1} and C_{i+1} and the lipid bilayer normal. The average is taken over the entire simulation time and for all lipid molecules.

$$S_{CD} = \frac{1}{2}(3\langle cos^2\theta_{CD}\rangle - 1) \tag{5.5}$$

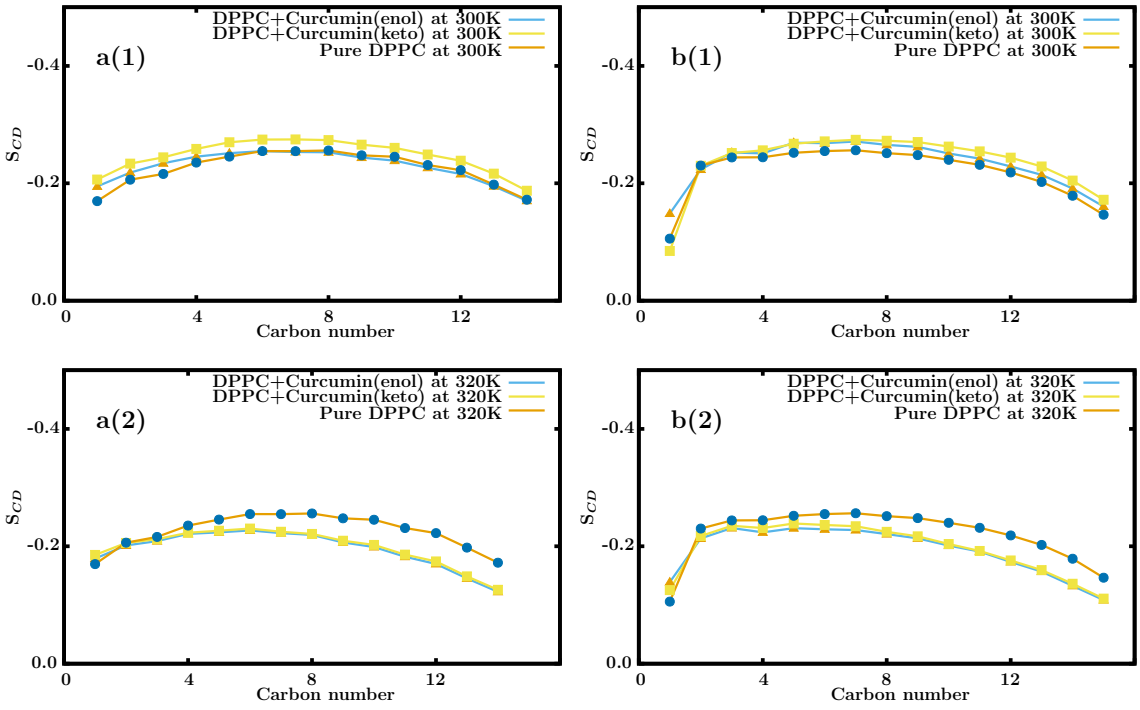

Figure 5.10: The order parameter plots of the two tails(a&b) of the DPPC lipid at 300K and 320K.

The order parameters of DPPC lipid bilayer calculated by this simulation study shows a close agreement with experimental results at 50°C[189].

5.4 Conclusions

In this chapter, the dynamics and the conformational flexibility of the curcumin molecule inside a DPPC lipid bilayer was probed using molecular dynamics simulations. The whole diffusion dynamics exists in the sub-diffusive regime. The C=C double bond in the enol form makes it rigid, while the keto form is more flexible. The flexibility of the keto form increases with an increase in the temperature. At 320K, curcumin also exists in the hairpin-like configuration. The area per lipid and the order parameters shows good agreement with already existing values in the literature.

Chapter 6

Summary and future outlook

This thesis focuses on the study of translational diffusion dynamics of small molecules investigated via NMR spectroscopy and molecular dynamics simulations. The thesis begins with the molecular dynamics study of the antibiotic drug pazufloxacin diffusing in a lipid membrane. The lipid membrane is composed from two different type of phospholipid molecules, namely DPPC and DMPC molecules. The nature of the diffusion, radial distribution function and rotational correlation functions of the drug molecule were calculated and presented. The rotational correlation function suggests that the drug is more restricted in the gel phase of the lipid bilayer. The study of translational self-diffusion of pazufloxacin molecule inside the membrane mimetic leads to interesting insights about the nature of diffusion inside the lipid membrane.

Another direction followed in the thesis is the structural and dynamical study of a PEG-based polymer and lithium perchlorate in three different molecular solvents by different NMR spectroscopic methods. The hydrodynamic radius of the polymer decreases while the temperature is increased. This shows the desolvation behavior of the polymer. Diffusion coefficients and the rotational correlation time shows strong coupling with the viscosity. Next the molecular dynamics study of the PEG based polymer inside the ionic liquid was performed. The study of the radius of gyration at temperatures shows that at higher temperatures, the polymer exists in a more linear form. The diffusion study of the polymer suggests that the nature of the diffusion is anomalous. The radial distribution function of the polymer and the ionic liquid are also discussed. Finally, the dynamics and the conformational flexibility of curcumin inside a DPPC lipid bilayer was studied. The entire diffusion dynamics exists in the

sub-diffusive regime. The C=C double bond in the enol form makes it rigid, while the keto form is more flexible. The flexibility of the keto form increases with an increase in the temperature.

The investigations carried out in this thesis show that combining experimental NMR spectroscopic data with results obtained from molecular dynamics simulations. Which can be combined to give deep insights into the structure and dynamics of small molecules interacting with different environments such as lipid membranes and ionic liquids.

References

[1] J. S. Bernstein, Applications of NMR to Pharmaceutical Technology. 1

[2] C. Corinne, NMR spectroscopy: From quantum mechanics to protein spectra, Concepts Magn. Reson. **9**(1), 17âĂŞ41. 1

[3] K. C. Wong, Review of NMR Spectroscopy: Basic Principles, Concepts and Applications in Chemistry, J. Chem. Educ **91**(8), 1103–1104 (2014). 1

[4] D. Marion, An Introduction to Biological NMR Spectroscopy, Mol. Cell. Proteomics **12**(11), 3006–3025 (2013). 1

[5] R. K. Sharma, K. Mishra, A. Farooqui, A. Behari, V. K. Kapoor, and N. Sinha, 1H nuclear magnetic resonance (NMR)-based serum metabolomics of human gallbladder inflammation, Inflamm. Res. **66**(1), 97–105 (Jan 2017). 1

[6] M. Rose, *Elementary Theory of Angular Momentum*, Dover Publications, 2011. 1

[7] F. H. Forsterling, Spin dynamics: Basics of Nuclear Magnetic Resonance, Second Edition, Med. Phys. **37**(1), 406–407. 1

[8] G. Harald, *NMR spectroscopy: basic principles concepts and applications in chemistry*, John Wiley & Sons, 2013. 1

[9] E. Pretsch, T. Clerc, J. Seibl, and W. Simon, *Tables of spectral data for structure determination of organic compounds*, Springer Science & Business Media, 2013. 1

[10] R. S. Macomber, *A complete introduction to modern NMR spectroscopy*, Wiley New York, 1998. 1

[11] R. R. Ernst, G. Bodenhausen, A. Wokaun, et al., *Principles of nuclear magnetic resonance in one and two dimensions*, volume 14, Clarendon Press Oxford, 1987. 1

[12] O. Zerbe and S. Jurt, *Applied NMR spectroscopy for chemists and life scientists*, John Wiley & Sons, 2013. 1

[13] H. Friebolin and J. K. Becconsall, *Basic one-and two-dimensional NMR spectroscopy*, VCH Weinheim, 1993. 1

[14] A. J. Dingley and S. M. Pascal, *Biomolecular NMR spectroscopy*, volume 3, Ios Press, 2011. 1

[15] M. Doucleff, M. Hatcher-Skeers, and N. J. Crane, *Pocket guide to biomolecular NMR*, Springer Science & Business Media, 2011. 1

[16] H. S. Atreya, *Isotope labeling in biomolecular NMR*, volume 992, Springer Science & Business Media, 2012. 1

[17] G. S. M. Reddy, T. Narasimhaswamy, B. V. N. P. Kumar, and K. M. Raju, Structural Assignment of Side Chain Liquid Crystalline Monomer and Polymer by 1-D and 2-D Solution NMR Studies, Int. J. Polym. Anal. Ch. **20**(1), 10–28 (2015). 1

[18] J. H. Simpson, *Organic structure determination using 2-D NMR spectroscopy: a problem-based approach*, Academic Press, 2011. 1

[19] N. E. Jacobsen, *NMR data interpretation explained: understanding 1D and 2D NMR spectra of organic compounds and natural products*, John Wiley & Sons, 2016. 1

[20] D. D. Traficante, Two-dimensional NMR methods for establishing molecular connectivity. A chemist's guide to experiment selection, performance, and interpretation., Concepts Magn. Reson. **3**(1), 49–50. 1

[21] S. A. Morris and T. C. Slesnick, Magnetic resonance imaging, Visual Guide to Neonatal Cardiology , 104–108 (2018). 1

[22] E. M. Haacke, R. W. Brown, M. R. Thompson, and R. R. Venkatesan, *Magnetic resonance imaging: physical principles and sequence design*, volume 82, Wiley-Liss New York:, 1999. 1

[23] R. C. Smith and R. C. Lange, *Understanding magnetic resonance imaging*, CRC Press, 1997. 1

[24] M. H. Levitt, *Spin dynamics: basics of nuclear magnetic resonance*, Wiley, 2001. 1

[25] J. Keeler, *Understanding NMR Spectroscopy*, John Wiley and Sons Ltd, 2005. 1

[26] T. D. W. Claridge, *High-Resolution NMR Techniques in Organic Chemistry (Third Edition)*, Elsevier, third edition edition, 2016. 1

[27] D. D. Traficante, Relaxation. Can T2 be longer than T1?, Concepts Magn. Reson. **3**(3), 171–177. 2

[28] R. Freeman, *Spin Choreography: Basic Steps in High Resolution NMR*, Oxford University Press, 1998. 2

[29] M. Chatell, F. Darcel, J. de Certaines, L. Benoist, and A. Bernard, T1 and T2 Proton Nuclear Magnetic Resonance (N.M.R.) relaxation times in vitro and human intracranial tumours, J. Neurooncol. **3**(4), 315–321 (1986). 2

[30] M. Goldman, Formal Theory of Spin-Lattice Relaxation, J. Magn. Reson **149**(2), 160 – 187 (2001). 3, 4

[31] W. S. Price, *NMR Studies of Translational Motion: Principles and Applications*, Cambridge Molecular Science, Cambridge University Press, 2009. 5, 9

[32] W. S. Price, Pulsed-field gradient nuclear magnetic resonance as a tool for studying translational diffusion: Part 1. Basic theory, Concepts Magn. Reson. **9**(5), 299–336. 8

[33] P. W. Kuchel, G. Pages, K. Nagashima, S. Velan, V. Vijayaragavan, V. Nagarajan, and K. H. Chuang, Stejskal-tanner equation derived in full, Concepts Magn. Reson. Part A. **40A**(5), 205–214. 8

[34] D.Sinnaeve, The Stejskal-Tanner equation generalized for any gradient shape-an overview of most pulse sequences measuring free diffusion, Concepts Magn. Reson. A **40A**(2), 39–65 (2012). 8

[35] J. E. Tanner and E. O. Stejskal, Restricted Self-Diffusion of Protons in Colloidal Systems by the Pulsed-Gradient Spin-Echo Method, J. Chem. Phys. **49**(4), 1768–1777 (1968). 8

[36] A. Viswan, C. Singh, R. K. Rai, A. Azim, N. Sinha, and A. K. Baronia, Metabolomics based predictive biomarker model of ARDS: A systemic measure of clinical hypoxemia, PLOS ONE **12**, 1–18 (11 2017). 9

[37] A. Singh, N. Deshpande, N. Pramanik, S. Jhunjhunwala, A. Rangarajan, and A. S. Hanudatta, Optimized peptide based inhibitors targeting the dihydrofolate reductase pathway in cancer, Sci. Rep. **8**(1), 3190 (2018). 9

[38] A. Pan, B. Naskar, G. K. S. Prameela, B. V. N. P. Kumar, A. B. Mandal, S. C. Bhattacharya, and S. P. Moulik, Amphiphile Behavior in Mixed Solvent Media I: Self-Aggregation and Ion Association of Sodium Dodecylsulfate in 1,4-Dioxane-Water and Methanol-Water Media, Langmuir **28**(39), 13830–13843 (2012). 9

[39] S. R. Chaudhari and N. Suryaprakash, Diffusion ordered spectroscopy for resolution of double bonded cis, trans-isomers, J. Mol. Struct. **1017**, 106–108 (2012). 9

[40] R. R. Reddy, G. Shanmugam, B. Madhan, and B. V. N. P. Kumar, Selective binding and dynamics of imidazole alkyl sulfate ionic liquids with human serum albumin and collagen - a detailed NMR investigation, Phys. Chem. Chem. Phys. **20**, 9256–9268 (2018). 9

[41] S. K. Mishra and N. Suryaprakash, Pure shift edited ultra high resolution NMR spectrum with complete eradication of axial peaks and unwanted couplings, jmr **279**, 74–80 (2017). 9

[42] H. Adam, G. J. Ramon, O. Modesto, and J. L. Gelpi, Molecular dynamics simulations: advances and applications, Adv. Appl. Bioinform. Chem. **8**, 37–47 (2015). 9

[43] S. K. Mishra and N. Suryaprakash, Intramolecular hydrogen bonding involving organic fluorine: NMR investigations corroborated by DFT-based theoretical calculations, Molecules **22**(3), 423 (2017). 9

[44] Y. Duan, C. Wu, S. Chowdhury, M. C. Lee, G. Xiong, W. Zhang, R. Yang, P. Cieplak, R. Luo, T. Lee, J. Caldwell, J. Wang, and P. Kollman, A point-charge force field for molecular mechanics simulations of proteins based on condensed-phase quantum mechanical calculations, J. Comput. Chem. **24**(16), 1999–2012. 11, 14

[45] B. R. Brooks, R. E. Bruccoleri, B. D. Olafson, D. J. States, S. Swaminathan, and M. Karplus, CHARMM: A program for macromolecular energy minimization and dynamics calculations, J. Comput. Chem. **4**(2), 187–217. 11, 14

[46] W. R. P. Scott, P. H. Hunenberger, I. G. Tironi, A. E. Mark, S. R. Billeter, J. Fennen, A. E. Torda, T. Huber, P. Kruger, and W. F. van Gunsteren, The GROMOS Biomolecular Simulation Program Package, J. Phys. Chem. A **103**(19), 3596–3607 (1999). 11, 15

[47] J. W. L., M. D. S., and T.-R. Julian, Development and Testing of the OPLS All-Atom Force Field on Conformational Energetics and Properties of Organic Liquids, J. Am. Chem. Soc. **118**(45), 11225–11236 (1996). 11, 15

[48] K. Martin and P. G. A., Molecular dynamics simulations in biology, Nature **347**, 631 (oct 1990). 11

[49] B. J. Alder and T. E. Wainwright, Studies in Molecular Dynamics. I. General Method, J. Chem. Phys. **31**(2), 459–466 (1959). 11

[50] J. Durrant and J. McCammon, Molecular dynamics simulations and drug discovery, BMC Biology **9**(1), 71 (2011). 11

[51] S. J. Marrink, H. J. Risselada, S. Yefimov, D. P. Tieleman, and A. H. de Vries, The MARTINI Force Field: Coarse Grained Model for Biomolecular Simulations, J. Phys. Chem. B **111**(27), 7812–7824 (2007). 12

[52] B. Hess, H. Bekker, H. Berendsen, J. G. Fraaije, et al., LINCS: a linear constraint solver for molecular simulations, J. Comput. Chem. **18**(12), 1463–1472 (1997). 13, 23, 55, 68

[53] H. C. Andersen, Rattle: A velocity version of the shake algorithm for molecular dynamics calculations, J. Comput. Phys. **52**(1), 24 – 34 (1983). 13

[54] M. J. Abraham, T. Murtola, R. Schulz, S. Pall, J. C. Smith, B. Hess, and E. Lindahl, GROMACS: High performance molecular simulations through multi-level parallelism from laptops to supercomputers, SoftwareX **1-2**, 19 – 25 (2015). 14

[55] H. Berendsen, D. van der Spoel, and R. van Drunen, GROMACS: A message-passing parallel molecular dynamics implementation, Comput. Phys. Commun. **91**(1), 43 – 56 (1995). 14

[56] E. Lindahl, B. Hess, and D. van der Spoel, GROMACS 3.0: a package for molecular simulation and trajectory analysis, J. Mol. Model. **7**(8), 306–317 (Aug 2001). 14

[57] *Gromacs 4.5.4 Manual: http://www.gromacs.org/Documentation/Manual*, 2011. 15

[58] J. Crank, *The mathematics of diffusion by J. Crank*, Clarendon Press, 1975. 17

[59] C. Peschel, M. Brehm, and D. Sebastiani, Polyphilic Interactions as Structural Driving Force Investigated by Molecular Dynamics Simulation, polymers **9**, 445 (2017). 19

[60] C. R. Sanders and J. P. Schwonek, Characterization of magnetically orientable bilayers in mixtures of dihexanoylphosphatidylcholine and dimyristoylphosphatidylcholine by solid-state NMR, Biochemistry **31**(37), 8898–8905 (1992). 19

[61] M. Shintani, Y. Matsuo, S. Sakuraba, and N. Matubayasi, Interaction of naphthalene derivatives with lipids in membranes studied by the 1H-nuclear Overhauser effect and molecular dynamics simulation, Phys. Chem. Chem. Phys. **14**, 14049–14060 (2012). 20

[62] H. Khandelia, S. Witzke, and O. G. Mouritsen, Interaction of salicylate and a terpenoid plant extract with model membranes: reconciling experiments and simulations, Biophys. J. **99**, 3887–3894 (2010). 20

[63] W. Kopec, J. Telenius, and H. Khandelia, Molecular dynamics simulations of the interactions of medicinal plant extracts and drugs with lipid bilayer membranes, Febs J. **280**, 2785–2805 (2013). 20

[64] J. L. MacCallum and D. P. Tieleman, Interactions between small molecules and lipid bilayers, Curr. Top. Membr. **60**, 227–256 (2008). 20

[65] S. Qin, Z. Yu, and Y. Yu, Structural and Kinetic Properties of α-Tocopherol in Phospholipid Bilayers, a Molecular Dynamics Simulation Study, J. Phys. Chem. B **113**, 16537–16546 (2009). 20

[66] M. Brehm, G. Saddiq, T. Watermann, and D. Sebastiani, Influence of Small Fluorophilic and Lipophilic Organic Molecules on Dipalmitoylphosphatidylcholine Bilayers, J. Phys. Chem. B **121**, 8311–8321 (2017). 20

[67] D. Lopes, S. Kakobtorweihen, C. Nunes, B. Sarmento, and S. Reis, Shedding light on the puzzle of drug-membrane interactions: Experimental techniques and molecular dynamics simulations, Prog. Lipid Res. **65**, 24–44 (2017). 20

[68] M. B. Boggara and R. Krishnamoorti, Partitioning of nonsteroidal antiinflammatory drugs in lipid membranes: a molecular dynamics simulation study, Biophys. J. **98**, 586–595 (2010). 20

[69] C. B. Fox, R. A. Horton, and J. M. Harris, Detection of drug-membrane interactions in individual phospholipid vesicles by confocal Raman microscopy, Anal. Chem. **78**, 4918–4924 (2006). 21

[70] F. Li, L. Wang, N. Xiao, M. Yang, L. Jiang, and M. Liu, Dominant Conformation of Valsartan in Sodium Dodecyl Sulfate Micelle Environment, J. Phys. Chem. B **114**(8), 2719–2727 (2010). 21

[71] C. Cao, J. Mao, F. Li, M. Yang, H. He, L. Jiang, and M. Liu, Understanding the Interaction between Valsartan and Detergents by NMR Techniques and Molecular Dynamics Simulation, J. Phys. Chem. B **116**(25), 7470–7478 (2012). 21

[72] M. Zervou, Z. Cournia, C. Potamitis, G. Patargias, S. Durdagi, S. G. Grdadolnik, and T. Mavromoustakos, Insights into the molecular basis of action of the AT1 antagonist losartan using a combined NMR spectroscopy and computational approach, Biochim. Biophys. Acta **1838**(3), 1031 – 1046 (2014). 21

[73] Y. H. Song, V. Guallar, and N. A. Baker, Molecular dynamics simulations of salicylate effects on the micro-and mesoscopic properties of a dipalmitoylphosphatidylcholine bilayer, Biochemistry **44**, 13425–13438 (2005). 21

[74] M. Orsi and J. W. Essex, Permeability of drugs and hormones through a lipid bilayer: insights from dual-resolution molecular dynamics, soft matter **6**, 3797–3808 (2010). 21

[75] Y. N. Abdiche and D. G. Myszka, Probing the mechanism of druglipid membrane interactions using Biacore, Analytical Biochemistry **328**(2), 233 – 243 (2004). 21

[76] B. Fichtl, B. Bondy, and H. Kurz, Binding of drugs to muscle tissue: dependence on drug concentration and lipid content of tissue., J. Pharmacol. Exp. Ther. **215**(1), 248–253 (1980). 21

[77] A. Ambrosini, G. Bossi, S. Dante, B. Dubini, L. Gobbi, L. Leone, M. G. P. Bossi, and G. Zolese, Lipid-drug interaction: thermodynamic and structural effects of antimicotic fluconazole on DPPC liposomes, Chem. Phys. Lipids. **95**(1), 37 – 47 (1998). 21

[78] C. Peetla, A. Stine, and V. Labhasetwar, Biophysical Interactions with Model Lipid Membranes: Applications in Drug Discovery and Drug Delivery, Mol. Pharm. **6**(5), 1264–1276 (2009). 21

[79] C. Schwieger, A. Achilles, S. Scholz, J. Ruger, K. Bacia, K. Saalwachter, and J. Kressler, Binding of amphiphilic and triphilic block copolymers to lipid model membranes: the role of perfluorinated moieties, soft matter **10**, 6147–6160 (2014). 21

[80] M. P. Krafft, Fluorocarbons and fluorinated amphiphiles in drug delivery and biomedical research, Adv. Drug. Deliv. Rev. **47**, 209–228 (2001). 21

[81] I. Turel, The interactions of metal ions with quinolone antibacterial agents, Coord. Chem. Rev. **232**, 27–47 (2002). 21

[82] P. Drevensek, J. Kosmrlj, G. Giester, T. Skauge, E. Sletten, K. Sepcic, and I. Turel, X-Ray crystallographic, NMR and antimicrobial activity studies of magnesium complexes of fluoroquinolones - racemic ofloxacin and its S-form, levofloxacin, J. Inorg. Biochem. **100**(11), 1755 – 1763 (2006). 21

[83] V. D. S. David, L. Erik, H. Berk., G. Gerrit, M. A. E., and B. H. J. C., GROMACS: Fast, flexible, and free, J. Comput. Chem. **26**(16), 1701–1718 (2005). 22, 55, 67

[84] C. Oostenbrink, A. Villa, A. Mark, and W. Gunsteren, A biomolecular force field based on the free enthalpy of hydration and solvation: The GROMOS force-field parameter sets 53A5 and 53A6, J. Comput. Chem. **25**(13), 1656–1676 (2004). 22, 55, 67

[85] A. K. Malde, L. Zuo, M. Breeze, M. Stroet, D. Poger, P. Nair, C. Oostenbrink, and A. E. Mark, An Automated Force Field Topology Builder (ATB) and Repository: Version 1.0, J. Chem. Theory Comput. **7**(12), 4026–4037 (2011). 22, 55, 67

[86] Sch A. W. üttelkopf and D. M. F. v. Aalten, PRODRG: a tool for high-throughput crystallography of protein-ligand complexes, Acta Crystallogr **D60**, 1355–1363 (2004). 22

[87] H. J. C. Berendsen, J. P. M. Postma, W. F. V. Gunsteren, A. Dinola, and J. R. Haak, Molecular dynamics with coupling to an external bath, J. Chem. Phys **81**, 3684–3690 (1984). 22, 55

[88] U. Essmann, L. Perera, M. L. Berkowitz, T. Darden, H. Lee, and L. G. Pedersen, A smooth particle mesh Ewald method, J. Chem. Phys. **103**, 8577–8593 (1995). 23, 55, 68

[89] S. Feng and G. Voth, Molecular dynamics simulations of imidazolium-based ionic liquid/water mixtures: Alkyl side chain length and anion effects, Fluid Ph. Equilibria **294**(1), 148–156 (2010). 24, 58

[90] M. G. Wolf, H. Grubmuller, and G. Groenhof, Anomalous Surface Diffusion of Protons on Lipid Membranes, Biophys. J. **107**, 76 – 87 (2014). 28, 29, 60

[91] M. Javanainen, H.Hammaren, L. Monticelli, J. Jeon, M. S. Miettinen, M. S., Hector, R. Metzler, and I.Vattulainen, Anomalous and normal diffusion of proteins and lipids in crowded lipid membranes, Farad. Discuss. **161**, 397–417 (2013). 30

[92] K. Ritchie, X. Shan, J. Kondo, K. Iwasawa, T. Fujiwara, and A. Kusumi, Detection of Non-Brownian Diffusion in the Cell Membrane in Single Molecule Tracking, Biophys. J. **88**(3), 2266 – 2277 (2005). 30, 60

[93] R.Black, B.Adams, and L. Nazar, Non-Aqueous and Hybrid Li-O2 Batteries, Adv. Energy Mater. **2**(7), 801–815 (2012). 33

[94] H.Wang, A.C.Forse, J.M.Griffin, N.M.Trease, L.Trognko, P.L.Taberna, P.Simon, and C.P.Grey, In Situ NMR Spectroscopy of Supercapacitors: Insight into the Charge Storage Mechanism, J. Am. Chem. Soc. **135**(50), 18968–18980 (2013). 33

[95] B.Dunn, H.Kamath, and J.M.Tarascon, Electrical Energy Storage for the Grid: A Battery of Choices, Science **334**(6058), 928–935 (2011). 33

[96] Z.Xue, D.He, and X.Xie, Poly(ethylene oxide)-based electrolytes for lithium-ion batteries, J. Mater. Chem. A **3**, 19218–19253 (2015). 33, 34

[97] C. Do, P. Lunkenheimer, D. Diddens, M. Götz, M. Weiss, A.Loidl, X.G.Sun, J.Allgaier, and M.Ohl, Li^+ transport in poly(ethylene oxide) based electrolytes: neutron scattering, dielectric spectroscopy, and molecular dynamics simulations., Phys. Rev. Lett. **111**, 018301 (Jul 2013). 34

[98] J. H. Ma, C. Guo, Y. L. Tang, and H. Z. Liu, 1H NMR Spectroscopic Investigations on the Micellization and Gelation of PEO-PPO-PEO Block Copolymers in Aqueous Solutions, Langmuir **23**(19), 9596–9605 (2007). 34, 36, 40

[99] M.Z.Jora, M. Cardoso, and E.Sabadini, Dynamical aspects of water-poly(ethylene glycol) solutions studied by 1H NMR, J Mol Liq **222**, 94 – 100 (2016). 34

[100] A. Graaf, K.W.M.Boere, J.Kemmink, R.G.Fokkink, C. Nostrum, D.T.S.Rijkers, J. der Gucht, H.Wienk, M.Baldus, E.Mastrobattista, T.Vermonden, and W.E.Hennink, Looped Structure of Flowerlike Micelles Revealed by 1H NMR Relaxometry and Light Scattering, Langmuir **27**(16), 9843–9848 (2011). 34

[101] J.Weiss, H.Wienk, R.Boelens, and A.Laschewsky, Block Copolymer Micelles with an Intermediate Star-/Flower-Like Structure Studied by 1H NMR Relaxometry, Macromol. Chem. Phys. **215**(9), 915–919 (2014). 34

[102] M. Joost, M. Kunze, S. Jeong, M. Schonhoff, M. Winter, and S. Passerini, Ionic mobility in ternary polymer electrolytes for lithium-ion batteries, âĂŐElectochim. Acta **86**, 330–338 (2012). 34

[103] A.Gong, C.Liu, Y. Chen, C.Chen, and F.Xi, Ionic conductivity of alkali-metal carboxylated dendritic poly(amidoamine) electrolytes and their lithium perchlorate salt complex, Polymer **41**(16), 6103 – 6111 (2000). 34

[104] K. Hayamizu, S. Tsuzuki, and S. Seki, Temperature-dependent 11B spin-lattice relaxation time for BF4 and CF3BF3 anions in room-temperature ionic liquids, Magn. Reson. Chem. **49**(1), 6–8 (2011). 34

[105] L.Qingwen, J.Yang, W.Lu, J.Wang, and Y.Nuli, Advanced semi-interpenetrating polymer network gel electrolyte for rechargeable lithium batteries, Electrochimica Acta **152**, 489 – 495 (2015). 34

[106] J. C. Daigle, A. Vijh, P. Hovington, C. Gagnon, J. H. Paquet, S. Verreault, N. Turcotte, D. Clement, A. Guerfi, and K. Zaghib, Lithium battery with solid polymer electrolyte based on comb-like copolymers, J. Power Sources **279**, 372 – 383 (2015). 34

[107] J. F. Velez, M. Aparicio, and J. Mosa, Effect of Lithium Salt in Nanostructured Silica-Polyethylene Glycol Solid Electrolytes for Li-Ion Battery Applications, J. Phys. Chem. C **120**, 22852–22864 (2016). 34

[108] R. Nanda, P. R. Rajamohanan, and A. Kumar, Experimental Signature of Micro-heterogeneity in Ionic Liquid-H2O Systems and Their Perturbation by Adding Li+ Salts: A Pulsed Gradient Spin-Echo NMR Approach, Chem. Phys. Chem. **16**(14), 2936–2941 (2015). 35

[109] R. Nanda, Unusual linear dependency of viscosity with temperature in ionic liquid/water mixtures, Phys. Chem. Chem. Phys. **18**, 25801–25805 (2016). 35

[110] E.O.Stejskal and J.E.Tanner, Spin Diffusion Measurements Spin Echoes in the Presence of a Time-Dependent Field Gradient, J. Chem. Phys. **42**, 288–292 (1965). 35

[111] R. Nanda, Thermal dynamics of lithium salt mixtures of ionic liquid in water by PGSE NMR spectroscopy, RSC Adv. **6**, 36394–36406 (2016). 36, 40

[112] R. Nanda and A. Kumar, Phase Behavior, Diffusion, Structural Characteristics, and pH of Aqueous Hydrophobic Ionic Liquid Confined Media: Insights into Microviscosity and Microporsity in the [C4C4im][NTf2] $^{+}$ Water System, J. Phys. Chem. B **119**(4), 1641–1653 (2015). 36

[113] G. M. Veith, J. Nanda, L. H. Delmau, and N. J. Dudney, Influence of Lithium Salts on the Discharge Chemistry of Li-Air Cells, J. Phys. Chem. Lett **3**(10), 1242–1247 (2012). 36

[114] F. Castiglione, E. Ragg, A. Mele, G. B. Appetecchi, M. Montanino, and S. Passerini, Molecular Environment and Enhanced Diffusivity of Li^{+} Ions in Lithium-Salt-Doped Ionic Liquid Electrolytes, J. Phys. Chem. Lett. **2**(3), 153–157 (2011). 36

[115] J. Ma, C. Guo, Y. Tang, J. Xiang, S. Chen, J. Wang, and H.Liu, Micellization in aqueous solution of an ethylene oxide-propylene oxide triblock copolymer, investigated with 1H {NMR} spectroscopy, pulsed-field gradient NMR,

and {NMR} relaxation, J. Colloid. Interface Sci. **312**(2), 390 – 396 (2007). 36, 47

[116] E.A.Bekturov, S.S.Ismagulova, and T.K.Dzumadilov, Complexation of poly(ethylene glycol) with lithium salts in solution, Die Makromolekulare Chemie **191**(6), 1329–1333 (1990). 36

[117] K. J. Liu and R. Ullman, Proton Magnetic Relaxation in Polyethylene Oxide Solutions, J. Chem. Phys. **48**, 1158–1168 (Feb. 1968). 36, 47

[118] B.J.Kim, S.S.Im, and S.G.Oh, Investigation on the Solubilization Locus of Aniline-HCl Salt in SDS Micelles with 1H NMR Spectroscopy, Langmuir **17**(2), 565–566 (2001). 40

[119] T. Shikata, A. Minakawa, and K. Okuyama, Structure, Dynamics, and Hydration of a Collagen Model Polypeptide, (l-Prolyl-l-ProlylGlycyl)10, in Aqueous Media: a Chemical Equilibrium Analysis of Triple Helix-to-Single Coil Transition, J. Phys. Chem. B **113**(43), 14504–14512 (2009). 40, 44, 45

[120] S. Magazu, NMR, static and dynamic light and neutron scattering investigations on polymeric aqueous solutions, J. Mol. Struct. **523**(1-3), 47 – 59 (2000). 40, 44

[121] A. Faraone, S. Magazu, G. Maisano, P. Migliardo, E. Tettamanti, and V. Villari, The puzzle of poly (ethylene oxide) aggregation in water: Experimental findings, J. Chem. Phys. **110**(3), 1801–1806 (1999). 40, 44, 45

[122] F. Cau and S.Lacelle, H NMR Relaxation Studies of the Micellization of a Poly(ethylene oxide)-Poly(propylene oxide)-Poly(ethylene oxide) Triblock Copolymer in Aqueous Solution, Macromolecules **29**(1), 170–178 (1996). 41

[123] M. J. Hey, S. M. Ilett, and G. Davidson, Effect of temperature on poly(ethylene oxide) chains in aqueous solution. A viscometric, 1H NMR and Raman spectroscopic study, J. Chem. Soc., Faraday Trans. **91**, 3897–3900 (1995). 41

[124] K. Mortensen and J. S. Pedersen, Structural study on the micelle formation of poly(ethylene oxide)-poly(propylene oxide)-poly(ethylene oxide) triblock copolymer in aqueous solution, Macromolecules **26**(4), 805–812 (1993). 44

[125] B. A. Borgias, M. Gochin, D. J. Kerwood, and T. L. James, Relaxation matrix analysis of 2D NMR data, Prog. Nucl. Magn. Reson. Spectrosc. **22**(1), 83 – 100 (1990). 48, 49

[126] R. Rogers and K. Seddon, Ionic liquids–solvents of the future?, Science **302**(5646), 792–793 (2003). 53

[127] C. J. Margulis, Computational study of imidazolium-based ionic solvents with alkyl substituents of different lengths, Mol. Phys. **102**(9-10), 829–838 (2004). 53

[128] M. Armand, F. Endres, D. MacFarlane, H. Ohno, and B. Scrosati, Ionic-liquid materials for the electrochemical challenges of the future, Nat. Mater. **8**(8), 621–629 (2009). 53

[129] C. Rey-Castro and L. F. Vega, Transport Properties of the Ionic Liquid 1-Ethyl-3-Methylimidazolium Chloride from Equilibrium Molecular Dynamics Simulation. The Effect of Temperature, J. Phys. Chem. B **110**, 14426–14435 (2006). 53

[130] P. A. Suarez, J. E. Dullius, S. Einloft, R. D. Souza, and J. Dupont, The use of new ionic liquids in two-phase catalytic hydrogenation reaction by rhodium complexes, Polyhedron **15**(7), 1217–1219 (1996). 53

[131] R. Sheldon, Catalytic reactions in ionic liquids, Chemical Communications , 2399–2407 (2001). 53

[132] W. Peter and K. Wilhelm, Ionic Liquids-New "Solutions" for Transition Metal Catalysis, Angew. Chem. Int. Ed. **39**(21), 3772–3789. 53

[133] J. Peng and Y. Deng, Cycloaddition of carbon dioxide to propylene oxide catalyzed by ionic liquids, New J. Chem **25**(4), 639–641 (2001). 53

[134] W. Wu, B. Han, H. Gao, Z. Liu, T. Jiang, and J. Huang, Desulfurization of flue gas: SO2 absorption by an ionic liquid, Angew. Chem. Int. Ed. **43**(18), 2415–2417 (2004). 53

[135] J. Anthony, E. Maginn, and J. Brennecke, Solubilities and thermodynamic properties of gases in the ionic liquid 1-n-butyl-3-methylimidazolium hexafluorophosphate, J. Phys. Chem. B **106**(29), 7315–7320 (2002). 53

[136] V. Baranchugov, E. Markevich, E. Pollak, G. Salitra, and D. Aurbach, Amorphous silicon thin films as a high capacity anodes for Li-ion batteries in ionic liquid electrolytes, Electrochem. Commun. **9**(4), 796–800 (2007). 53

[137] H. Nakajima and H. Ohno, Preparation of thermally stable polymer electrolytes from imidazolium-type ionic liquid derivatives, Polymer **46**(25), 11499–11504 (2005). 53

[138] W. Liu, C. Ye, Q. Gong, H. Wang, and P. Wang, Tribological performance of room-temperature ionic liquids as lubricant, Tribol. Lett. **13**(2), 81–85 (2002). 54

[139] H. Wang, Q. Lu, C. Ye, W. Liu, and Z. Cui, Friction and wear behaviors of ionic liquid of alkylimidazolium hexafluorophosphates as lubricants for steel/steel contact, Wear **256**(1), 44–48 (2004). 54

[140] M. Chen, R. Pendrill, G. Widmalm, J. W. Brady, and J. Wohlert, Molecular Dynamics Simulations of the Ionic Liquid 1-n-Butyl-3- Methylimidazolium Chloride and Its Binary Mixtures with Ethanol, J. Chem. Theory Comput. **10**, 4465–4479 (2014). 54

[141] T. A. Lodge, Unique platform for materials design, Science **321**, 50–51 (2008). 54

[142] C. Tiyapiboonchaiya, D. R. MacFarlane, J. Sun, and M. Forsyth, Polymer-in-ionic-liquid electrolytes, Macromolecular chemistry and physics **203**(13), 1906–1911 (2002). 54

[143] S. Y. Kim, S. Kim, and M. Park, Enhanced proton transport in nanostructured polymer electrolyte/ionic liquid membranes under water-free conditions, Nat. Commun. **1**, 88 (2010). 54

[144] C. M. S. S. Neves, K. A. Kurnia, J. A. P. Coutinho, i. M. Marrucho, J. N. C. Lopes, M. G. Freire, and L. P. N. Rebelo, Systematic Study of the Thermophysical Properties of Imidazolium-Based Ionic Liquids with Cyano-Functionalized Anions, J. Phys. Chem. B **117**(35), 10271–10283 (2013). 54

[145] Y. Wang, H. Pan, H. Li, and C. Wang, Force Field of the TMGL Ionic Liquid and the Solubility of SO2 and CO2 in the TMGL from Molecular Dynamics Simulation, J. Phys. Chem. B **111**(35), 10461–10467 (2007). 54

[146] J. F. B. Pereira, K. A. Kurnia, M. G. Freire, J. A. P. Coutinho, and R. D. Rogers, Controlling the Formation of Ionic-Liquid-based Aqueous Biphasic Systems by Changing the Hydrogen Bonding Ability of Polyethylene Glycol End Groups, Chem. Phys. Chem **16**(10), 2219–2225 (2015). 54

[147] J. Mondal, E. Choi, and A. Yethiraj, Atomistic Simulations of Poly(ethylene oxide) in Water and an Ionic Liquid at Room Temperature, Macromolecules **47**(1), 438–446 (2014). 54

[148] L. T. Costa, B. Sun, F. Jeschull, and D. Brandell, Polymer-ionic liquid ternary systems for Li-battery electrolytes: Molecular dynamics studies of LiTFSI in a EMIm-TFSI and PEO blend, J. Chem. Phys. **143**(2), 024904 (2015). 54

[149] H. Asai, K. Fujii, K. Nishi, T. Sakai, K. Ohara, Y. Umebayashi, and M. Shibayama, Solvation Structure of Poly(ethylene glycol) in Ionic Liquids Studied by High-energy X-ray Diffraction and Molecular Dynamics Simulations, Macromolecules **46**, 2369–2375 (2013). 54

[150] C. M. S. S. Neves, S. Shahriari, J. Lemus, J. F. B. Pereira, M. G. Freire, and J. A. P. Coutinho, Aqueous biphasic systems composed of ionic liquids and polypropylene glycol: insights into their liquid-liquid demixing mechanisms, Phys. Chem. Chem. Phys. **18**(30), 20571–20582 (2016). 54

[151] L. I. N. Tome, J. F. B. Pereira, R. D. Rogers, M. G. Freire, J. R. B. Gomes, and J. A. P. Coutinho, Evidence for the Interactions Occurring Between Ionic Liquids and Tetraethylene Glycol in Binary Mixtures and Aqueous Biphasic Systems, J. Phys. Chem. B **118**, 4615–4629 (2014). 54

[152] H. J. C. Berendsen, D. van der Spoel, and R. van Drunen, GROMACS: A message-passing parallel molecular dynamics implementation, Comput. Phys. Commun. **91**(1), 43 – 56 (1995). 55, 67

[153] T. Darden, D. York, and L. Pedersen, Particle mesh Ewald: An N.log(N) method for Ewald sums in large systems, J. Chem. Phys. **98**(12), 10089–10092 (1993). 55, 68

[154] E. Lindahl, B. Hess, and D. V. D. Spoel, GROMACS 3.0: a package for molecular simulation and trajectory analysis, J Mol Model **7**(8), 306–317 (2001). 55

[155] S. Pall and B. Hess, A flexible algorithm for calculating pair interactions on {SIMD} architectures, Comput. Phys. Commun. **184**(12), 2641 – 2650 (2013). 55

[156] F. Yuan and R. Larson, Multiscale Molecular Dynamics Simulations of Model Hydrophobically Modified Ethylene Oxide Urethane Micelles, J. Phys. Chem. B **119**(38), 12540–12551 (2015). 56

[157] A. Triolo, O. Russina, U. Keiderling, and J. Kohlbrecher, Morphology of poly(ethylene oxide) dissolved in a room temperature ionic liquid: A small angle neutron scattering study, J. Phys. Chem. B **110**, 1513–1515 (2006). 56

[158] A. Filippov, N. Azancheev, M. Taher, F. Shah, P. Rabet, S. Glavatskih, and O. Antzutkin, Self-diffusion and interactions in mixtures of imidazolium bis(mandelato)borate ionic liquids with polyethylene glycol: 1H NMR study, Magn. Reson. Chem. **53**(7), 493–497 (2015). 62

[159] T. Masuda, K. Hidaka, A. Shinohara, T. Maekawa, Y. Takeda, and H. Yamaguchi, Chemical Studies on Antioxidant Mechanism of Curcuminoid Analysis of Radical Reaction Products from Curcumin, J. Agric. Food Chem **47**(1), 71–77 (1999). 65

[160] E. Kunchandy and M. Rao, Oxygen radical scavenging activity of curcumin, Int. J. Pharm. **58**(3), 237 – 240 (1990). 65

[161] Y. He, Y. Yue, X. Zheng, K. Zhang, S. Chen, and Z. Du, Curcumin Inflammation and Chronic Diseases: How Are They Linked?, Molecules **20**(5), 9183–9213 (2015). 65

[162] K. Ono, K. Hasegawa, H. Naiki, and M. Yamada, Curcumin has potent anti amyloidogenic effects for Alzheimer s amyloid fibrils in vitro, J. Neurosci. Res. **75**(6), 742–750 (2004). 65

[163] M. Garcia-Alloza, L. A. Borrelli, A. Rozkalne, B. T. Hyman, and B. J. Bacskai, Curcumin labels amyloid pathology in vivo, disrupts existing plaques, and partially restores distorted neurites in an Alzheimer mouse model, J. Neurochem. **102**(4), 1095–1104 (2007). 65

[164] A. N. Begum, M. R. Jones, G. P. Lim, T. Morihara, P. Kim, D. D. Heath, C. L. Rock, M. A. Pruitt, F. Yang, B. Hudspeth, S. Hu, K. F. Faull, B. Teter, G. M. Cole, and S. A. Frautschy, Curcumin Structure-Function, Bioavailability, and Efficacy in Models of Neuroinflammation and Alzheimers Disease, J. Pharmacol. Exp. Ther. **326**(1), 196–208 (2008). 65

[165] F. Yang, G. P. Lim, A. N. Begum, O. J. Ubeda, M. R. Simmons, S. S. Ambegaokar, P. P. Chen, R. Kayed, C. G. Glabe, S. A. Frautschy, and G. M. Cole, Curcumin Inhibits Formation of Amyloid β-Oligomers and Fibrils, Binds Plaques, and Reduces Amyloid in Vivo, J. Biol. Chem. **280**(7), 5892–5901 (2005). 65

[166] A. Goel and B. B. Aggarwal, Curcumin, the Golden Spice From Indian Saffron, Is a Chemosensitizer and Radiosensitizer for Tumors and Chemoprotector and Radioprotector for Normal Organs, Nutr. Cancer **62**(7), 919–930 (2010). 65

[167] K. Hee-Je, K. Dong-Jo, S. Karthick, K. Hemalatha, C. J. Raj, S. ok, and C. Youngson, Curcumin Dye Extracted from Curcuma longa L. Used as Sensitizers for Efficient Dye-Sensitized Solar Cells, Int. J. Electrochem. Sci. , 8320 – 8328 (2013). 65

[168] P. Davari and H. I. Maibach, contact urticaria to cosmetic and industrial dyes, Clin. Exp. Dermatol. **36**(1), 1–5 (2011). 65

[169] G. M. S. Gonsalves, G. H. Silva, P. P. Barros, S. M. Srebernich, C. T. C. Shiraishi, V. R. Camargos, and T. B. Lasca, Use of Curcuma longa in cosmetics: extraction of curcuminoid pigments, development of formulations, and in vitro skin permeation studies, Braz. J. Pharm. Sci. **50**, 885 – 893 (12 2014). 66

[170] L. R. C. Barclay, M. R. Vinqvist, K. Mukai, H. Goto, Y. Hashimoto, A. Tokunaga, and H. Uno, On the Antioxidant Mechanism of Curcumin: Classical Methods Are Needed To Determine Antioxidant Mechanism and Activity, Org. Lett. **2**(18), 2841–2843 (2000). 66

[171] J. Duan, Y. Zhang, S. Han, Y. Chen, B. Li, M. Liao, W. Chen, X. Deng, J. Zhao, and B. Huang, Synthesis and in vitro/in vivo anti-cancer evaluation of curcumin-loaded chitosan/poly(butyl cyanoacrylate) nanoparticles, Int. J. Pharm. **400**(1), 211 – 220 (2010). 66

[172] B. B. Aggarwal and K. B. Harikumar, Potential therapeutic effects of curcumin, the anti-inflammatory agent, against neurodegenerative, cardiovascular, pulmonary, metabolic, autoimmune and neoplastic diseases, Int. J. Biochem. Cell Biol. **41**(1), 40 – 59 (2009). 66

[173] T. Hamaguchi, K. Ono, and M. Yamada, REVIEW: Curcumin and Alzheimer s Disease, CNS Neurosci. Ther. **16**(5), 285–297 (2010). 66

[174] D. Patra and C. Barakat, Synchronous fluorescence spectroscopic study of solvatochromic curcumin dye, Spectrochim. Acta A **79**(5), 1034 – 1041 (2011). 66

[175] M. Heger, R. F. van Golen, M. Broekgaarden, and M. C. Michel, The Molecular Basis for the Pharmacokinetics and Pharmacodynamics of Curcumin and Its Metabolites in Relation to Cancer, Pharmacol. Rev. **66**(1), 222–307 (2014). 66

[176] P. Anand, A. B. Kunnumakkara, R. A. Newman, and B. B. Aggarwal, Bioavailability of Curcumin: Problems and Promises, Mol. Pharm. **4**(6), 807–818 (2007). 66

[177] S. Jalili and M. Saeedi, Study of curcumin behavior in two different lipid bilayer models of liposomal curcumin using molecular dynamics simulation, J. Biomol. Struct. Dyn. **34**(2), 327–340 (2016). 66

[178] K. Saravanan, C. Kalaiarasi, and P. Kumaradhas, Understanding the conformational flexibility and electrostatic properties of curcumin in the active site of rhAChE via molecular docking, molecular dynamics and charge density analysis, J. Biomol. Struct. Dyn. **35**(16), 3627–3647 (2017). 66

[179] S. Karmakar, V. A. Raghunathan, and S. Mayor, Phase behaviour of dipalmitoyl phosphatidylcholine (DPPC)-cholesterol membranes, J. Phys. Condens. Matter **17**(14), S1177 (2005). 66

[180] B. Hess, C. Kutzner, D. Spoel, and E. Lindahl, GROMACS 4: Algorithms for Highly Efficient Load-Balanced and Scalable Molecular Simulation, J. Chem. Theory Comput. **4**(3), 435–447 (2008). 67, 68

[181] D.Poger, V.Gunsteren, F. Wilfred, and A. M. , A new force field for simulating phosphatidylcholine bilayers, J. Comput. Chem. **31**(6), 1117–1125 (2010). 67

[182] O. Berger, O. Edholm, and F. Jahnig, Molecular dynamics simulations of a fluid bilayer of dipalmitoylphosphatidylcholine at full hydration, constant pressure, and constant temperature, Biophys. J. **72**(5), 2002 – 2013 (1997). 67

[183] C. Wennberg, T. Murtola, B. Hess, and E. Lindahl, Lennard-Jones Lattice Summation in Bilayer Simulations Has Critical Effects on Surface Tension and Lipid Properties, J. Chem. Theory Comput. **9**(8), 3527–3537 (2013). 68

[184] C. Wennberg, T. Murtola, S. Pall, M. Abraham, B. Hess, and E. Lindahl, Direct-Space Corrections Enable Fast and Accurate Lorentz-Berthelot Combination Rule Lennard-Jones Lattice Summation, J. Chem. Theory Comput. **11**(12), 5737–5746 (2015). 68

[185] D. J. Evans and B. L. Holian, The Nose-Hoover thermostat, J. Chem. Phys. **83**(8), 4069–4074 (1985). 68

[186] M. Parrinello and A. Rahman, Polymorphic transitions in single crystals: A new molecular dynamics method, J. Appl. Phys. **52**(12), 7182–7190 (1981). 68

[187] M. Hanwell, D. E. Curtis, D. C. Lonie, T. Vandermeersch, E. Zurek, and G. R. Hutchison, Avogadro: an advanced semantic chemical editor visualization, and analysis platform, J. Cheminform. **4**(1), 17 (2012). 74

[188] V. Chaban, Computationally efficient prediction of area per lipid, Chem. Phys. Lett. **616-617**, 25 – 29 (2014). 76

[189] J. Douliez, A. Leonard, and E. Dufourc, Restatement of order parameters in biomembranes: calculation of C-C bond order parameters from C-D quadrupolar splittings, Biophys. J. **68**(5), 1727 – 1739 (1995). 77